ISSN: 2473-506X (Print)
ISSN: 2473-5078 (Online)

Volume 1, Number 2, 2018
IJPSZZ 1(2) 99-180

International Journal of Peening Science and Technology

ocp science

Papers in This Journal Are Available On-Line Before the Print Copy
www.oldcitypublishing.com/journals/IJPST-home/

INTERNATIONAL JOURNAL OF
Peening Science and Technology
(Print) ISSN 2473-506X • (Online) ISSN 2473-5078

PAPERS IN THIS JOURNAL ARE AVAILABLE
ON-LINE BEFORE THE PRINT COPY
www.oldcitypublishing.com/journals/IJPST-home/

Volume 1, Number 2, 2018 **International Journal of Peening Science and Technology** Pages 99-180

International Journal of Peening Science and Technology (IJPST)

Aims and Scope:

The ***International Journal of Peening Science and Technology*** (**IJPST**) aims to provide a global and multidisciplinary forum for the exchange of the science, technology, developments and applications surrounding the wide variety of peening techniques available. The Journal highlights the latest development which peening technologies have made to provide both scientific and industrial progress. Emphasis is placed on both the theoretical and practical contributions in relation to the methods, technologies, new applications/materials, and evaluates results and developments of enhanced solutions, new experimental methods and associated phenomena. Original research papers, case studies, review papers, short communications, mini reviews and letters to editor are all welcome. The scope of the journal is defined to include but, not limited to, the following areas: laser shock peening (LSP); plasma physics and dynamics; grit blasting; shot peening; blast and laser cleaning; ultrasonic peening; water-jet/cavitation peening; oil-jet peening; ion exchange beam peening; low plasticity burnishing and deep rolling; other material strengthening treatments; issues on plastic deformation and strengthening mechanisms; residual stresses and its management in materials; finite element analysis (FEA) and process modelling of the peening techniques; topographical and micro and nano structural characteristics; change in mechanical, electrical and biomedical properties using such peening techniques and reflects the main areas in which peening methods are used and developed for the surface engineering and for manufacturing applications.

Papers submitted for publication must be in English and must follow a prescribed format. All papers will be subjected to a critical peer-review prior to publication. Notes for contributors can be found at the back of the journal.

Publisher's World Wide Web Address

Additional information is available through the Publisher's web site at:
http://www.oldcitypublishing.com.

Ordering Information

Four issues per volume. Subscriptions are renewed on an annual basis. 2018 Volume: 1. Orders may be placed with your usual supplier or at the address shown below. Journal subscriptions are sold on a per volume basis only; single issues of the current volume are not available separately. Claims for non-receipt of issues will be honored if made within three months of publication of the issue. All issues are dispatched by airmail throughout the world.

Subscription Rates

Institutional rate (includes print and on-line):	US $1023	EURO €933	¥122,600
Individual rate (includes print version only):	US $205	EURO €194	¥26,340

The individual rate is available only to individuals whose library subscribes to the journal OR who warrant that the journal is for their own personal use. Orders must be sent directly to the Publisher and payment must be made by personal check or credit card.

Publication Schedule Information

To ensure your collection is up-to-date, please call +1 215 925 4390 for information about the latest issue published or visit the publisher's web site:
http://www.oldcitypublishing.com.

Orders should be placed through:
Customer Services Department
Old City Publishing
628 North 2nd Street
Philadelphia, PA 19123, USA

Tel: +1 215 925 4390
Fax: +1 215 925 4371

Enquiries can also be sent by e-mail via a link on the publishers web site:
http://www.oldcitypublishing.com.

Printed in USA.

OCTOBER 2018

Int. Journ. of Peening Science and Technology, Vol. 1, pp. 99–118
Reprints available directly from the publisher
Photocopying permitted by license only.

Finite Element Analysis of Residual Stress Induced by Multiple Laser Shock Peening with Square Spots

R. ZHU[1], Y.K. ZHANG[2], G.F. SUN[1], S.B. ZHANG[1], P. LI[1] AND Z.H. NI[1]

[1]*Jiangsu Key Lab Design &MfgMicronano Biomed Ins, Southeast University, Nanjing, Jiangsu 211189, China*
[2]*School of Electromechanical Engineering, Guangdong University of Technology, Guangzhou, Guangdong 510006, China*

Laser shock peening (LSP) is a competitive innovative surface treatment technique, which can induce compressive residual stresses in metal materials. In this investigation, a modified explicit finite element analysis (FEA) method was used to predict the residual stress distribution in 2050-T8 aluminum alloy induced by LSP. The laser shock sequence was programmed by VDLOAD ABAQUS subroutine. Simulated residual stresses from FEA showed good consistency with open literatures. Based on the method, the effects of LSP parameters such as overlapping percentage, number of impacts, laser power density, laser spot size on the average surface residual stress and average in-depth residual stress of 2050-T8 aluminum alloy were analyzed.

Keywords: *Laser shock peening, residual stress, modified explicit simulation*

1 INTRODUCTION

Over the past decades, laser shock peening (LSP) has been proposed as a competitive surface treatment technique [1], which can generate deeper compressive residual stress compared to those characteristics of the conventional shot peening, improve fatigue life [2], stress corrosion [3] and wear resistance [4] of metallic materials.

*Corresponding author's e-mail: gfsun@seu.edu.cn

With the development of laser technology, square shaped laser spot has been used in LSP. It has shown more efficient coverage, overlapping, uniform packing and improved surface quality for a layer of treatment as compared to the round shaped spot [1]. In order to predict the residual stress field and optimize LSP parameters, many experiments and analytical models have been reported in the literatures [5-10]. In the meantime, a number of finite element models (FEM) have been applied to simulate the confined LSP process. The conventional method involves two distinct steps using both explicit and implicit solving techniques to obtain an absolutely steady residual stress field. Braisted and Brockman [11] first adopted the combined approach to predict the residual stress distribution induced by LSP technologies in Ti-6Al-4V and 35CD4 steel in 1999. From then on, several researchers have used this method to analyse the laser shock waves propagated into different metallic materials, and predict residual stress distribution and surface deformation of the metal targets [12-17]. However, when there are multiple laser shocks, the above-mentioned method becomes difficult to be carried out. In order to meet the requirements of practical industrial applications, a variety of LSP parameters need to be considered for multiple laser shocks.

In view of the above-mentioned facts, this investigation adopted a modified explicit procedure [18] to predict the distribution of residual stress induced by LSP. Basic simulation for the LSP treatment of 25 impact loadings was calculated and validated. In addition, the influences of different LSP parameters such as overlapping percentage, number of impacts, laser power density, laser spot size were investigated.

2 3-D FEM AND VALIDATION

2.1 LSP analysis procedure

The modified explicit simulation approach adopted for LSP contains two analysis steps [18]. The first is used for each LSP with a short duration explicit approach until the kinetic energy approximates zero. The second is used for the final shot with an extended-duration explicit approach instead of implicit analysis. The modified explicit simulation approach should adopt infinite elements as non-reflecting boundaries and it is based on the observation that the redistribution of residual stress field drops when a transient stress state is steady. For a multi-shot simulation, the pulse shock sequence was implemented into ABAQUS/Explicit by using VDLOAD subroutine. The procedure of LSP simulation is shown in Figure 1.

2.2 High pressure pulse for LSP process

During an LSP process, a high intensity laser pulse vaporizes an absorbent layer, forming plasma and producing an extremely high pressure on the material surface with a short duration pulse pressure. The expression for the peak pressure P is given by Fabbro et al. [19]:

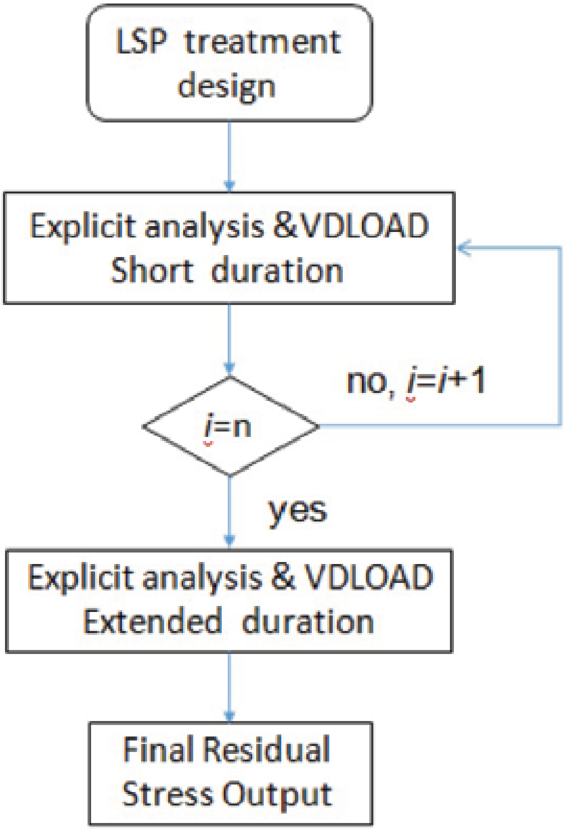

FIGURE 1
Laser Shock Peening Simulation Procedure.

$$P(\text{kbars}) = 0.10\left(\frac{\alpha}{2\alpha+3}\right)^{1/2} Z^{1/2}\left(g/cm^2 s\right) I_0^{1/2}\left(GW/cm^2\right) \tag{1}$$

where α is the efficiency of the internal energy devoted to the thermal energy, I_0 is the absorbed laser power density, Z is the reduced acoustic impedance between the target Z_{target} and the confining medium water Z_{water}.The model considers the plasma to be a perfect gas and the impedance between two materials is defined by the relation:

$$\frac{2}{Z} = \frac{1}{Z_{water}} + \frac{1}{Z_{target}} \tag{2}$$

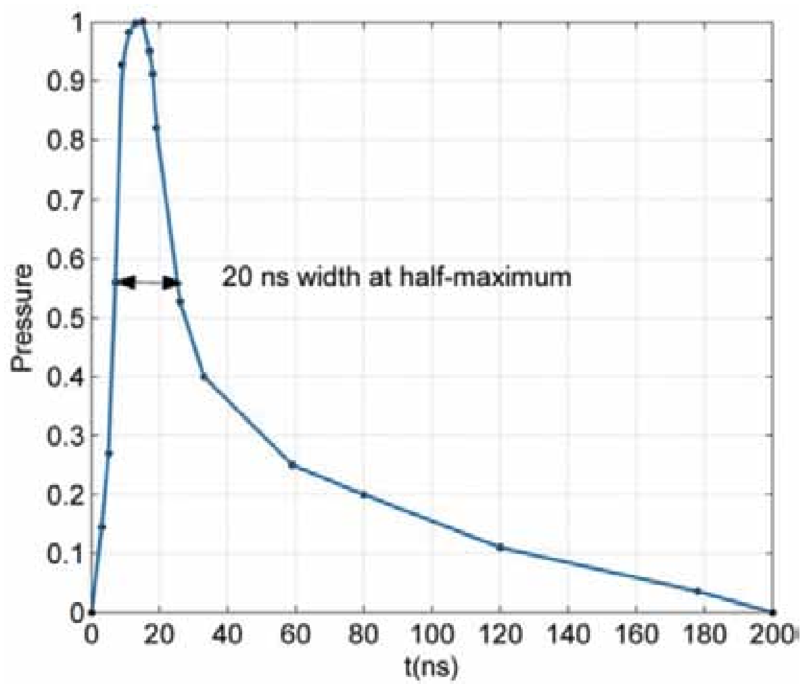

FIGURE 2
Normalized pressure pulse induced by a 8-10ns laser pulse used in ABAQUS.

For the aluminum target, we take $Z_{target} = 1.5 \times 10^6$ g/cm^2 s and $Z_{water} = 0.165 \times 10^6$ g/cm^2 s in the calculation, The value of α varies in a range of 0.2 to 0.5, and it just depends on the transparent confining layer and the other processing conditions [20]. α =0.35 is used and the peak pressure is given in Equation (3):

$$P(Gpa) = 1.65\sqrt{I_0(GW/cm^2)} \tag{3}$$

Owing to the fact that square spot shows better homogenous in intensity, the spatial distribution of shock pressure is presumed to be uniform. The typical profile of pressure pulse history evolution obtained from experiments is given in Figure 2 [21].

In the work, we imposed a fixed number of pressure pulse impacting a target material successively as shown in Figure 3. The averaged residual stresses $\sigma_{xx} = \sigma_{11}$ at the surface and along the depth of the target were considered. In addition, the overlapping percentage $R\%$ was defined by $R\% = \Delta d/d$ with d = laser spot size and Δd =distance between two adjacent laser impacts.

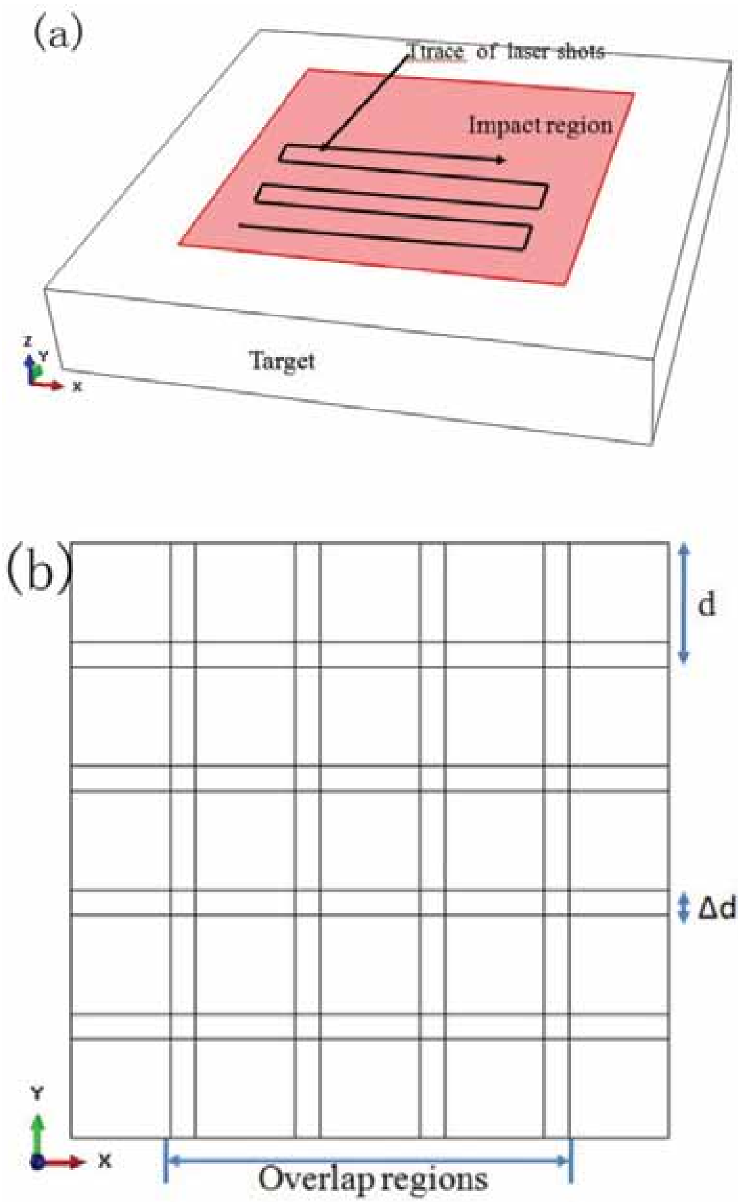

FIGURE 3
(A) The geometry of LSP, (b) schematic illustration of overlapped LSP.

2.3 Constitutive model and material properties

In LSP processes, the strain rate is in the order of 10^6/s. In order to accurately predict the material response, the Johnson-Cook model was adopted as the constitutive model to deal with high strain rate problems. Due to the fact that

TABLE 1
Mechanical properties of 2050-t8 aluminum alloy[21].

Material	*A* (MPa)	*B* (MPa)	*n*	*C*	ε_0 (/s)	*E* (Gpa)	υ	ρ kg/m^3
2050-T8	510	200	0.45	0.02	0.01	72	0.33	2750

thermal effect in LSP process is minimal, the thermal part of Johnson-cook model could be removed in the finite element simulations. Therefore, the equivalent Von Mises flow stress is given by:

$$\sigma = \left(A + B\varepsilon^n\right)\left[1 + CLn\left(\frac{\dot{\varepsilon}}{\dot{\varepsilon}_0}\right)\right] \tag{4}$$

where ε is the equivalent plastic strain, $\dot{\varepsilon}$ represents dynamic strain rate, and $\dot{\varepsilon}_0$ is the quasi-static strain rate, *A, B, C* and *n* are considered to be the material constants (*A* is the yield stress at 0.2% offset strain, *B* is the work hardening modulus, *n* represents the work hardening exponent and *C* represents the strain rate sensitivity). 2050-T8 aluminum alloy is the material considered for this investigation. The material property parameters required for FEM simulation are illustrated in Table 1.

2.4 Modeling of the LSP process

A three-dimensional (3D) dynamic FEM was developed to simulate the process of 25 square laser spots impacting on the target surface. Corresponding 3D model is shown in Figure 4(a). For the element type, two types of elements (C3D8R for finite elements and CIN3D8 for infinite elements) are used, as shown in Figure 4(b). The infinite elements are used as non-reflecting boundaries, which will prevent shock wave reflections on free surfaces from backing into the finite element area and also can reduce the computational time. Up to 2532495 continuums three dimensional eight-node with reduced integration elements were used to mesh the FEM. An element size of 150μm×150μm×100μm was used within the shocked region.

2.5 Modified method validation

The modified method is validated by comparing computed results with available experimental data and FEA results from Hfaiedh et al [21], in which a specimen of 2050-T8 aluminum alloy with a size of 25mm×25mm×5mm was treated by 25 laser impacts. In the literature, the spot size of 1.5mm, the overlap of 50%, the laser power density of 3.5 GW/cm^2 , and laser pulse of 10ns were used in the LSP process. Figure 5 shows the kinetic energy history from the LSP simulation. It can be seen that kinetic energy approaches zero for

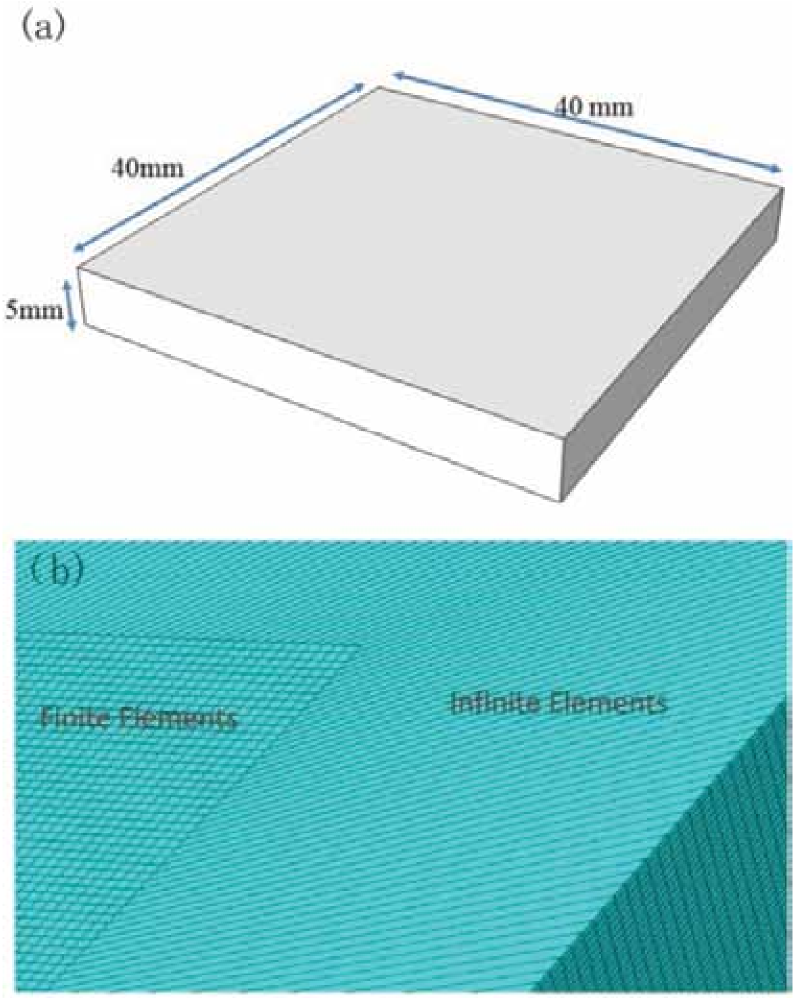

FIGURE 4
(A) 40mm×40mm×5mm 3-D model, (B) 3d fem mesh.

each LSP shot when the short duration reaches 8×10^{-6}s. Therefore, 8×10^{-6}s can be selected as the short duration and 4×10^{-5}s is selected as extended duration.

The comparison of surface residual stress σ_{11} is shown in Figure 6. It shows the simulated values (in grey lines in Figure 6a and b) from different data extraction lines and average simulated values (black line in Figure 6a and b). Similarly, the comparison of in-depth residual stress σ_{11} (Figure 7) also corresponds to average simulated values. The comparison shows a good similarity between simulations and the data from literature. Therefore, it

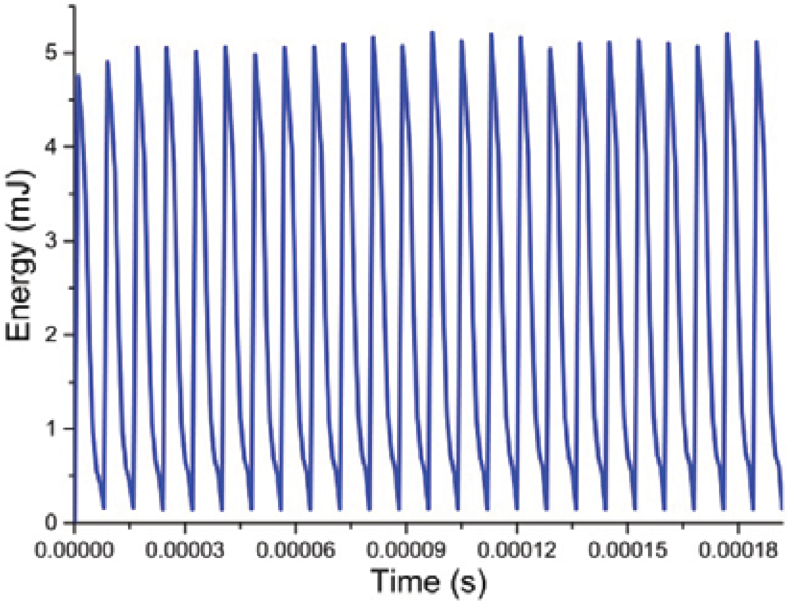

FIGURE 5
Kinetic energy history in each short duration.

could be concluded that the modified calculation method is reliable to simulate residual stress and can be used further to predict residual stress distribution in the target induced by LSP.

3 RESULTS AND DISCUSSION

3.1 Influence of overlapping percentage

Figure 8 shows the residual stress distributions of 25 impacts on 2050-T8 aluminum alloy when laser power density is 3.5GW/cm^2 , laser spot size is 3 mm, laser pulse is 10 ns, and overlapping rate is 5%. The average simulated values of residual stresses σ_{11} at the surface and along the depth of the target were considered using the inserted black dot lines (Figure 8 a and 8b).

Overlapping percentage can drastically affect the surface residual stress distribution and depth of residual stress during massive LSP impacts. 5% and 50% overlapping rates were applied to investigate the influence and other parameters used in the simulations were: laser power density of 3.5 GW/cm^2 , laser spot size of 3mm and laser pulse duration of 10ns.

Figure 9(a) shows that the surface residual stress across overlap regions tends to increase with overlapping percentage. The surface residual stress

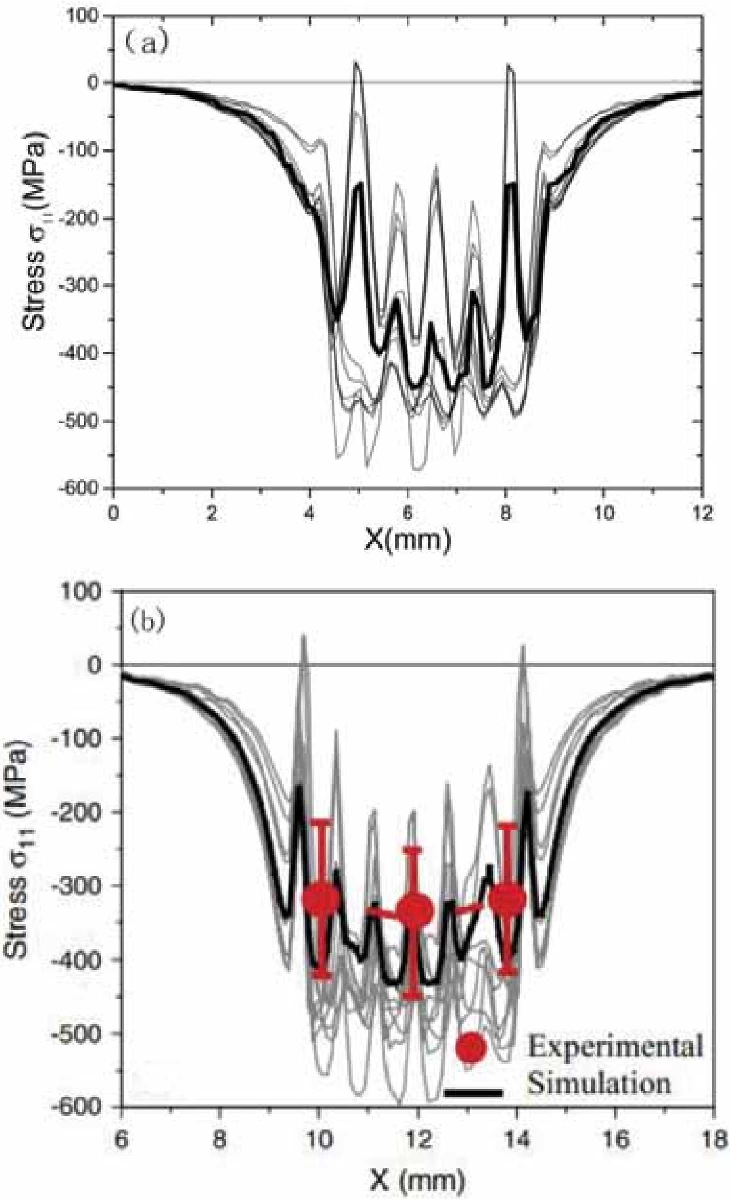

FIGURE 6
Comparison of surface residual stress σ_{11}, (a) modified calculation method, (b) reference values [21].

distributions of 50% overlap are more uniform than those of 5% overlap in the overlap regions. The non-uniformity of the residual stress field caused by the focusing of the radial stress waves has been considered, which can be defined by the following equation:

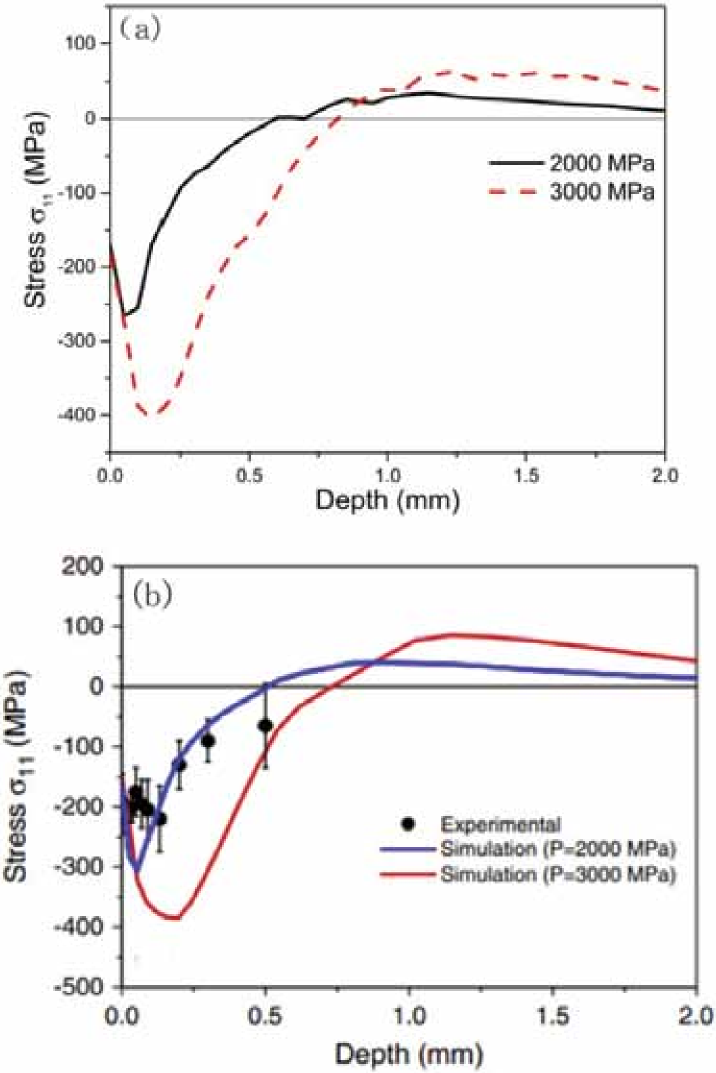

FIGURE 7
Comparison of in-depth residual stress , (a) modified calculation method, (b) reference values [21].

$$\phi = \frac{\sigma_{11}^{\max} - \sigma_{11}^{center}}{\sigma_{11}^{\max}} \times 100\% \tag{5}$$

where ϕ is the fluctuation ratio, σ_{11}^{max} is the maximum surface residual stress and σ_{11}^{center} is the surface residual stress of the spot center in the overlap regions. Table 2 shows the results of surface residual stress with different overlapping percentages obtained by numerical simulations.

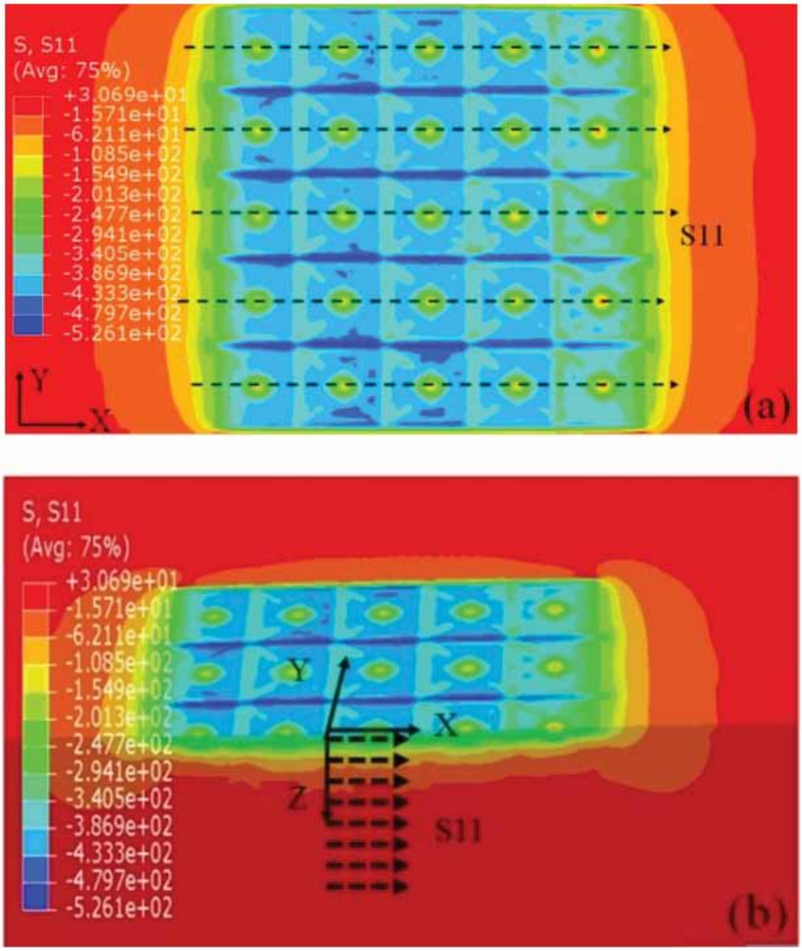

FIGURE 8
Residual stress distributions of simulated data, (a) surface residual stress, (b) in-depth residual stress.

Figure 9(b) exhibits the simulated in-depth residual stress. It indicates that the in-depth residual stress and plastically affected depth increase with the increase of overlapping percentage. The reason is that the overlap regions with an overlapping percentage of 50% suffer repeated LSP impacts. It can be seen that the number of LSP impacts reaches four across the overlap regions with 50% overlap. The residual stress and plastically affected depth generally increase with the increasing LSP impacts in a certain range.

3.2 Influence of multiple impacts

The surface and in-depth residual stress distributions that result from different numbers of impacts are shown in Figure 10. The LSP parame-

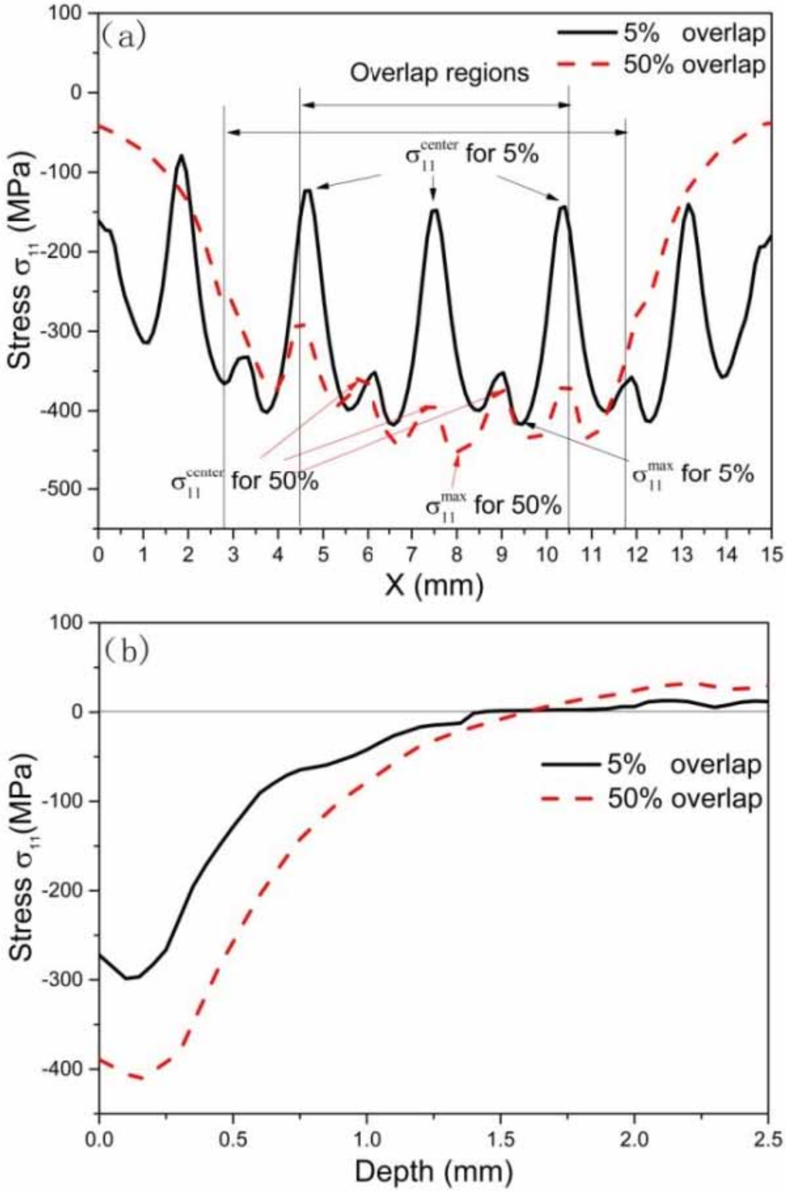

FIGURE 9
Influence of overlapping percentage on residual stress distribution, (a) surface residual stress, (b) through-thickness residual stress.

ters such as laser power density, laser spot size, laser pulse duration, and overlapping percentage used in the simulations were defined to be 3.5 GW/cm^2, 5mm, 10ns, and 50%, respectively. Fig. 11 shows a schematic

TABLE 2
Results of surface residual stress with different overlapping rates in the overlap regions.

Overlapping rate		(x, σ_{11}^{max} (mm, MPa)	(x, σ_{11}^{center} (mm, MPa)	ϕ
1.	5%	(9.45, -416.8)	(4.65,-123.1)	70.4%
2.	5%	(9.45, -416.8)	(7.5, -147.8)	64.5%
3.	5%	(9.45, -416.8)	(10.35,-143.5)	65.6%
4.	50%	(7.86, -450.5)	(6, -355.1)	21.2%
5.	50%	(7.86, -450.5)	(7.5, -391.3)	13.1%
6.	50%	(7.86,-450.5)	(9, -372.3)	17.3%

of 25 overlapped LSP shots for 50% overlap. As shown in Fig. 11, 1, 2, 3 and 4 represent four square spots. A represents the overlapped region of four square spots. When the overlapping percentage is 50%, the overlapped region suffers four impacts on the trace of laser shock for the first impact and twelve impacts on the trace of laser shock after the third impact. This explains why the stress after 3 impacts was lower than 1 impact in the overlapped area.

As shown in Figure 10(a), the surface residual stress of overlap regions decreases slightly with the increase of number of impacts on the same location. This result can be attributed to that surface deformations increase with the increasing number of impacts and it will induce the stress relaxation in the heavily deformed region. Literature [22] gave the similar results. Figure 10(b) shows that in-depth residual stress increases with increasing number of impacts, which is already evidenced analytically by Wei et al [12]. Hence, multiple impacts can have a beneficial effect on in-depth residual stress distributions.

3.3 Influence of laser power density

The peak pressure as a function of laser power density has been defined in Equation (3). It will create plastic strain when the peak pressure exceeds the shock yield strength(or Hugoniot limit *HEL*) ,which can be defined according to [21]:

$$P_H = \frac{1}{2}\rho \times C_{el} \times U_F \tag{6}$$

With C_{el}=elastic wave velocity=6000m/s, ρ=2750kg/m^3, U_F=free surface velocity=170m/s, we obtain Hugoniot limit value P_H=1.4 GPa.

The power density used for the simulation was assumed 1.5 GW/cm^2, 2.5 GW/cm^2, 3.5 GW/cm^2, and 4.5 GW/cm^2, corresponding to estimated peak pressures 2GPa, 2.6GPa, 3GPa, and 3.5GPa using Equation (3). In

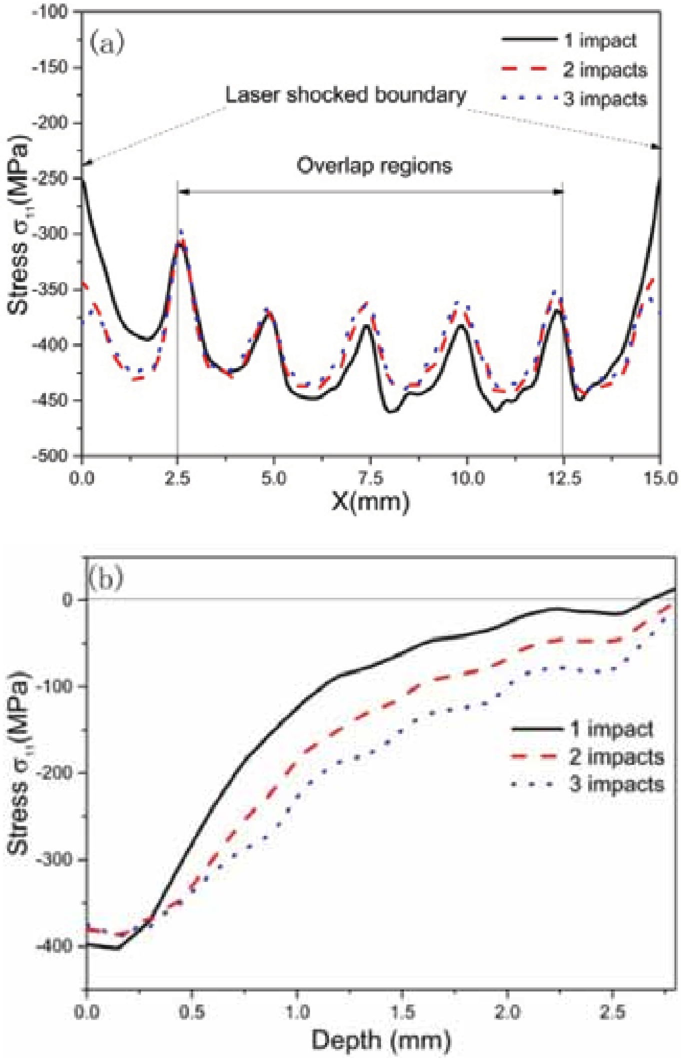

FIGURE 10
Influence of number of impacts on residual stress distribution, (a) surface residual stress, (b) in-depth residual stress.

addition, the simulation for each case was accomplished using the same LSP parameters (5mm spot size,10ns laser pulse duration and 50% overlap).

Figure 12(a) shows that surface residual stress increases with increasing power densities. The variation becomes small when laser power density

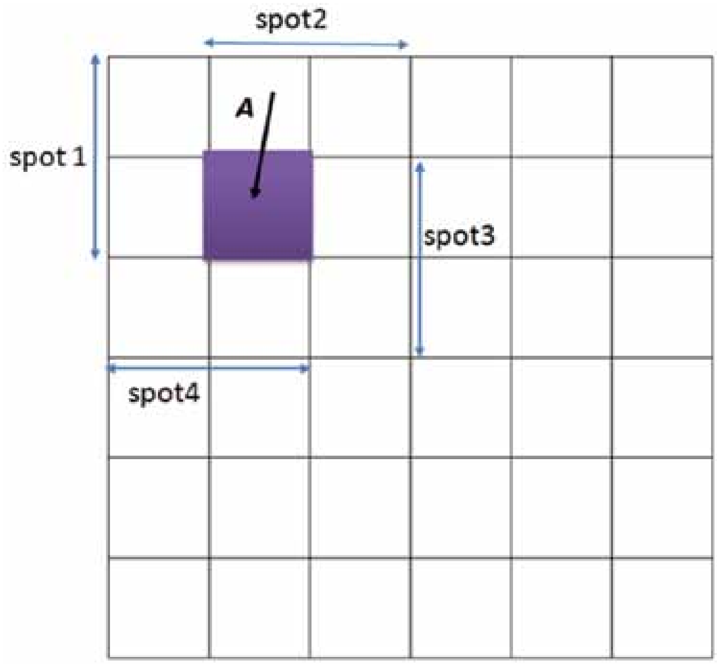

FIGURE 11
Schematic of overlapped 25 LSP shots for 50% overlap.

increases to 3.5 GW/cm^2. When the laser power density is in the range of 2.8 to 4.5 GW/cm^2 , corresponding peak pressure is between 2.8GPa and 3.5GPa, which is within the (2 to 2.5) × P_H range. The phenomenon is consistent with literature [23], which indicates that P= (2 to 2.5) × P_H is the optimum pressure for treatment of materials.

Figure 12(b) shows the residual stress along the depth of the target. As reported by Peyre [23] more than 20 years ago, the plastically affected depth increases with increasing power densities. Therefore, laser power density is a very important parameter to be optimized for generating residual stress fields.

3.4 Influence of laser spot size

In order to analyze the influence of spot size on residual stress distribution, the spot size was assumed to be 3mm, 4mm, and 5mm. The 3.5 GW/cm^2 laser power density , 10ns laser pulse duration, and 50% overlap were kept consistent in the simulations.

The results in Figure 13(a) show that surface residual stress distributions of overlap regions are quite similar to the variation of the laser spot size. However, the surface residual stress of laser shocked boundary

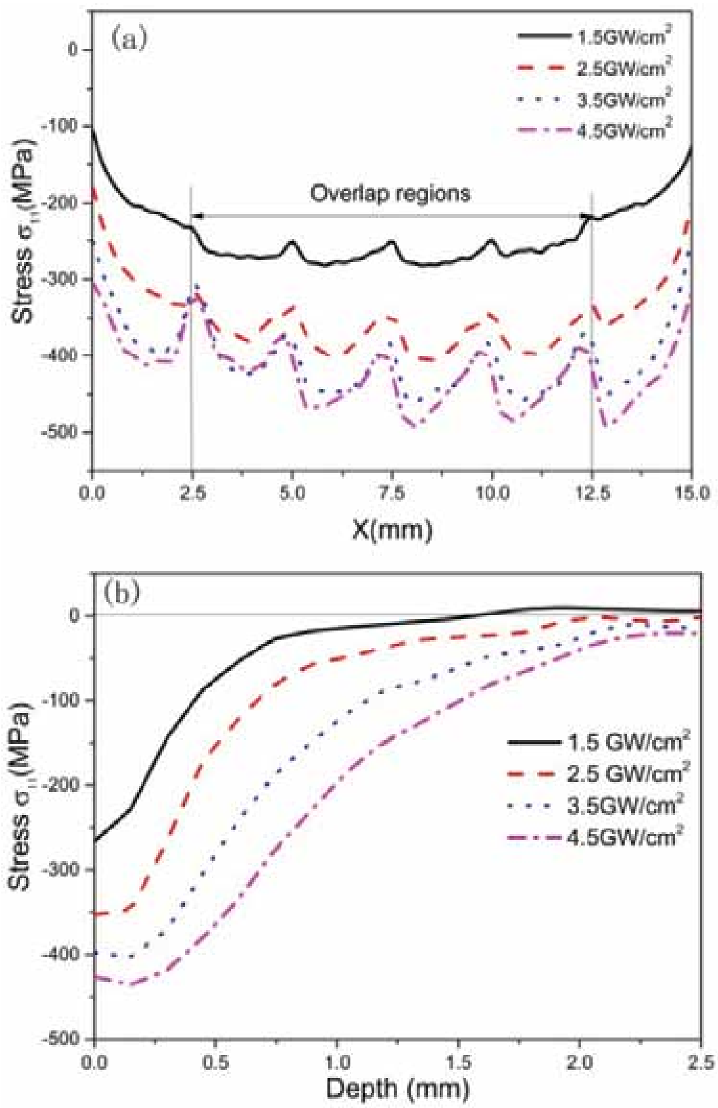

FIGURE 12
Influence of laser power density on residual stress distribution, (a)surface residual stress, (b) in-depth residual stress.

increases with increasing spot size. Increasing the laser spot size can also increase the depth of the residual stress. Figure 13(b) shows the distribution of in-depth residual stresses for d=3mm, 4mm and 5mm, respectively. It can be seen that plastically affected depth is increased by 36% as a result of increasing the laser spot size from 3 mm to 5 mm, which is evidenced by Peyre et al [24].

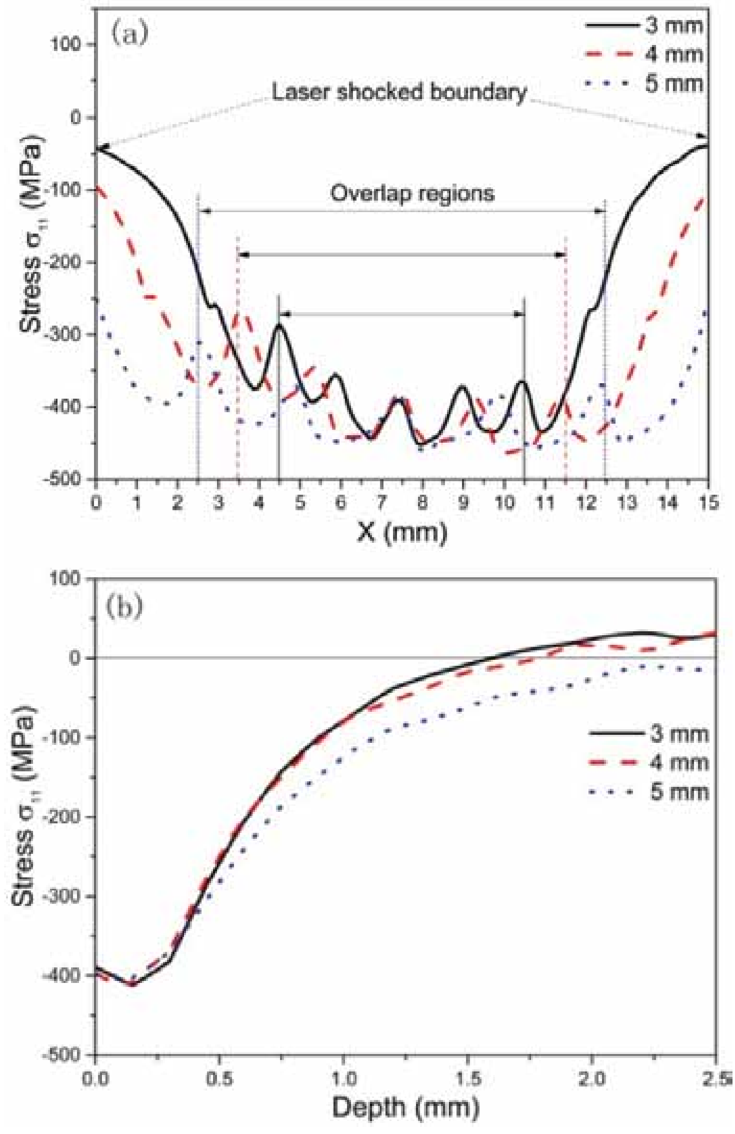

FIGURE 13
Influence of laser spot size on residual stress distribution, (a)surface residual stress, (b) through-thickness residual stress.

4 CONCLUSIONS

A three-dimensional model was proposed to predict the distribution of the average residual stresses field of 2050-T8 aluminum alloy after LSP treatment with multiple square spots. The following conclusions can be made.

(i) The modified explicit simulation was performed and verified with available results from literature. The use of VDLOAD subroutine makes the multi-spots three dimensional LSP simulation more convenient.
(ii) Compared with 5% overlap, 50% overlap can generate larger residual stresses with good uniformity and deeper plastically affected depth.
(iii) The surface residual stresses decrease with the increase of number of impacts for overlap regions, while the in-depth residual stresses increase with increasing the number of impacts.
(iv) P= (2 to 2.5) × P_H is the optimum pressure for LSP in this investigation. It can generate larger surface residual stresses and deeper plastically effected depth.
(v) The plastically effected depth increases with increasing the spot size, which implies that a larger spot size tends to produce a larger plastically affected depth of compressive residual stresses.

ACKOWLEDGEMENTS

This work was supported by the Joint Fund of Advanced Research of Equipment and Ministry of Education of China (Grant number 6141A02033103); the Scientific and Technological Innovation Project of Certain Commission of China (grant number 1716313ZT01001801); the Industry-University-Institute Cooperation Joint Research Project of Jiangsu Province of China (grant number BY2015070-05); the Six Talent Peaks of Jiangsu Province (grant number 2016-HKHT-001); the China Postdoctoral Science Foundation (grant numbers 2015M570395, 2016T90400); and the Postdoctoral Science Foundation of Jiangsu Province (grant number 1501028A).

NOMENCLATURE

A	Yield stress at 0.2% offset strain(MPa)
B	Work hardening modulus(MPa)
C	Strain rate sensitivity
n	Work hardening exponent
P	Peak pressure induced by laser beam(GPa)
Z	Reduced acoustic impedance(g/cm^{2}s)
Z_{target}	Shock impedance of the 2050-T8 aluminum alloy(g/cm^{2}s)
Z_{water}	Shock impedance of the water(g/cm^{2}s)
E	Elastic modulus(GPa)
I_0	Absorbed laser power density (GW/cm^2)

R%	Overlapping percentage
d	Laser spot size(mm)
Δd	Distance between two adjacent laser impacts(mm)
ϕ	Fluctuation ratio
C_{el}	Elastic wave velocity(m/s)
U_F	Free surface velocity (m/s)
P_H	Hugoniot limit value(GPa)

Greek symbols

σ_{11}^{max}	Maximum surface residual stress in the overlap regions(MPa)
σ_{11}^{center}	Surface residual stress of the spot center in the overlap regions(MPa)
ρ	Density of the 2050-T8 aluminum alloy(kg/m^3)
σ	Equivalent Von Mises flow stress(MPa)
v	Poisson's ratio
ε	Equivalent plastic strain
$\dot{\varepsilon}$	Dynamic strain rate
$\dot{\varepsilon}_0$	Quasi-static strain rate
α	Efficiency of the internal energy devoted to the thermal energy

REFERENCES

[1] Gujba, A. K, and Medraj, M. Laser peening process and its impact on materials properties in comparison with shot peening and ultrasonic impact peening. *Materials* **7** (2014), 7925-7974.

[2] Montross, C. S., Wei, T., Ye, L., Clark, G. and Mai, Y.W. Laser shock processing and its effects on microstructure and properties of metal alloys: A review. *International Journal of Fatigue* **24** (2002), 1021-1036.

[3] Hua, Y.Q., Bai, Y.C., Ye, Y.X., Xue, Q., Liu, H.X., Chen, R.F. and Chen, K.M. Hot corrosion behavior of TC11 titanium alloy treated by laser shock processing. *Applied Surface Science* **283** (2013), 775-780.

[4] Lim, H., Kim, P., Jeong, H. and Jeong, S. Enhancement of abrasion and corrosion resistance of duplex stainless steel by laser shock peening. *Journal of Materials Processing Technology* **212** (2012),1347-1354.

[5] Dorman, M., Toparli M.B., Smyth, N., Cini, A., Fitzpatrick, M.E. and Irving, P.E. Effect of laser shock peening on residual stress and fatigue life of clad 2024 aluminium sheet containing scribe defects. *Materials Science and Engineering: A* **548** (2012), 142-151.

[6] Gagliardi, M.A., Sencer, B.H., Hunt, A.W., Maloy, S.A. and Gray, G.T. Relative defect density measurements of laser shock peened 316L stainless steel using positron annihilation spectroscopy. *Journal of Nondestructive Evaluation* **30** (2011), 221-224.

[7] Qiao, H.C., Zhao, J.Z. and Gao, Y. Experimental investigation of laser peening on TiAl alloy microstructure and properties. *Chinese Journal of Aeronautics* **28** (2015), 609-616.

[8] Cao, Z.W., Xu, H., Zou, S.K. and Che, Z.G. Investigation of surface integrity on TC17 titanium alloy treated by square-spot laser shock peening. *Chinese Journal of Aeronautics* **25** (2012), 650-656.

[9] Lou, S., Li Y., Zhou L., Nie, X., He, G., Li, Y. and He, W. Surface nanocrystallization of metallic alloys with different stacking fault energy induced by laser shock processing. *Materials & Design* **104** (2016), 320-326.

[10] Yu, Q., Dong Z., Miao R., Deng, X. and Chen, L. Bending deformation of laser peened aluminium alloy with uniform rectangular spots. *Materials Science and Technology* **32** (2016), 9-14.

[11] Braisted, W. and Brockman, R. Finite element simulation of laser shock peening. *International Journal of Fatigue* **21** (1999), 719-724.

[12] Wei, X.L. and Ling, X. Numerical modeling of residual stress induced by laser shock processing. *Applied Surface Science* **301** (2014), 557-563.

[13] Cao, Z.W., Che, Z.G., Zou, S.K. and Fei, Q.X. Numerical simulation of residual stress field induced by laser shock processing with square spot. *Journal of Shanghai University* **15** (2011), 553-556.

[14] Hu, Y.X., Gong, C.M., Yao, Z.Q. and Hu, J. Investigation on the non-homogeneity of residual stress field induced by laser shock peening. *Surface & Coatings Technology* **203** (2009), 3503-3508.

[15] Hu, Y.X., Yao, Z.Q., Wang, F. and Hu, J. Study on residual stress of laser shock processing based on numerical simulation and orthogonal experimental design. *Surface Engineering* **23** (2007), 470-478.

[16] Ding, K. Three-dimensional dynamic finite element analysis of multiple laser shock peening processes. *Surface Engineering* **19** (2003), 351-358.

[17] Kim, J.H., Kim, Y.J., Lee, J.W. and Yoo, S.H. Study on effect of time parameters of laser shock peening on residual stresses using FE simulation. *Journal of Mechanical Science and Technology* **28** (2014), 1803-1810.

[18] Vasu, A., Hu Y. and Grandhi, R.V. Differences in plasticity due to curvature in laser peened components. *Surface & Coatings Technology* **235** (2013), 648-656.

[19] Fabbro, R., Fournier J., Ballard P., Devaux, D. and Virmont, J. Physical study of laser produced plasma in confined geometry. *Journal of Applied Physics* **68** (1990), 775-784.

[20] Clauer, A. H. and Lahrman, D. F. Laser shock processing as a surface enhancement process. *Key Engineering Materials* **197** (2001), 121-144.

[21] Hfaiedh, N., Peyre P., Song H., Popa, I., Ji V. and Vignal, V. Finite element analysis of laser shock peening of 2050-T8 aluminum alloy. *International Journal of Fatigue* **70** (2015), 480-489.

[22] Zhu, R.H., Xie H.M., Xue Y.F., Wang, L. and Li Y.J. Fabrication of speckle patterns by focused ion beam deposition and its application to micro-scale residual stress measurement. *Measurement Science and Technology* **26** (2015),095601.

[23] Peyre, P. and Fabbro, R. Laser shock processing: a review of the physics and applications. *Optical and Quantum Electronics* **27** (1995),1213-1229.

[24] Peyre, P., Berthe L., Scherpereel, X. and Fabbro R. Laser-shock processing of aluminium-coated 55C1 steel in water-confinement regime, characterization and application to high-cycle fatigue behaviour. *Journal of Materials Science* **33** (1998), 1421-1429.

Int. Journ. of Peening Science and Technology, Vol. 1, pp. 119–136
Reprints available directly from the publisher
Photocopying permitted by license only.

Improving the Surface Properties of Ti6Al4V with Laser Shock Processing

CESAR A. REYNOSO-GARCIA[1*], G. GOMEZ-ROSAS[2], O. BLANCO[2], C. RUBIO-GONZALEZ[3], ARTURO CHAVEZ CHAVEZ[2], E. CASTAÑEDA[1] AND J. L. OCANA[4]

[1]*Doctorate in Materials Science, CUCEI, University of Guadalajara, Jose Guadalupe Zuno # 48, Los Belenes, Zapopan, Jalisco, Mexico*
[2]*Department of Physics, CUCEI, University of Guadalajara, Blvd. Marcelino Garcia Barragan #1421, 44430, Guadalajara, Jalisco, México*
[3]*Centre for Engineering and Industrial Development, Av. Playa Pie de la Cuesta No. 702, Desarrollo San Pablo, Queretaro, 76130, Mexico*
[4]*UPM Laser Centre, Polytechnic University of Madrid, Ctra. de Valencia, Km. 7,300. 28031 Madrid, Spain*

Laser shock processing (LSP) is a technique that induces residual compressive stresses in metallic objects through the plastic deformation caused by the propagation of shock waves generated by laser pulses. The alloy Ti6Al4V is utilized in various industries such as the aerospace, automotive, and medical industries. In this study, LSP was performed using a high-power, low-cost, Q-switched Nd:YAG pulsed laser that emits at two wavelengths, 1064 and 532 nm, with pulse times of 6 and 5 ns, respectively. Power densities of 8.4 and 7.5 GW/cm^2 were tested. The material had no protective layer on the surface but was covered with a thin film of water (LSPwC). At both power densities, LSP produced great depth and magnitude residual compressive stresses (a result not previously reported), a reduction in the friction coefficient, and an increase in the hardness were found. The results obtained with both wavelengths were satisfactory and improved the surface properties of Ti6Al4V.

Keywords: *LSP, coefficient of friction, Ti6Al4V, residual stress, hardness, Nd:YAG laser*

1 INTRODUCTION

The alloy Ti6Al4V has low density, high fatigue strength, and excellent corrosion resistance, and this combination of mechanical and physical

*Corresponding author's e-mail: carg23@msn.com

properties makes it desirable in the aerospace industry, where it is used for engine components such as compressor blades [1]. In addition, Ti6Al4V is used in medical prosthetics replacing hip, knee, shoulder, and wrist joints and in dental posts due to its biocompatibility with the human body [2, 3]. However, it is widespread use as a joint component is limited by its low wear resistance both adhesive and abrasive which causes the breakage of the passive layers when the metal enters friction and causes an acceleration in the corrosion and the produced residues are released into the organism [4].

Laser shock processing (LSP), also known as laser shock peening, is a technique that can alter certain mechanical properties of materials by creating a residual stress field to a depth of 1 to 2 mm [5]. The depth of the stress field is greater than that obtained with the abrasive blasting technique [6]. LSP uses high-power laser pulses directed onto the surface of the material. The power density of the laser pulses must be sufficiently high (1 to 10 GW/cm^2) to generate shock waves in the material [7]. These shock waves, upon propagating within the material, lead to plastic deformation that causes structural changes and increases the dislocation density, thereby improving the mechanical properties of the treated material [8]. Previous studies have compared LSP to other surface treatment processes, such as shot peening [9, 10], laser shock forming [11], and deep rolling [12], to determine the benefits of using LSP to treat metal components.

LSP is unique in that a number of treatment parameters and conditions can be varied. The variables include the laser wavelength [13, 14], pulse width [13, 15], power density [16, 17], and energy [3, 18]. An additional option is to apply a protective layer to the material surface to avoid thermal effects due to the plasma generated by LSP [16]. LSP without the protective layer is known as laser peening without coating (LPwC) [19, 20]. LSP also offers options with regard to confinement. One option is water immersion, in which the material is completely submerged in water and is usually irradiated with a wavelength of 532 nm [14]. Another option is water jet confinement, wherein the material is covered by a thin layer of water a few millimetres deep and either the 532 or 1064 nm wavelength can be used with minimal power losses [19].

Several authors in recent years have reported positive results with LSP using a high-power, low-cost Nd:YAG pulsed laser with both water immersion (532 nm) [13] and waterjet confinement (532 nm and 1064 nm) [22].

The LSP technique has shown favourable results in materials such as steel [23], aluminium [24], and titanium [25]. LSP has been applied to the alloy Ti6Al4V in various studies, which have reported that LSP leads to a field of surface deformation and induces residual compressive stresses [26]. Other studies have reported that LSP of Ti6Al4V improves the fretting fatigue [27], increases the micro-hardness [28], and increases the surface roughness [15].

The main objective of this study was to evaluate the effect of LSP on the micro-hardness, surface roughness, microstructure, friction coefficient, and wear of Ti6Al4V without an applied protective layer using a low-cost laser at two different wavelengths with approximately the same power density.

2 EXPERIMENTAL PROCEDURE

2.1 Material Background

A plate of Ti6Al4V manufactured to the ASTM B265 standard was obtained. Square specimens with dimensions of 50 mm × 50 mm × 7 mm were machined and ground with 80 and 100 grit/cm^2 size SiC abrasive paper to eliminate the residual stresses resulting from the manufacturing process.

2.2 Laser Peening

Then, the specimens were irradiated with a Quantel Brilliant B high-energy Nd:YAG pulsed laser with pulses at the fundamental wavelength of 1064 nm for 6 ns. A second optical harmonic coupled to the fundamental wavelength was used to produce pulses at a wavelength of 532 nm for 5 ns. An optical system consisting of mirrors and positive lenses (with a focal length of 1000 mm) was used to direct the laser beam with a diameter of 1.5 mm at 1064 nm and 1.3 mm at 532 nm. The maximum power density was 8.4 GW/cm^2 at 1064 nm and 7.5 GW/cm^2 at 532 nm. A programmable, motorised XY positioning system controlled the location of the beam on the specimen. The LSP treatment was conducted in a square area of 20 mm ´ 20 mm. A pulse density of 2500 pulses/cm^2 was used for both wavelengths, and the overlapping rate was set to achieve the desired distribution of laser pulses on the treated surface [29]. The setup for LSP without a surface coating is shown in Figure 1; the values of additional treatment parameters for both wavelengths are shown in Table 1.

2.3 Blind hole test for Residual Stress

The hole-drilling strain gage method was used to determine the residual stress field induced by LSP in the Ti6Al4V. A CEA-120-06-062UL strain gauge and an RS-200 milling guide with reaming (both items produced by the Vishay Precision Group, Inc.) were used in the tests. The residual compressive stresses were measured according to the ASTM E837-01 standard [30].

2.4 Friction and wear tests

Dry (unlubricated) sliding tests were performed with a Microtest S.A. MT 30 pin-on-disk tribometer. The test parameters are shown in Table 2. The wear tests were repeated four times for each LSP treatment condition and on the untreated material. The software provided with the tribometer (MT4002) was

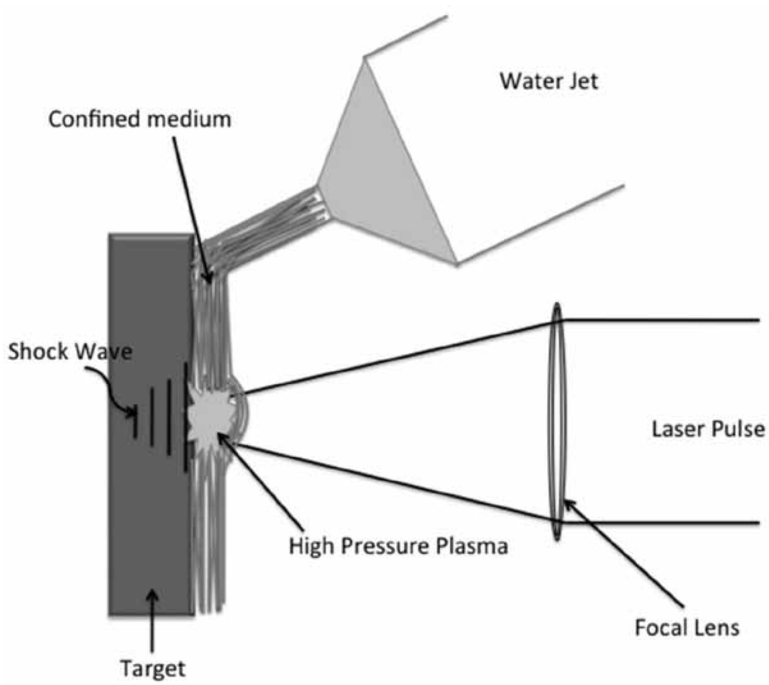

FIGURE 1
Laser shock processing without coating set up.

TABLE 1
LSP treatment parameters.

Wavelength	**1064nm**	**532nm**
Confining mode	Water-Jet	
Ablative coating	No	
Laser	Nd:YAG	
Pulse density	2500 pulses/cm^2	
Spot diameter	1.5 mm	1.3 mm
Pulse duration	6 ns	5 ns
Powerdensity	8.4 GW/cm^2	7.5 GW/cm^2
Energy	0.9 J	0.5 J
Frequency	10 Hz	

used to process the test data, and the coefficient of friction was calculated according to the ASTM G99-04 standard [31].

The friction tests used to obtain the dry slip curves exhibit four stages. The first stage (I) consists of the coupling of the tribological pair (the pin and the disk). In

TABLE 2
Pin-on-disk test parameters.

Speed	**0.0471**	**m/s**
Sliding distance	500	m
Track Radio	1.5	mm
Pin	Steel	AISI 52100
Pin diameter	3	mm
Revolutions	53052	rev
Time	177	min
Load	30	N

the second stage (II), the friction force stabilises. In the third stage (III), a sharp increase in friction occurs, usually catastrophically. In the fourth and final stage (IV), the tribological pair stabilises again and fluctuations occur because of the particles that are released as the result of wear in the tribological pair [32, 33].

2.5 Metallographic analysis

A metallographic analysis was performed according to the ASTM E3-11 standard [34] on cross sections of the treated specimens. The specimens were ground on a Buehler Phoenix® Betagrinding-polishing machine with 240, 400, 800, and 1200 grit/cm^2 size SiC abrasive paper, then polished using 9, 3, and 1 μm diamond suspensions to remove surface scratches. Finally, a mirror finish was obtained by polishing with colloidal silica with a diameter of 0.01 μm. The chemical solution for developing the metallographic samples was a mixture of 190 ml of water, 2 ml of hydrochloric acid, 2 ml of nitric acid, and 2 ml of hydrofluoric acid. The samples were submerged for 30 seconds in the solution. The material phases were examined with scanning electron microscopy (SEM) using a Tescan MIRA3 microscope.

2.6 Phase characterisation

The material phases were determined using a Phillips Expert X-ray diffractometer with a Cu anode (λ= 1.54056). The X-ray diffraction pattern was calculated for each peak over a range of angles from 33.01 to 72.99 degrees.

2.7 Micro-hardness tests

Eight indentations were made 85 microns from each other from the surface of the material to a depth of 1000 microns in the cross-section of the LSP-treated specimens. A Vickers indenter was used to apply a load of 200 g for 20 seconds as prescribed in the ASTM E384 standard. Micro-indentation hardness measurements were performed on the cross-sections of the specimens treated with LSP (from the material surface to a depth of 1 mm). A Vickers indenter was used to apply a load of 200 g for 20 s, as prescribed in the ASTM E384 standard [35].

2.8 Surface roughness

The surface roughness was measured using a Leica confocal scanning laser microscope prior to and subsequent to LSP. The microscope has a scan range of 17 mm in the two horizontal axes (X and Y) and a vertical resolution (Z) of up to 0.01 nm. The measurements were taken over the entire LSP-treated area.

3 RESULTS

3.1 Residual stresses

Figure 2 shows in detail the profiles of the residual stress in the untreated specimen and that treated with LSP with a wavelength of 532 nm and a power density of 7.5 GW/cm^2. The treated specimen had a maximum induced compressive stress of 500 MPa at a depth of 280 μm. The residual stresses at the same depth in the untreated specimen were 280 MPa. Figure 3 shows the profiles of the residual stresses for the untreated specimen and that treated with LSP with a wavelength of 1064 nm and a power density of 8.4 GW/cm^2. The maximum compressive stress was 750 MPa at 325 μm in the treated specimen. The residual compressive stress was 280 MPa in the untreated specimen at the

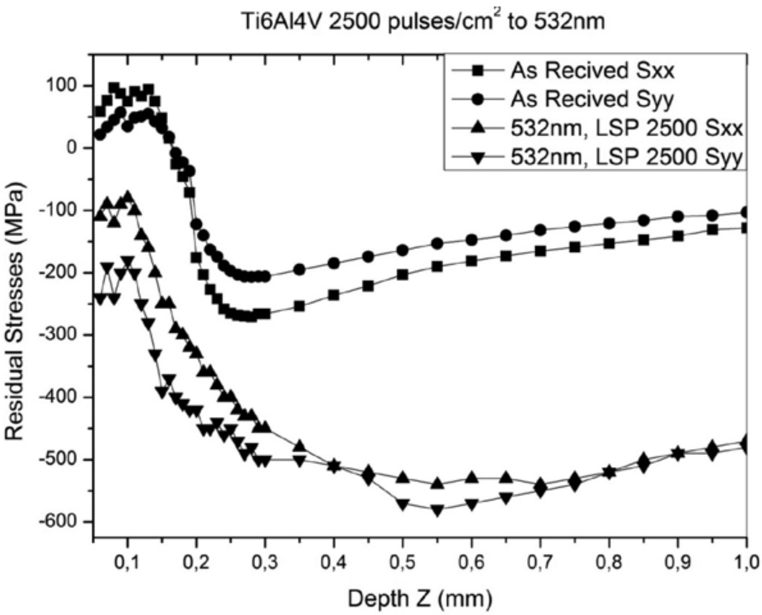

FIGURE 2
In depth residual stresses profile of untreated and processed sample with 532nm. Stress component s_{xx} is parallel while s_{yy} is perpendicular, both to swept direction that will be used during the treatment LSP.

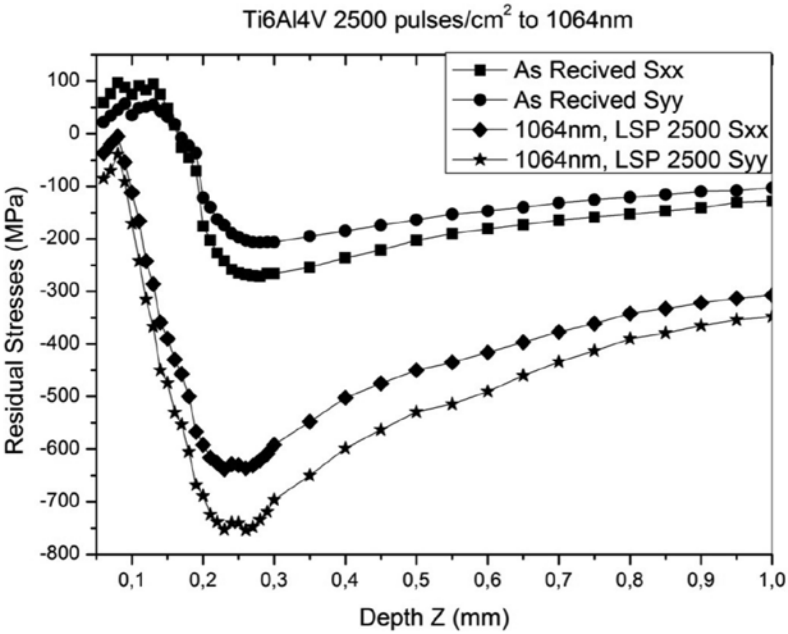

FIGURE 3
In depth residual stresses profile of untreated and processed sample with 1064nm. Stress component s_{xx} is parallel while s_{yy} is perpendicular, both to swept direction that will be used during the treatment LSP.

same depth. The measurements reveal that the residual compressive stresses induced in the Ti6Al4V by LSP with either wavelength were higher in magnitude and extended deeper into the material compared with the untreated specimen. In addition, these values were greater than those previously reported [25].

3.2 Friction

The results of the wear tests on the dry(unlubricated) samples treated with LSP at a power density of 8.4 GW/cm^2 are shown in Figure 4(a). The adjustment stage (I) occurred between 0 and 8 metres, followed by a period of stability in the frictional force (stage II) from 8 to 14 metres. In stage III, a transition can be observed in the untreated specimens. The frictional force on the specimens treated with LSP was stable from 14 to 52 metres. In stage IV, the untreated specimens exhibited frequent transitions and the treated specimens had shorter transitions. The frictional force in the treated samples stabilised again at 77 metres, at which point the abrupt transitions began to occur until the end of the test. The treated specimens had a stable frictional force over a longer distance. In Figure 4(b), the results for the specimens treated with LSP at a power density of 7.5 GW/cm^2 are shown. The lengths of the adjustment stage (I) and the stability period (II) were equal to those observed

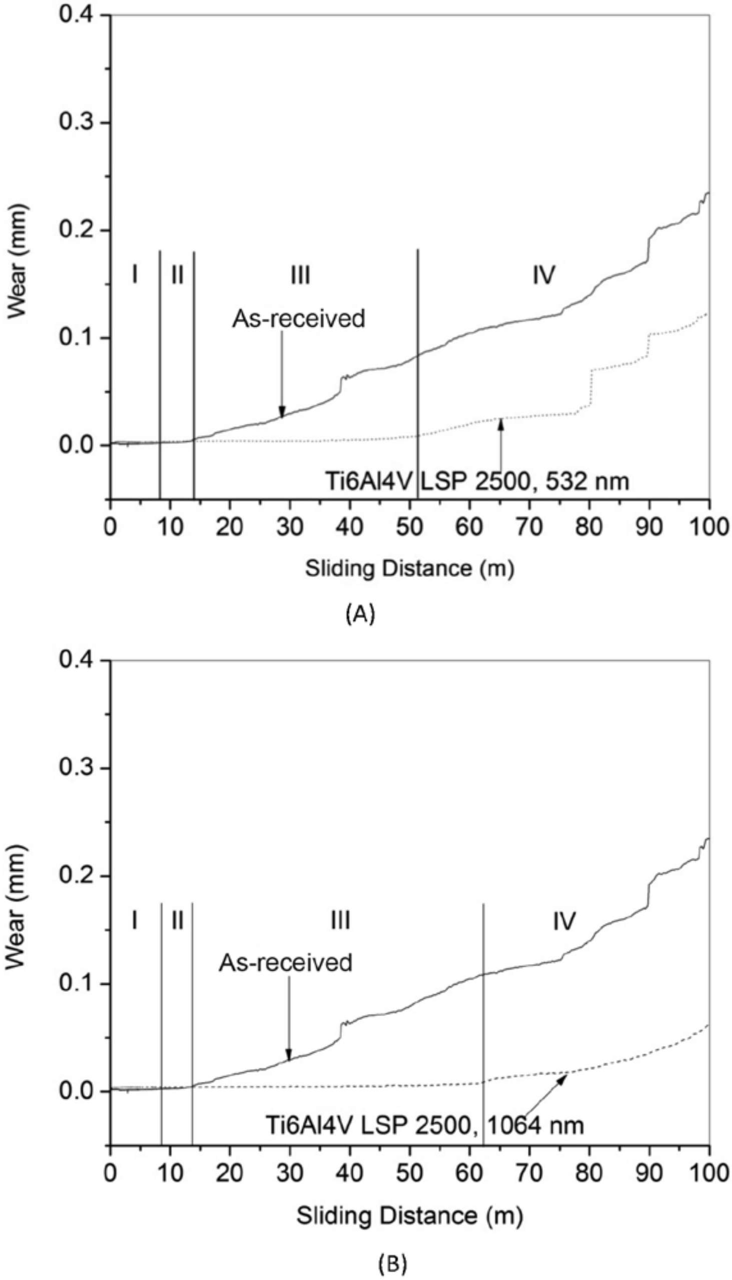

FIGURE 4
Friction force stabilization. Figure 5(a) sample treated with 532nm and figure (b), 1064 nm wavelength.

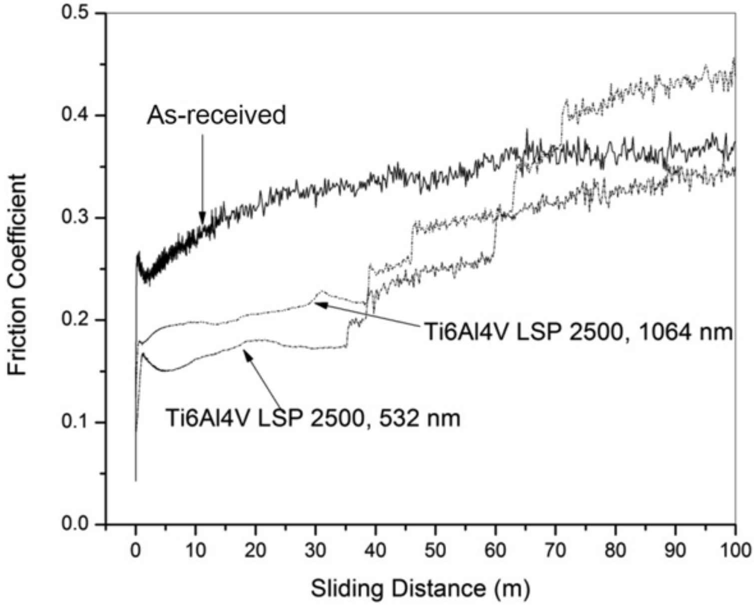

FIGURE 5
Stabilized friction coefficient. Samples without LSP and treated with LSP at 532nm and 1064nm wavelength.

in the specimens treated with a power density of 8.4 GW/cm^2. Stage III in the untreated specimens was characterised by the appearance of the transitions, whereas the frictional force was stable in the treated specimens. During this period (from 14 to 63 metres), small transitions were observed before 63 metres. Beyond this point (in stage IV), transitions occurred in the treated specimens, but no abrupt transitions and instability in the frictional force were observed at 100 metres. The friction test results for the two power densities used showed that the stage of stability of the frictional force was longer in the treated specimens than in the untreated specimens.

3.2.1 Friction Coefficient

Figure 5 shows the results of the friction coefficient of Ti6Al4V. The friction coefficient presented an improvement in the two wavelengths. However, the biggest improvement is in the wavelength of 532nm (0.16). The reduction of the friction coefficient presented could be due to the increase of the hardness and the residual stresses observed after the LSP treatment compared to the material as recived.

On the other hand, there is a difference in wavelengths in the reduction of the friction coefficient. This difference could have two explanations: first, the relationship with the depth of hardness, at a wavelength of 532 nm, a higher hardness (Hv) is obtained up to about 225 microns than at the wavelength of

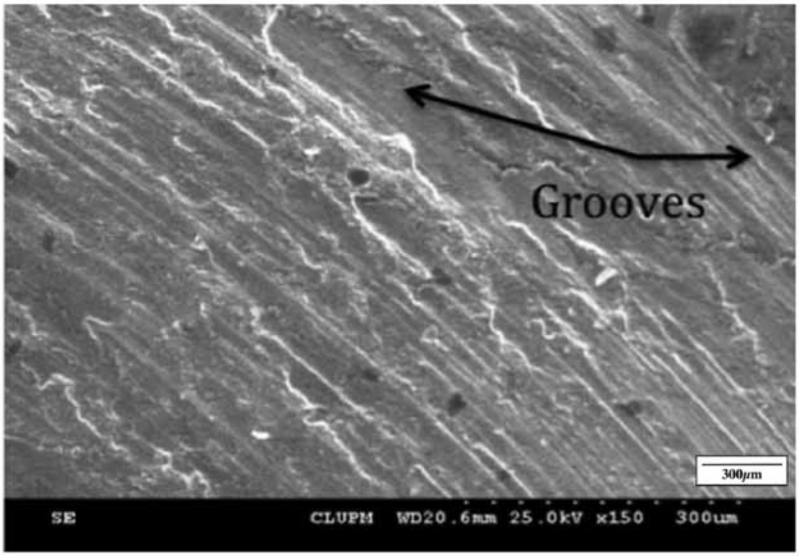

FIGURE 6
Wear systems in material without LSP treatment.

1064 nm (Hv). Secondly, the depth of the residual stresses can be observed that at the wavelength of 532nm reaches its greatest magnitude at a depth of 550μm. However the wavelength of 1064nm has a maximum magnitude at 250 microns in depth, regardless of the magnitude of the residual stresses that is greater at the wavelength of 1064nm but at a lower depth.

In both cases the difference between one wavelength and another is most likely due to the greater hardness and depth of residual stresses present at the wavelength of 532nm.

Figure 5 shows the experimentally determined values for the coefficient of friction of Ti6Al4V. The friction coefficient was lower for the treated samples for both power densities: the values were 0.16 for a density of 7.5 GW/cm^2 and 0.18 for a density of 8.4 GW/cm^2, and that for the untreated specimen was 0.26.

3.2.2 Wear

Figure 6 shows the wear in the untreated specimen. Grooves can be observed that are parallel to the direction of the sliding track. Figures 7(a) and 7(b) show the wear patterns, which were identified from the sliding tracks, in the LSP-treated samples for wavelengths of 532 nm and 1064 nm, respectively. Figure 7(a) shows that the wear particles had a flat morphology (plate or foil type), which is a characteristic of both dry and lubricated wear. This result is due to the discontinuous application of the normal force by the pin to the disk surface, which can cause fatigue on the surface. Furthermore, a separation of the metal particles can be observed, which can occur in regions subjected to friction or

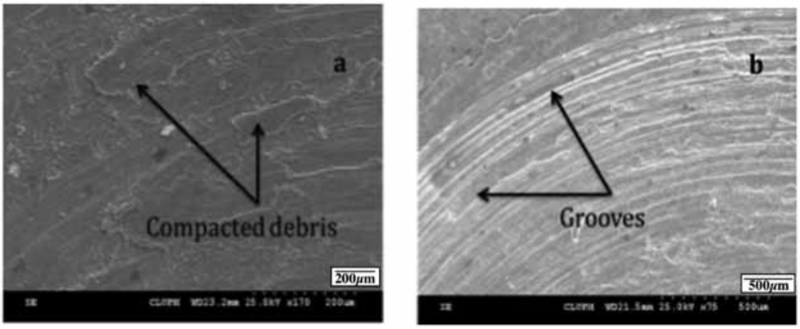

FIGURE 7
Wear systems after pin on disk test in LSP material treatment, a) at 532nm, b) at 1064nm.

relative motion, including cases where the material is soft [36]. Figure 7(b) shows that the surface of the specimen treated with a wavelength of 1064 nm has grooves in the abraded area that are of greater length and uniformity than those in the untreated specimen. These wear patterns were observed in the pin-on-disk test and were found in the material treated with LSP. This observation confirms that materials with an HCP crystal structure exhibit less adhesion than materials with a BCC or FCC crystalline structure [37, 38]. These results are consistent with those obtained in previous studies [24].

3.3 Metallographic analysis

Figure 8 no reduction in the grain size was observed at the surfaces of the treated specimens. The two characteristic phases, α and β, of the material remained unchanged.

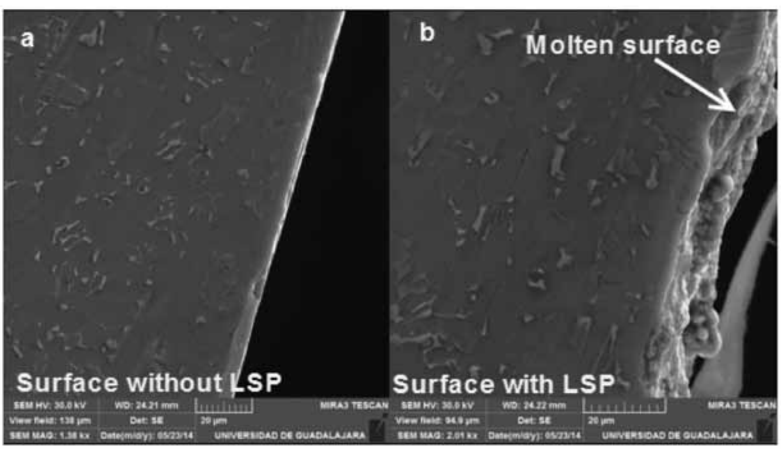

FIGURE 8
Surface microstructure of Ti6Al4V. A) without LSP. B) with LSP.

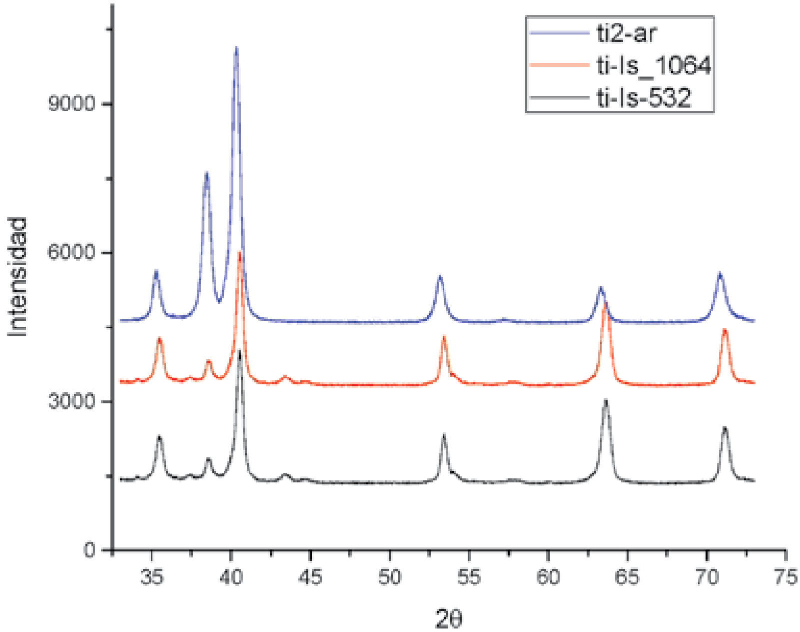

FIGURE 9
X-Ray diffraction pattern of laser peened samples red and black pattern, and blue pattern of untreated material.

3.4 Phase characterisation

The X-Ray diffraction tests did not show any phase changes or the formation of a different phase following LSP. Figure 9 shows the Miller indices of the crystallographic planes corresponding to the peaks in the X-Ray beam intensity as a function of the diffraction angle 2θ. The values for the 004 peak were shifted to the right with respect to the values for the untreated material. This result indicates the presence of residual compressive stresses in the material after being treated with LSP.

3.5 Micro-hardness tests

The hardness profiles by micro-indentation of the specimens are shown in Figure 10. The hardness in the first 250 μm was greater in the treated specimens than in the untreated specimen. The values of the micro-hardness of the untreated specimen were 303 and 294 (HV) at depths of 85 μm and 225 μm, respectively. In the sample treated with LSP at 7.5 GW/cm^2, the hardness values were 341 and 315 HV at the same two depths; i.e., the microhardness increased by 38 and 21 HV compared with the untreated specimen. In the specimen treated with LSP at 8.4 GW/cm^2, the hardness values obtained were 326 and 303 HV at the same two depths. Therefore, increases of 23 HV and 9 HV over those of the untreated specimen were obtained. The standard error

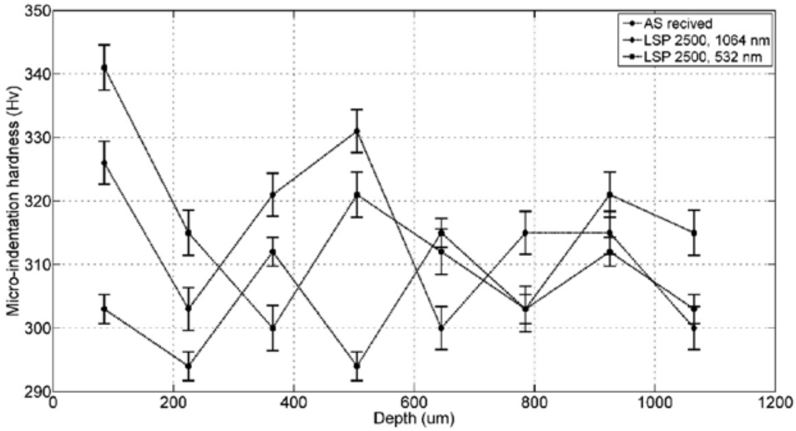

FIGURE 10
Measurement of micro-indentation harness profile on the specimen cross section. Samples treated with 532 nm and 1064 nm wavelengths.

calculated of hardness test was at range from to 2 and 4 HV. Tests of the hardness of the surface of Ti6Al4V treated with LSP have been previously reported [39].

3.6 Surface roughness

Figure 8 (b) shows the melt surface of Ti6Al4V alloy, rapid heating and fusing and the high pressure of the plasma generated by the laser pulse cause the liquefied material to be ejected from the centre to the periphery of the laser spot. This effect is shown in Figure 11. The ejected material is rapidly cooled by the water layer covering the surface of the material, resulting in an increase in surface roughness. The surface roughness is further increased by the overlapping of the laser pulses. The surface roughness values (Ra, arithmetic profile deviation) of the samples are shown in Table 3 for the two power densities. Despite the increase in the final surface roughness of the samples treated with LSP, no further surface finishing is required because the surface uniformity is greater than that obtained by abrasive blasting [24].

4 DISCUSSION

Because the water film confines the plasma generated by LSP, the surface temperature reaches approximately 2200 °C (the melting temperature of Ti64 is between 1604 and 1660 °C) [40]. This high temperature vaporises and melts the surface material, which rapidly cools, causing hardening. The interaction of the plasma with an aqueous environment generates an oxide film of approximately 1 μm in thickness, which is deposited on the surface and dif-

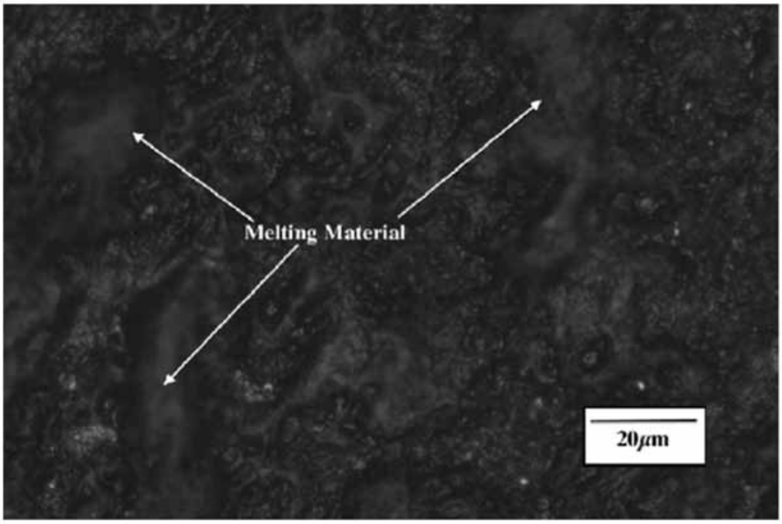

FIGURE 11
Unfocused areas show molten material after LSP treatment.

TABLE 3
Ra superficial roughness values.

Equipment	Base Material (Ra)	1064 nm	532 nm
Laser confocal Microscope	0.7454 μm0.5	2.9261 μm0.5	2.8821 μm

fuses into the material [14]. This combination of oxidation and surface hardening could affect the tribological properties of Ti6Al4V.

In the coupling phase of the tribological pair, variations in the friction force occur because the interaction between the two materials is slightly unstable causing skipping to occur (loading and unloading of the normal force). At this stage, the coefficient of friction is not stable because of differences in the roughness and the hardness of the two materials that constitute the tribological pair.

In the second stage, when the tribological pair stabilises, the oxide layer deposited on the surface acts as a lubricant. At this stage, because of the aforementioned properties and the increase in hardness, the friction coefficient decreases from 0.26 for the untreated specimen to 0.16 for the specimen treated with a power density of 7.5 GW/cm^2 and to 0.18 for the specimen treated with a power density of 8.4 GWm^2. The surface roughness due to the expulsion of molten material during the treatment increases considerably, from 0.7454 μm for the untreated specimen to 2.8821 μm for the specimen treated with a 7.5 GW/cm^2 power density and to 2.9261 μm for the specimen treated with an 8.4 GW/cm^2 power density. This change in roughness does not have a significant effect regardless of the friction load applied in the test, as reported in the literature [41]. The change in the surface hardness induced by LSP is consistent to a depth of approximately 250 μm. The friction coefficient remains constant with the surface roughness.

In the third stage, greater wear was observed in the treated surface at depths greater than 250 μm. This difference is the result of material emission during the test. Figure 4(a) shows the transitions in which the pin penetrates the Ti6Al4V and the subsequent re-stabilization of the tribological pair for short periods as the effect of the induced hardness for the treatment with a 7.5 GW/cm^2 power density begins to decrease. In Figure 4(b), it can be observed that the transitions are much smoother and that stabilisation of the tribological pair occurs a second time because the effect of the induced hardness for the treatment with an 8.4 GW/cm^2 power density persists.

5 CONCLUSIONS

The surface residual compressive stresses in specimens of Ti6Al4V treated with Laser shock processing (LSP) increased by 257.14% in specimens treated at a power density of 8.4 GW/cm^2 and a wavelength of 1064 nm; and by 93% in specimens treated with a power density of 7.5 GW/cm^2 at 532 nm compared with the untreated specimen. The power density has an important role in the magnitude and depth of the residual compressive stresses.

The friction force was stable over a greater duration in the specimens treated with LSP. The friction coefficient decreased by 38.5% and 30.5% for specimens treated with a power density of 7.5 GW/cm^2 and 8.4 GW/cm^2, respectively. These results represent an increase in the period of stability of the frictional force of 475.19% and 350% for the specimens treated at a power density of 7.5 GW/cm^2 and 8.4 GW/cm^2, respectively, compared with the untreated specimen.

No phase changes were observed in the alloy following LSP. The crystallographic peaks decreased slightly in intensity, and the widths increased. It is possible that these changes were due to LSP.

The surface hardness at a depth of 225 μm increased by 19% in specimens treated with a 7.5 GW/cm^{2}power density and by 10% in specimens treated with an 8.4 GW/cm^2 power density compared with the untreated specimen. This increase may have been caused by the presence of oxides on the irradiated surface. The decrease in the friction coefficient corresponded to an increase in the surface hardness of the specimens treated with LSP.

The surface roughness of the specimens increased by 392.5% for the specimens treated with LSP at an 8.4 GW/cm^2 power density and by 386.6% for the specimens treated with LSP at a 7.5 GW/cm^2 power density compared to that of the untreated specimen. Despite this increase, the surface quality remained satisfactory and would be acceptable for biomedical applications.

The wear in the treated and untreated specimens exhibited damage at the periphery of the pin test disk. In future research, depths from 0 to 250 μm, where changes due to LSP have been observed, they will be analysed in a later article.

In this study, LSP was tested on Ti6Al4V specimens without an ablative protection layer and using two different wavelengths. LSP can be used with two forms of confinement, waterjet and total immersion. These options are satisfactory in improving the mechanical properties, including residual stresses, the coefficient of friction, the surface hardness and the surface roughness.

6 ACKNOWLEDGEMENTS

The authors would like to thank the Centre for Engineering and Industrial Development (CIDESI) of Queretaro; the U.P.M. Laser Centre, Madrid, Spain; the Departments of Physics and Project Engineering at the University of Guadalajara for providing the facilities used in this research; and the National Council of Science and Technology (CONACYT) for the award of a postgraduate scholarship.

REFERENCES

[1] Altenberger, I., Nalla, R.K., Sano, Y., Wagner, L., Ritchie, R.O. On the effect of deep-rolling and laser-peening on the stress-controlled low- and high-cycle fatigue behaviour of Ti–6Al–4V at elevated temperatures up to. *Int. J. Fatigue,* **44** (2012), 292-302.

[2] ASTM. *E-837-01, Standard Test Method for Determining Residual Stresses by the Hole Drilling Strain Gage Method,* (2002), ASTM International, (v.03.01).

[3] ASTM, G. (2004), 99-04 Standard test method for Wear testing with a pin on disk apparatus ASTM International.

[4] ASTM. (2012), E-3-11, Standard Guide for preparations of metallographic specimens, ASTM International, (v.03.01).

[5] ASTM. (2011), E384 11-1 Standard test method for Knoop and Vickers hardness of materials, ASTM International, (v.03.01).

[6] Bagherifard, S., Ghelichi, R., Guagliano, M. Numerical and experimental analysis of surface roughness generated by shot peening. *Appl. Surf. Sci.,* **258** (2012), 6831-6840. doi: 10.1016/j.apsusc.2012.03.111.

[7] Buckley, D.H. *Surface Effects in Adhesion, Friction, Wear, and Lubrication, Tribology Series* (1981), Amsterdam: Elsevier.

[8] Campbell F.C. Titanium. In Campbell, F.C. (ed.), Chapter 28, *Elements of Metallurgy and Engineering Alloys*. Materials Park, OH: ASM International, 2008, pp 527-545.

[9] Castañeda, E., Rubio-Gonzalez, C., Chavez-Chavez, A., Gomez-Rosas, G. Laser shock processing with different conditions of treatment on duplex stainless steel. *J. Mater. Eng. Perform.*, **24** (2015), 2521-2525.

[10] Clauer, A.H., Holbrook, J.H. Effects of laser induced shock waves, rate phenomena in metals. In: Meyers, M.A. et al. (ed.), Chapter 38, *Shock Waves and High-Strain-Rate Phenomena in Metals*. New York, NY: Plenum Press. 1981. pp 675-703.

[11] Fairand, B.P., Clauer, A.H., Jung, R.G., Wilcox, B.A. Quantitative assessment of laser-induced stress waves generated at confined surfaces. *Appl. Phys. Lett.,* **25** (1974), 431-433. doi: 10.1063/1.1655536.

[12] Gil, F.J., Crespo, A., Manero, J.M., Rodriguez, D., Planell, J.A. Mejora de la resistencia al desgaste de titanio y sus aleaciones utlizados para prótesis articulares. *Biomecanica.,* **10** (2002), 20-37.

[13] Gomez-Rosas, G., Rubio-Gonzalez, C., Ocaña, J.L., Molpeceres, C., Porro, J.A., Morales, M., Casillas, F.J. Laser shock processing of 6061-T6 Al alloy with 1064 nm and 532 nm wavelengths. *Appl. Surf. Sci.,* **256** (2010), 5828-5831. doi: 10.1016/j.apsusc.2010.03.043.

[14] Gomez-Rosas, G., Rubio-Gonzalez, C., Ocaña, J.L., Molpeceres, C., Porro, J.A., Chi-Moreno, W., Morales, M. High level compressive residual stresses produced in aluminum alloys by laser shock processing. *Appl. Surf. Sci.,* **252** (2005), 883-887. doi: 10.1016/j.apsusc.2005.01.150.

[15] Golden, P.J., Hutson, A., Sundaram, V., Arps, J.H. Effect of surface treatments on fretting fatigue of Ti–6Al–4V. *Int. J. Fatigue,* **29** (2007), 1302-1310. doi: 10.1016/j.ijfatigue.2006.10.005.

[16] Hu, Y., Yao, Z. Overlapping rate effect on laser shock processing of 1045 steel by small spots with Nd:YAG pulsed laser. *Surf. Coat. Technol.,* **202** (2008), 1517-1525. doi: 10.1016/j.surfcoat.2007.07.008.

[17] Khosroshahi, M.E., Mahmoodi, M., Tavakoli, J. Characterisation of Ti6Al4V implant surface treated by Nd:YAG laser and emery paper for orthopaedic applications. *Appl. Surf. Sci.,* **253** (2007), 8772-8781. doi: 10.1016/j.apsusc.2007.04.084.

[18] Kumar, D., Nadeem Akhtar, S., Kumar Patel, A., Ramkumar, J., Balani, K. Tribological performance of laser peened Ti–6Al–4V. *Wear,* **322** (2015), 203-217. doi: 10.1016/j.wear.2014.11.016.

[19] Liu, H.X., Hu, Y., Wang, X., Shen, Z.B., Li, P., Gu, C.X., Liu, H., Du, D.Z., Guo, C. Grain refinement progress of pure titanium during laser shock forming (LSF) and mechanical property characterisations with nanoindentation. *Mater. Sci. Eng. A,* **564** (2013), 13-21. doi: 10.1016/j.msea.2012.11.087.

[20] Luengo, L., Oliver: Final Project, School of Industrial Engineering of Barcelona, Es. 2008.

[21] Menezes, P.L., Kishore, K., Kailas, S.V. Influence of roughness parameters on coefficient of friction under lubricated conditions. *Sadhana,* **33** (2008), 181-190. doi: 10.1007/s12046-008-0011-8.

[22] Morales, M., Ocaña, J.L., Molpeceres, C., Porro, J.A., García-Beltrán, A. Model based optimization criteria for the generation of deep compressive residual stress fields in high elastic limit metallic alloys by ns-laser shock processing. *Surf. Coat. Technol.,* **202** (2008), 2257-2262. doi: 10.1016/j.surfcoat.2007.12.007.

[23] Peyre, P., Carboni, C., Forget, P., Beranger, G., Lemaitre, C., Stuart, D. Influence of thermal and mechanical surface modifications induced by laser shock processing on the initiation of corrosion pits in 316L stainless steel. *J. Mater Sci*, **42** (2007), 6866-6877. doi: 10.1007/s10853-007-1502-4.

[24] Peyre, P., Fabbro, R., Berthe, L., Dubouchet, C. Laser shock processing of materials, physical processes involved and examples of applications. *J. Laser Appl.,* **8** (1996), 135-141. doi: 10.2351/1.4745414.

[25] Porro, J.A., Molpeceres, C., Morales, M., Ocaña, J.L. Generación de un campo de tensiones residuales de compresión en aluminio 2024-t351 mediante tratamiento por onda de choque generada por láser (laser shock processing). Óptica Pura y Aplicada, **40** (2007), 73-78.

[26] Rozmus, M., Kusiński, J., Blicharski, M., Marczak, J. Laser shock peening of a Ti6Al4V titanium alloy. *Arch. Metall. Mater.*, **54** (2009), 665-670.

[27] Rozmus-Górnikowska, M. Surface modifications of a Ti6Al4V alloy by a laser shock processing. *Acta Phys. Pol. A*, **117** (2010), 808-811.

[28] Rubio-González, C., Felix-Martinez, C., Gomez-Rosas, G., Ocaña, J.L., Morales, M., Porro, J.A. Effect of laser shock processing on fatigue crack growth of duplex stainless steel. *Mater. Sci. Eng. A,* **528** (2011), 914-919. doi: 10.1016/j.msea.2010.10.020.

[29] Sano,Y., Obata, M., Kubo, T., Mukai, N., Yoda, M., Masaki, K., Ochi, Y. Retardation of crack initiation and growth in austenitic stainless steels by laser peening without protective coating. *Mater. Sci. Eng. A*, **417** (2006), 334-340. doi: 10.1016/j.msea.2005.11.017.

[30] Sano, Y., Mukai, N., Okazaki, K., Obata, M. Residual stress improvement in metal surface by underwater laser irradiation. *Nucl. Instrum. Methods Phys. Res. Sect. B,* **121** (1997), 432-436. doi: 10.1016/S0168-583X(96)00551-4.

[31] Sano, Y., Akita, K., Masaki, K., Ochi, Y., Altenberger, I., Scholtes, B. Laser peening without coating as a surface enhancement technology. *Journal of Laser Micro Nanoengineering,* **1** (2006), 161-166.

[32] Sánchez-Santana, U., Rubio-González, C., Gomez-Rosas, G., Ocaña, J.L., Molpeceres, C., Porro, J., Morales, M. Wear and friction of 6061-T6 aluminum alloy treated by laser shock processing. *Wear,* **260** (2006), 847-854. doi: 10.1016/j.wear.2005.04.014.

[33] Sirosky, M.E. Transactions ASME, series D. *Journal of Basic Engineering,* **85** (1963), 279-285.

[34] Sokol, D., Laser shock processing. Technical Bulletin 1, Dublin, OH: Laser Technologies Inc.

[35] Trtica, M., Gakovic, B., Batani, D., Desai, T., Panjan, P., Radak, B. Surface modifications of a titanium implant by a picosecond Nd:YAG laser operating at 1064 and 532 nm. *Appl. Surf. Sci.,* **253** (2006), 2551-2556. doi: 10.1016/j.apsusc.2006.05.024.

[36] Trdan, U., Grum, J. Evaluation of corrosion resistance of AA6082-T651 aluminium alloy after laser shock peening by means of cyclic polarisation and ElS methods. *Corros. Sci.* **59** (2012), 324-333. doi: 10.1016/j.corsci.2012.03.019.

[37] Trdan U, Porro JA, Ocaña JL, Grum J. Laser shock peening without absorbent coating (LSPwC) effect on 3D surface topography and mechanical properties of 6082-T651 Al alloy. *Surf. Coat. Technol.,* **208** (2012), 109-116.

[38] Yakimets, I., Richard, C., Béranger, G., Peyre, P. Laser peening processing effect on mechanical and tribological properties of rolling steel 100Cr6. *Wear,* **256** (2004), 311-320. doi: 10.1016/S0043-1648(03)00405-8.

[39] Yue, L., Wang, Z., Li, L. Material morphological characteristics in laser ablation of alpha case from titanium alloy. *Appl. Surf. Sci.,* **258** (2012), 8065-8071. doi: 10.1016/j.apsusc.2012.04.173.

[40] Zhang, X.C., Zhang, Y.K., Lu, J.Z., Xuan, F.D., Wang, Z.D., Tu, S.T. Improvement of fatigue life of Ti–6Al–4V alloy by laser shock peening. *Mater. Sci. Eng. A,* **527** (2010), 3411-3415.

[41] Ziwen, C., Shuili, G., Shikun, Z., Zhigang, C. Surface profiles and residual stresses on Laser shocked Zone of Ti6Al4V titanium alloy. *Rare Metal Mat. Eng.*, **40** (2011), 190-193.

Int. Journ. of Peening Science and Technology, Vol. 1, pp. 137–154
Reprints available directly from the publisher
Photocopying permitted by license only

Laser Shock Peening of Orthopaedic Ti-6Al-7Nb: Evaluation of Topography, Wetting Characteristics, Microstructure and Residual Stress

X. SHEN[1*], P. SHUKLA[1], F. YAO[2], S. NATH[1], Z. AN[3] AND J. LAWRENCE[1]

[1]*Coventry University, School of Mechanical, Aerospace and Automotive Engineering, Faculty of Engineering, Environment and Computing, Priory Street, Coventry, CV1 5FB, United Kingdom*
[2]*The No.1 Department of orthopaedic Surgery, The No.1 People's Hospital of JiaShan, China*
[3]*Science and Technology on Plasma Dynamics Laboratory, Air Force Engineering University, China*

This paper is focused on a study of wetting characteristics post laser shock peening (LSP) of orthopaedic titanium alloy (Ti-6Al-7Nb) for the first-time. A 10J, 8ns, 1064nm wavelength, Nd:YAG Laser was employed. Residual stress was measured using the incremental hole drilling method. Residual stress results showed maximum compressive stress of -420 MPa, and -100 MPa at a depth of 0.8mm. The surface roughness was increased from 0.15 µm to 0.87 µm after multiple LSP impacts. The contact angle measurements were undertaken by using a sessile drop device with water and ethylene glycol. Both liquids showed that LSP increase the contact angle by 17% and 30.4% respectively using water and ethylene glycol. In addition, further verification was made using the Fowkes model to calculate the surface energy. This yielded the total energy, diversion and polar component to have reduced. The increased contact angle of LSPned samples were affected by combination of increased surface roughness and decreased surface energy. The findings in this study not only form a base for further research, but also reveal the possibility of strengthening titanium implants and rendering them to become more biocompatible.

Keywords: *LSP, wettability, contact angle, Ti-674-Nb, residual stress, SEM, 3-D profiling*

Corresponding author's e-mail: s673864902@126.com

1 INTRODUCTION

Laser shock peening (LSP) has been successfully applied in aeronautic and auto industry over the last two decades. Over the years, researchers have dedicated time to improve the mechanical properties of metallic materials such as fatigue life, wear, and corrosion resistance using LSP. Recently, researchers are also investigating the effect of laser shock peening in another area. In particular, the biological properties of orthopaedic implants, especially the wettability. The wettability of orthopaedic implants is one of the most determining factors in efficiently governing osteogenic activity, involving adhesion, proliferation and differentiation of osteoblasts cells. For the majority of implant materials, wettability is fixed [1-5]. How to change the wetting characteristics in order to improve the biocompatibility of implants without changing surface chemical components has become a new research focus.

Some researchers have already started to do some researches about the effects of LSP on contact angles of metals. Specifically, Vinodh *et al.* [6-7] analysed the effect of LSP on the dynamic corrosion rate of magnesium. As one important property, wettability was also determined and the contact angles of peened samples were increased by 66%. Moreover, Prabhakaran *et al.* [8], employed low energy laser shock peening without coating (LSPwC) to measure the wettability of AISI 304 austenitic stainless steel and found that the hydrophilic unpeened surface was converted into the hydrophobic surface. The contact angle of AISI 304 austenitic stainless steel was significantly increased from 34.24° to 95.75°. Currently, as the dominant material used for implants fabrication, the effect of LSP on the wettability of titanium has not been investigated to-date.

Thus, the focus of this paper was to deploy LSP to change the contact angle of titanium implants for the first-time, since LSP has the capability to change the surface roughness and surface energy, while avoiding the introduction of new chemical substances. Moreover, a Ti-6Al-7Nb titanium alloy was employed due to its excellent biocompatibility and mechanical properties compared Ti-6AL-4V. It is also known that vanadium (V) would be released into the body environment when the surface oxide layer is broken, causing ion toxicosis [9]. Nevertheless, in Ti-Al-67-Nb, niobium (Nb) does not have such a problem. Thus, Ti-6Al-7Nb has more advantage than the most widely used Ti-6Al-4V alloy. However, with orthopaedic implants materials in general, processing stable mechanical properties is necessary, with excellent biocompatibility is also being mandatory. As discussed in previous literatures, LSP can greatly improve the mechanical properties of metal materials. But if this technique needs to be used for implant applications, then the biocompatible aspect of it should be considered too. Our previous findings showed that improvement of wear resistance in Ti-6Al-7Nb alloy subjected to LSP [10] can be achieved. Adding to that, this study has formed a

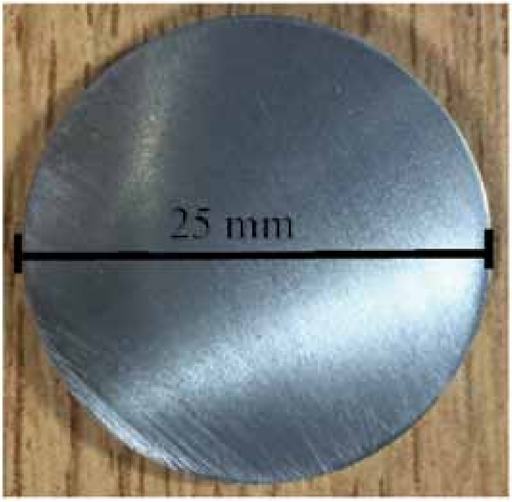

FIGURE 1
An optical image of Ti-6Al-7Nb alloy experimental sample.

TABLE 1
Elemental analysis of Ti-6Al-7Nb alloy (Astm F1295 Rev 11).

Element	Al	Nb	Ta	Fe	N	O	C	H2	Ti
Wt.%	6.1	6.88	0.5	0.19	0.008	0.166	0.04	0.002	Bal

future research stream for strengthening and rendering titanium implants to becoming more biocompatible.

2 MATERIAL AND METHODS

2.1 Details of Ti-6Al-7Nb alloy and sample preparation

Ti-6Al-7Nb samples (show in Figure 1 with its elemental composition in Table 1) were cut into φ25mm x8mm, grinded from 300μm to 1200μm grit size, SiC abrasive paper in stages until the material comprised of Sa (arithmetic mean height) 0.15 μm surface finish. Two samples were used for the laser LSP experiments and one for the analysis on the untreated areas. The etching reagent was 100ml beaker in 20ml Kroll's reagent in which the samples were immersed to reveal surface integrity. Samples were then prepared to the size 10mm × 10mm using wire electro-discharge machining and then immersed in etching solution for 20 seconds then washed in deionized water, dried in the fume hood for the microstructural analysis.

TABLE 2
Laser shock peening parameters employed for the surface treatment of Ti-6Al-7Nb.

Parameters	Value
Pulse energy (J)	6.5
Laser wavelength (nm)	1064
Spot diameter (mm)	3
Radiance Density ($W/mm^2/Sr^{-1}/\mu m$) [11-13]	2.52
Number of laser impacts	1
Overlapping rate (%)	50
Pulse duration (ns)	8
Divergence (mrad)	0.5
Pulse Repetition Rate (Hz)	5

2.2 Laser shock processing method

The LSP experiments were conducted by a Q-Switched Nd:YAG laser (LPY10J; Litron, Rugby, UK), using a wavelength of 1064nm and 8ns pulse width. The laser comprised of a flat-top beam and a M^2 value of 1.99 with a beam divergence of 0.5 mrad. The pulse energy was 6.5J per pulse with a spot diameter was 3 mm focused using a fused silica lens of 50mm diameter. This resulted to a power density of $11.5GW/cm^2$ and a shock pulse pressure of 5.77 GPa in Table.2. The LSP experiment overlap was 50% with 3 impacts according to the one peening sequence presented in Figure 2(b). The water layer was used as the confinement layer, while coating absorb layer was black tape. Figure 2 (a) presents a schematic diagram of the process and (b) shows one pulse overlapping sequence employed.

2.3 Measurements and characterization

2.3.1 Surface Roughness

A 3-D profiler (Contour GT-K, Bruker, Germany.) was employed to measure surface roughness of the Ti-6Al-7Nb alloy before and after LSP. The scanned area for surface roughness determination was 5×5 mm^2 and was measured x5 to ensure the surface roughness values were the same and consistent.

2.3.2 Incremental Residual Stress

The cross-section residual stress was tested by using the incremental hole drilling method with a system developed by Stresscraft, UK. The strain relaxation was measured by wired gauges in a standard three-gauge rosette (two gauges at 90° with a third at 45°). The holes were incremen-

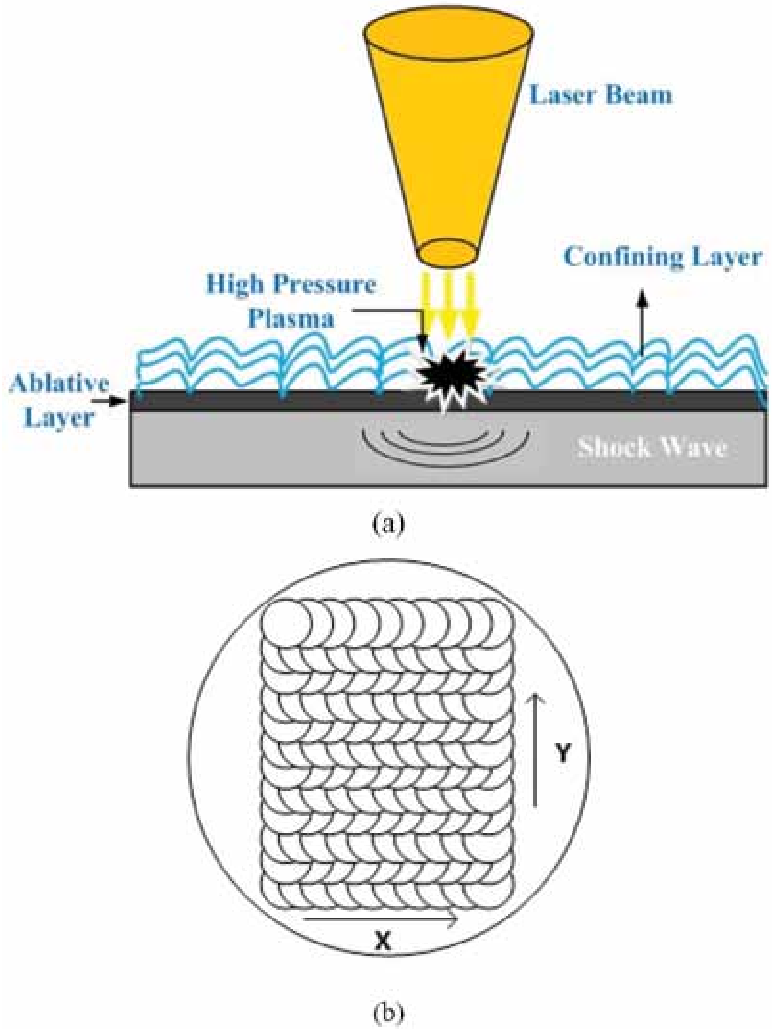

FIGURE 2
A schematic diagram of the laser shock peening process in (a); and (b) the pulse overlapping sequence employed for the laser shock peening surface treatment of Ti-6Al-7Nb [10].

tally drilled with a diameter of 2mm and a maximum depth of 1mm. The relaxed strains were recorded at 13 different increments. Four increments were of 32 μm, and further four increments were of 64 μm. Additional 8 increments were of 128 μm, to a total hole depth of nearly 1 mm. The data were interpreted by Stresscraft RS INT software. Young`s modulus of 105 GPa and Poission`s ration of 0.36 were the input properties in order to calculate the residual stresses.

2.3.3 Wettability

The surface wettability characteristic was measured by using goniometry instrument (DAS 100, DAS, Germany) at room temperature (20°C). The droplet volume of 250 μl and was separately filled with distilled water and ethylene glycol. Each time, 5μl testing liquid was dropped on the surface of the samples. The goniometer calculated the contact angle thereafter, with a processing time of 10 secs. Five sets of contact angles were measured for each sample at different locations to validate the consistency of the data.

3 RESULTS AND DISCUSSION

3.1 Microstructure observation of Ti-6Al-7Nb

The grain refinement has significant relationship with the mechanical properties of the metal alloys. Figure 3 shows the optical cross-section of Ti-6Al-7Nb alloy before and after LSP. From both images coarse grains are distributed non-uniformly over the cross-section. According to grain intercept method, the coarse grains of as-received sample was 6.25 μm, while that of LSPned sample was 3.71 μm. Therefore, the refinement percentage of coarse grain is 68%.

SEM was also used to evaluate the microstructure of the Ti-6Al-7Nb alloy. Figure 4 presents the SEM observations of the untreated and the surface after LSP. As shown in Figure 4, the original microstructure of Ti-6Al-7Nb alloy consists of globular and acicular α and residual β [14 - 17]. The acicular and globular α distribute non-uniformly that the grains are coarse-grains and have clear phase boundaries. Inside the coarse α-grains, there are lots of fine α-rains which possess different grain orientations as shown in Figure 4(b). The grain boundaries between the fine α-grains are clear. The average fine grain size of as-received samples is 266.6 nm. Having said that, the grains decreased after LSP to 150 nm which is about 78% reduction and is exceptional reduction indicating a strengthen surface.

3.2 Surface roughness

Figure 5 show the 3-D topography of Ti-6Al-7Nb alloy before and after LSP. The untreated samples were polished from 300μm to 1200μm grit size, SiC abrasive paper in stages. Moreover, it can be seen that scratch distributed non-uniformly on the untreated samples. In Figure 5(b) the scratches are non-existent after LSP, particularly in the treated areas, and more micro-grooves and dimples were presented on the surface due to the high-pressure waves from the process generating the dimpling effect that you see with shot peening in general. With that said the roughness after LSP increases from 0.194μm to 0.445μm as shown in In Table 3.

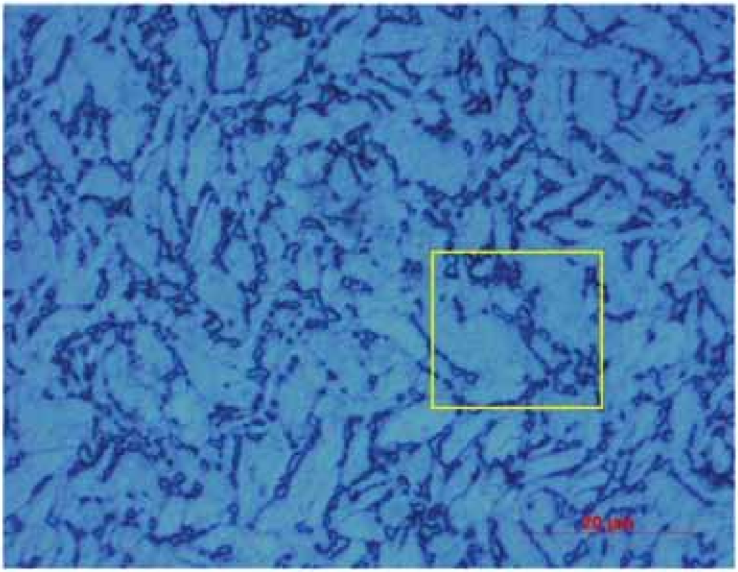

(a)

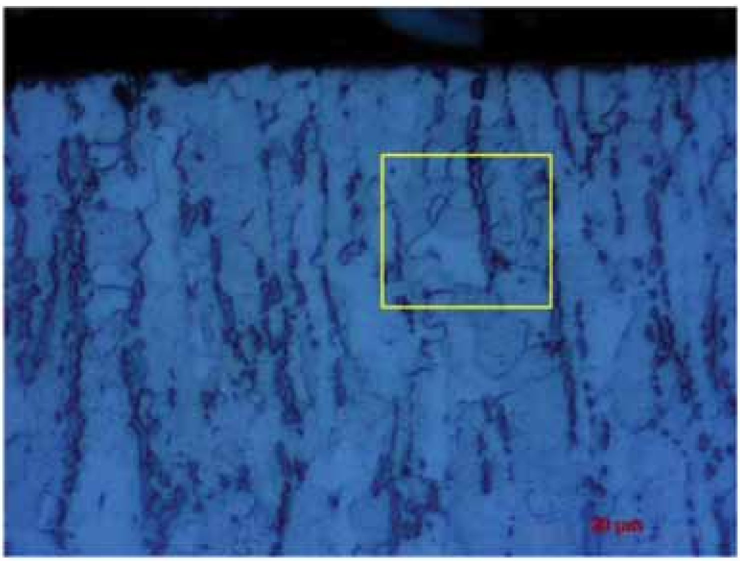

(b)

FIGURE 3
Optical image showing the cross-section of the as-received and laser impacted surface of the Ti-6Al-7Nb in (a); and laser shock peened surface in (b).

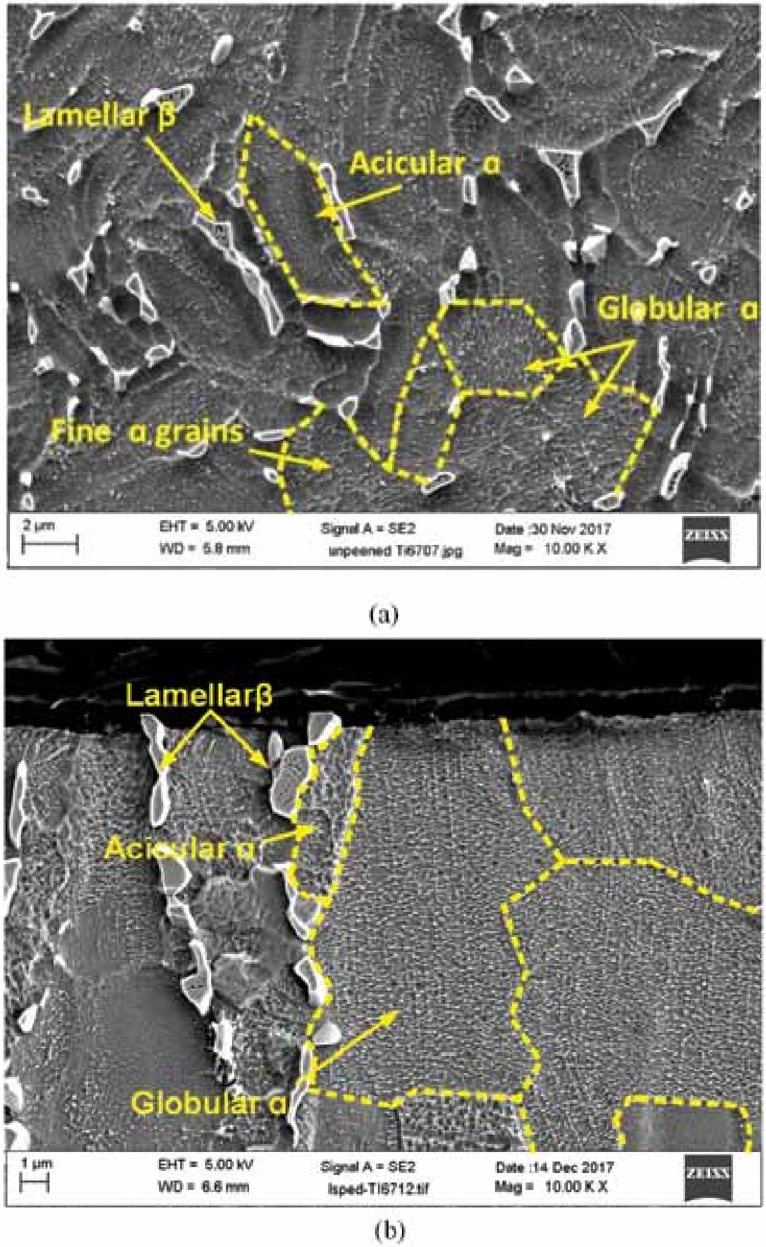

FIGURE 4
SEM image showing the microstructure of the Ti-6Al-7Nb, before and after laser shock peening in both (a) and (b).

What is more, Figure 6(a) and (b) shows the 2-D profile of the unpeened and LSPned Ti-6Al-7Nb alloy. Figure 6(c) and (f) shows cross-sectional 2-D surface

TABLE 3
Surface roughness of Ti-6Al-7Nb in 3-D.

	Sa	**Sp**	**Sq**	**Ssk**	**Sv**	**Sz**
Untreated	0.193.8	5.246	0.252	-0.69	-5.59	10.835
LSPend	0.445	2.596	0.576	-3.78	-12.9	15.47

TABLE 4
A 2-D profile height of Ti-6Al-7Nb.

	Ra	**Rp**	**Rq**	**Rt**	**Rv**
Untreated	0.194	5.246	0.253	10.838	-5.589
LSPed	0.446	2.596	0.578	15.479	-12.883

roughness form X-and-Y axis of the unpeened and LSPned samples. The surface height of the untreated sample scattered from a peak of 0.5μm to a depth of -0.5μm in both X and Y directions. But after LSP, the surface roughness scattered from -1.0μm to -1.5μm in X and ranged from 1.0μm to -1.0μm. As shown in table 4, the average roughness Ra is increased from 0.194μm (unpeened sample) to 0.446μm (peened sample). According to above surface roughness data, the by-product created by LSP which is the surface roughness, could in turn contributes to the changes to the contact angles as the increase in the surface roughness takes place.

3.3 Residual stress

Laser shock peening can introduce a stable compressive residual stress layer on the surface of metallic materials through high pressure shock wave [10]. As shown in Figure 7, the distribution of cross-sectional residual stress before and after LSP resulted to a stable compressive residual stress layer at a depth of 800 μm. Surface residual stress of as-received samples is -60 MPa caused by surface finishing. Onwards along the depth, residual stress varies from 0 MPa to 60 MPa. Surface residual stress of impacted samples was -250MPa. This was around x5 than that of the as-received. Additionally, compressive residual stress is at the highest at a depth of 80 μm, thereby, starting to decrease along the depth to stable value as the intensity of the pressure waves decrease.

3.4 Wettability characteristics

Wetting characteristics have great influence on osseointegration. As a direct parameter reflecting the wetting characteristics of the sample, contact angle θ is affected by many factors including surface roughness and surface energy. Shown from previous work, Caralapatti [7] and Prabhakaran *et al.* [8] found the phenomenon that contact angle θ was increased after laser peened.

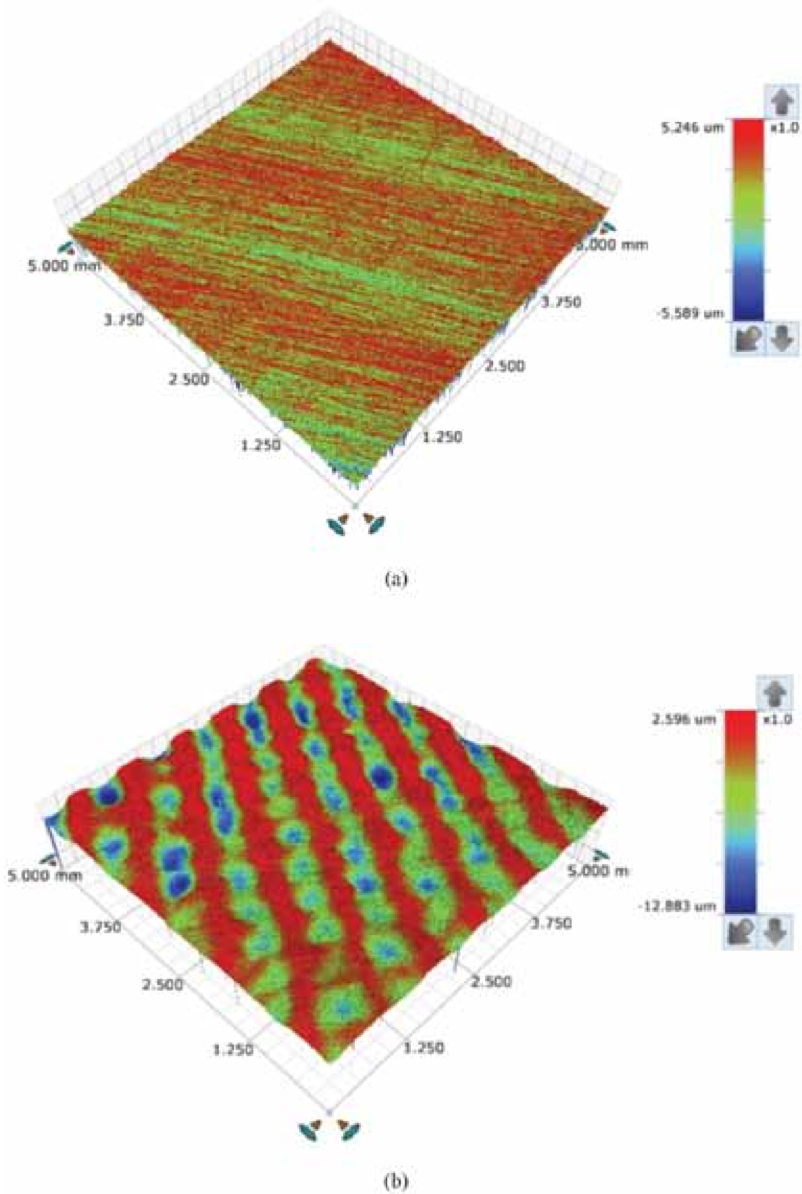

FIGURE 5
A 3D surface map showing the topography of Ti-6Al-7Nb prior-to laser shock peening in (a) and after laser shock peening in (b).

The typical Wendzel model [18, 19] is shown in Figure 7 and equation (1):

$$\cos\theta^{*} = r(\gamma_{SG} - \gamma_{SL}) / \gamma_{LG} \tag{1}$$

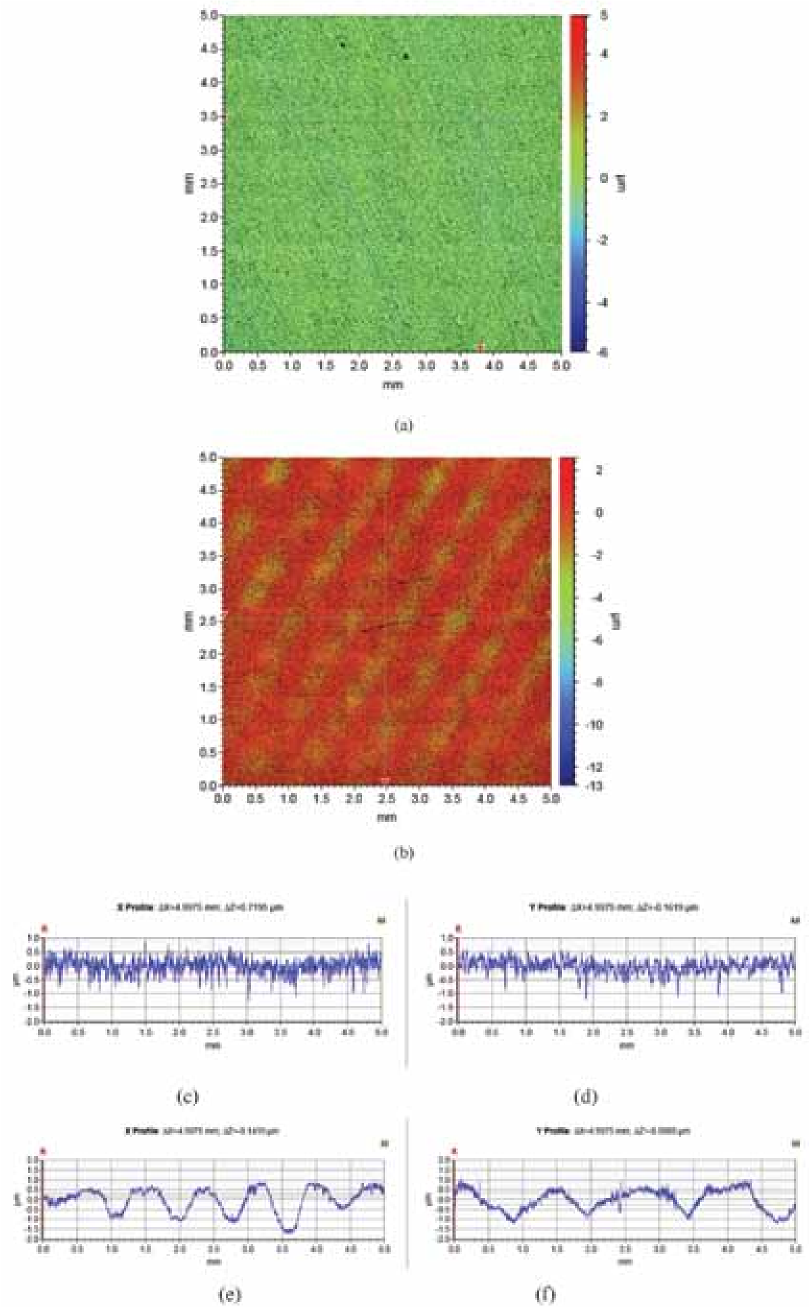

FIGURE 6
A 2-D surface topography of Ti-6Al-7Nb alloy.

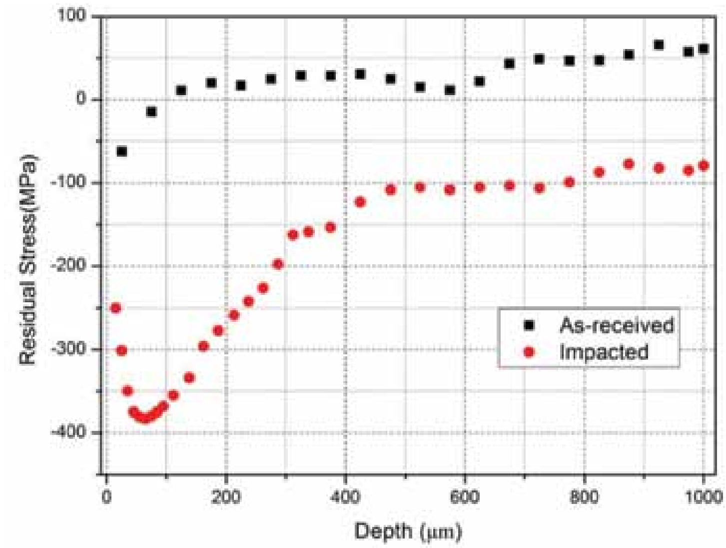

FIGURE 7
A cross-sectional distribution of residual stress of Ti-6Al-7Nb before and after laser shock peening.

Where, $\cos\theta^*$ is the real contact angle; r is surface roughness factor; γ_{SG} is the tension between solid and gas; γ_{SL} is the tension between solid and liquid; γ_{LG} is the tension between liquid and gas.

Therefore, it is necessary to calculate another factor which is the surface energy which can change the difference of contact angle. Fowkes [20 - 21], assumed that surface free energy of solid is a sum of independent components, associated with specific interactions:

$$\gamma_{SG} = \gamma_{SG}^{d} + \gamma_{SG}^{p} + \gamma_{SG}^{h} + \gamma_{SG}^{i} + \gamma_{SG}^{ab} + \gamma_{S}^{o} \tag{2}$$

Where, γ_{SG} is surface free energy of a solid; γ_{SG}, γ_{SG}, γ_{SG}, γ_{SG}, γ_{SG}^{o} are the dispersion, polar, hydrogen, induction and acid-base components, and γ_{SG} is all remaining interactions. Combined with young equation (3), Fowkes suggested equation (4), which used 2 components to calculate solid surface energy.

$$\gamma_{SG} = \gamma_{SL} + \gamma_{LG}\cos\theta \tag{3}$$

$$\frac{\gamma_{\mathrm{lg}}(1+\cos\theta)}{2} = \sqrt{\gamma_{sg}^{d}\gamma_{lg}^{d}} + \sqrt{\gamma_{sg}^{p}\gamma_{lg}^{p}} \tag{4}$$

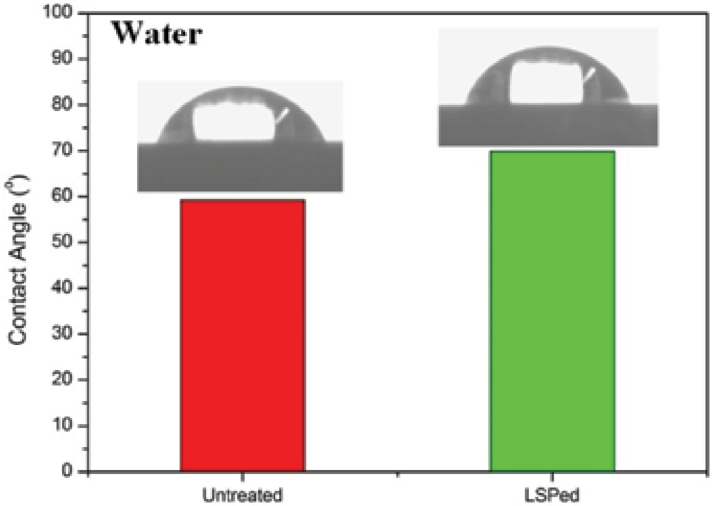

(a)

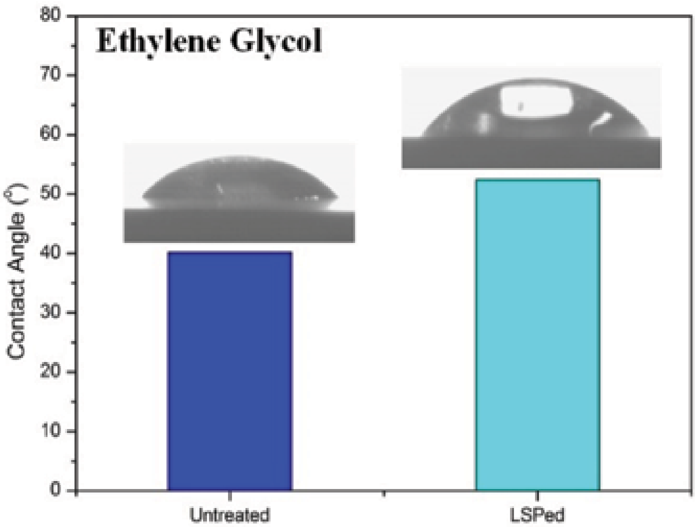

(b)

FIGURE 8
Contact angle images of Ti-6Al-7Nb with (a) water and (b) ethylene glycol.

Where, θ refers to the contact angle; In equation (4), only γ_{sg}, γ_{sg}, are unknown. Thus, using two reference liquid which have γ^{d}_{lg}, γ^{p}_{lg} and γ_{1g} calculate γ_{sg} and γ_{sg}. We used distilled water (γ^{P}= 51.0 mD/m, γ^{D}=21.8 mN/m, γ^{T}=72.8 mN/m) and ethylene glycol (γ^{P}= 19 mD/m, γ^{D}=29 mN/m,

TABLE 5
Wetting characteristic of Ti-6Al-7Nb alloy before and after laser shock peening.

	Liquid	Ra	Sa	γ^D	γ^P	γ^T	Contact angle θ
Untreated	Water	0.15	0.149	42.891	9.864	52.754	59.19
	Ethylene glycol						40.184
LSPed	Water	0.875	0.873	30.326	4.248	34.574	69.818
	Ethylene glycol						52..41

γ^T=48 Mn/m) to calculate the total surface energy including polar component and diverse component. The results are shown in Table 5 and Figure 8.

The results of contact measurements indicate that contact angles are increased by using both liquids. As shown in Table 5 and Figure 8, the contact angle increased from 59.19° to 69.818° with water liquid, and 40.18° to 52.41° with ethylene glycol.

If the valleys of a coarse surface were filled by liquid such as water, then the Wenzel`s model is more suitable. Normally, according to Wenzel Model shown in Figure 8, the contact angle of the LSPned samples should decrease while surface roughness of samples increased. But the contrast result is that contact angle was increased. Thus, Cassie-Baxter model, shown in Figure 9, or mixed regime of both [22 - 24] may be used in this case. The explanation of Cassie-Baxter model suggested that the fluid adhering onto the top of the protrusions would create a pocket of air underneath [25].

The reason why contact angle was increased was because the γ^P, γ^D and γ^T in both liquids were all decreased. High surface energy can lead to low hydrophilicity which meant that low contact angle resulted. Thus, the decreased in surface energy, combined with increased surface roughness increased the contact angle.

Additionally, due to the ablation of LSP, the contaminations, namely; dirt was removed, which contribute to improving the surface free energy [26]. Since the surface free energy of contaminations were low, the removal of contaminations can increasing the surface energy thereby contributing to the biological properties of implants. It is said that contact angle of 70° [27] is considered to be ideal for cell attachment and better bonding with osteoblast which is key for cell adhesion. When implants are serving inside the human body, they undergo different interactions such as cells, proteins and adhesion. What is more important, osteointegration was also influence by surface wettability of implants. However, the effect of LSP on cell adhesion and osteointegration of medical-grade metals have not been investigated.

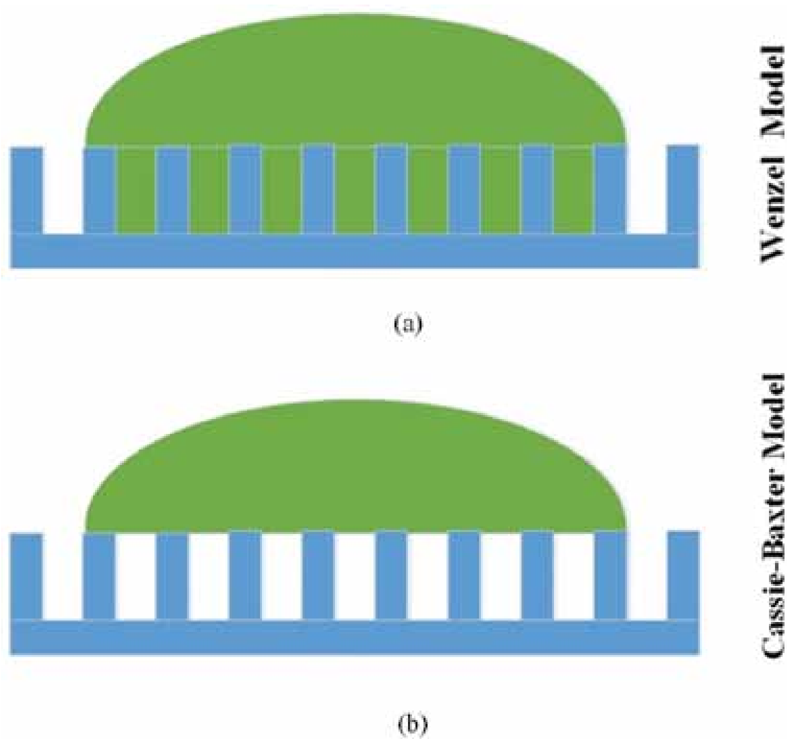

FIGURE 9
The schematic diagrams of (a) Wenzel model and (b) Cassie-Baxter model.

4 CONCLUSIONS

It is very important to provide a strengthening mechanism for implant metals due to the obvious failures resulting to significant damage and loss of patient's time, money and the potential pain *via* repetitive surgeries. Therefore, it proves very useful to investigate the biological effect of LSP strengthening technique on medical-grade metallic materials such as titanium alloys. Thus, the focus of this paper is on the topography, wetting characteristics, microstructure and residual stress which were investigated for the first-time prior-to and post laser shock peening of orthopaedic grade Ti-6Al-7Nb. The wide range of analysis verified and rendered the following conclusions:

1) Three LSP impacts increase the surface roughness by 127%.
2) In the cross-section, the coarse grain size was decreased from 6.25μm to 3.71 μm, while the refinement of fine grain size was from 266.5nm to 150nm.

3) LSP increased the contact angle from 59.19° to 69.81° by using water and 40.18° to 52.41° by Ethylene glycol as result of the decreased surface energy and increased surface roughness.

NOMENCLATURE

Ra	Arithmetical mean roughness value over the entire measured length (µm)
Rp	Maximum profile peak height/ valley depth are the distance from the mean line (µm)
Rq	Average between the height deviations and the mean line (µm)
Rt	Total height of the roughness profile over the length (µm)
Rv	Surface to the highest/lowest point along the sample length (µm)
Sa	The arithmetic mean of the absolute values of the surface departures from the mean plane (µm)
Sp	The height of the highest peak within the defined area (µm)
Sq	The root mean square value of the ordinate values within the definition area (µm)
Ssk	Asymmetry of the profile about the mean plane (µm)
Sv	The absolute value of the height of the largest pit within the defined area (µm)
Sz	The sum of the largest peak height value and the largest pit depth within the area (µm)

Greek Symbols

γ_{sg}	The tension between solid and gas
γ_{SL}	The tension between solid and liquid
γ_{LG}	The tension between liquid and gas
γ_{SG}^{d}	Dispersion component
γ_{SG}^{p}	Polar component
γ_{SG}^{h}	Hydrogen component
γ_{SG}^{i}	Induction component
γ_{SG}^{ab}	Acid-base component
γ^{P}	Polar energy
γ^{D}	Dispersion energy
γ^{T}	Total surface energy

5 ACKNOWLEDGEMENT

This work was supported by the Engineering Physical Sciences Research Council's (EPSRC) laser loan pool scheme run by the Science & Technology Facilities Council (STFC) with the Grant no: EP/G03088X/1, (13250017 – NSL4)).

REFERENCES

[1] Chen, D., Gao, M., Fu, Y., Xu, X., Hao, Z. A facile approach to manipulation of osteogenic activity of orthopaedic implants by in situ electrically controlled wettability. *Electrochimica Acta* **182** (2015), 841-846.

[2] Padial-Molina, M., Galindo-Moreno, P., Fernandez-Barbero, J. E., O`Valle, F., Jodar-Reyes, A. B., Ortega-Vinuesa, J. L., Ramon-Torregrosa, P. J. Role of Wettability and nanoroughness on interactions between osteoblast and modified silicon surfaces. *Acta Biomaterialia* **7** (2015), 771-778.

[3] Rosales-Leal, J.I., Rodriguesz-Valverde, M. A., Mazzaglia, G., Ramon-Torregrosa, P. J., Diaz-Rodriguez, L., Garcia-Martinez, O., Vallecillo-Capilla, M., Ruiz, C., Cabrerizo-Vilchez, M. A. Effect of roughness, wettability and morphology of engineered titanium surfaces on osteoblast-like cell adhesion. *Colloids and Surfaces A: Physicochemical and Engineering Aspects*, **365** (2011), 222-229.

[4] Kulkarni, M., Patil-Sen, Y., Junkar, I., Kulkarni, C.V., Loreenzetti, M., Iglic A. Wettabiltiy Studies of Topologically distinct titanium surfaces. *Colloids and Surfaces B: Biointerfaces*, **129** (2015), 47-53.

[5] Hotchkiss, K.M., Reddy, F.B., Hyzy, S.L., Schwartz, Z., Boyan, B.D., Olivares-Navarrete, R. Titanium surface characteristics, including topography and wettability after macrophage activation. *Acta Biomaterialia* **31** (2016), 425-434.

[6] Caralapatti, V.C., Narayanswamy, S. Analyzing the effect of high repetition laser shock peening on dynamic corrosion rate of magnesium. *Optics and laser Technology* **93** (2017), 165-174.

[7] Caralapatti, V.C., Narayanswamy, S. Effect of high repetition laser shock peening on biocompatibility and corrosion resistance of magnesium. *Optics & Laser Technology* **88** (2017), 75-84.

[8] Prabhakaran, S., Aniket K., G. Vasanth, Kalainathan, S., Shukla P., Vasudevan V. K. Laser shock peening without coating induced residual stress distribution, wettability characteristics and enhance pitting corrosion resistance of austenitic stainless steel. *Applied Surface Science* **428** (2018), 17-30.

[9] Semlitsch, M.F., Weber, H., Streicher, R.M., Schön, R. Joint replacement components made of hot-forged and surface-treated Ti–6Al–7Nb alloy. *Biomaterials* **13** (1992), 781-788.

[10] Shen, X., Shukla. P., Nath, S., Lawrence, J. Improvement in mechanical properties of titanium alloy (Ti-6Al-7Nb) subject to multiple laser shock peening. *Surface and Coatings Technology* **327** (2017), 101-109.

[11] Shukla, P.P., Lawrence, J. Role of laser beam radiance in different ceramic processing: A two wavelength comparison. *Optics and Laser Technology* **54** (2013), 380-388.

[12] Shukla, P., Lawrence J., Zhang, Yu. Understanding Laser-beam brightness: A Review on a New Prospective in Materials Processing', *Optics and Lasers in Engineering* **75** (2015), 40-51.

[13] Shukla, P.P., and Lawrence, J. Identification of Optical Parameters for Determination of Radiance, *Journal of Optics*, Optical Society of India **44** (2015), 12-19.

[14] Oliveira, D.P., Prokoiev, E., Sanches, L.F.R., Valiev, R.Z., Botta, W.J., Junior, A.M.J., Bolfarini, C. Surface chemical treatment of ultrafine-grained Ti-6Al-7Nb alloy processed by severer plastic deformation. *Journal of Alloys and Compounds* **643** (2015), 241-245.

[15] Chlebus, E., Kuznicka, B., Kurzynowski, T., Dybala. B. Microstructure and mechanical behavior of Ti-6Al-7Nb alloy produced by selective laser melting. *Material Characterization* **62** (2013), 488-495.

[16] Huang, H., Wu, C., Sun, Y., Yang, W., Lee. T. Surface nanotopography of an anodized Ti-6Al-7Nb alloy enhances cell growth. *Journal of Alloys and Compounds* **615** (2014), S648-S654.

[17] Rafieerad, A.R., Bushroa, A.R., Nasiri-Tabrizi, B., Vadivelu, J., Baradaran, S., Mesbah, M., Zavareh A. M. Mechanical properties, corrosion behavior and in-vitro bioactivity of

nanostructured Pd/ PdO coating on Ti-6Al-7Nb implant. *Materials and Design* **103** (2016), 10-24.

[18] Yamaguchi, M., Suzuki, S., Sasaki, S., Chiba, T., Itoh, N., Hoga. M. Fabrication of nano-periodic structures and modification of the Wenzel model to estimate contact angle. *Sensors and Actuators A: Physical* **212** (2014), 87-92.

[19] Han, T., Shr, J., Wu, C., Hsieh., C. A modified Wenzel model for hydrophobic behaviour of nanostructured surfaces. *Thin Solid Films* **515** (2017), 4666-4669.

[20] Kwok, S.Y., Li, D., Neumann. A.W., Fowkes. Surface tension component approach revisited. *Colloids and Surfaces A: Physicochemical and Engineering Aspects* **89** (1994), 181-191.

[21] Spelt, J.K., Neumann. A. W. Solid surface tension: the equation of state approach and the theory of surface tension components. Theoretical and conceptual considerations. *Langmuir* **3** (1987), 588-591.

[22] Robert D. A., Neumann, W. Contact angle patterns on Low-Energy surfaces. *Advances in Colloid and Interface Science* **206** (2014), 46-56.

[23] Cansoy, C.E., Erbil, H.Y., Orhan A., Tayfun A. Effect of pattern size and geometry on the use of Cassie-Baxter equation for surperhydrophobic surfaces. *Colloids and surfaces A: Physicochemical and Engineering Aspects* **386** (2011), 116-124.

[24] Ugur C., Cansoy. C. E. Applicability of Cassie-Baxter equation for superhydrophobic fluoropolymer-silica composite films. *Applied Surface Science* **335** (2015), 99-06.

[25] Jothi Prakash, C.G., Clement Raj, C. Prasanth, R. Fabrication of zero contact angle ultra-super hydrophilic surfaces. *Journal of Colloid and Interface Science* **496** (2017), 300-310.

[26] Thayawat U., Suwit S., Chotika V., Viboon T.. Laser cleaning performance and PAHs formation in the removal of roasting marinade stain. Food and Bioproducts Processing **102** (2017), 81-89.

[27] Jin, W., Wu, G., Feng, H., Wang, W., Zhang, X., Chu, P.K. Improvement of corrosion resistance and biocompatibility of rare-earth WE43 magnesium alloy by neodymium self-ion implantation. *Corrosion Science* **94** (2015), 142-155.

Int. Journ. of Peening Science and Technology, Vol. 1, pp. 155–180
Reprints available directly from the publisher
Photocopying permitted by license only

Laser Cleaning of Grey Cast Iron Automotive Brake Disc: Rust Removal and Improvement in Surface Integrity

Y. F OGBEKENE[1], P. SHUKLA[1,*], Y. ZHANG[2], X. SHEN[1], S. PRABHAKARAN[3], S. KALAINATHAN[3], K. GULIA[4] AND J. LAWRENCE[1]

[1]*School of Mechanical, Aerospace and Automotive Engineering, Coventry University, Priory Street, Coventry, CV1 5FB, United Kingdom*
[2]*University of Lincoln, Brayford Way, Brayford Pool, Lincoln, LN6 7TS, United Kingdom*
[3]*Centre for Crystal Growth, Department of Physics, School of Advanced Sciences, Vellore Institute of Technology, Vellore, 632014, Tamilnadu, India*
[4]*Faculty of Science and Engineering, School of Engineering, University of Wolverhampton, Priorslee, Telford, TF2 9NN, United Kingdom*

There is a great need for removal of rust and surface damage from corroded engineering parts. This enables the retention of strength and increased longevity of metals and alloys in general. The use of lasers for cleaning, polishing and ablation has proven to be effective and promising overtime. This research is focused on a parametric study of laser cleaning a corroded grey cast iron brake disc. A continuous wave CO_2 laser having a wavelength of 10.6μm was used for the study. A systematic approach was employed for the experiments where one parameter was changed while other parameters remained constant. Additional effects of laser cleaning were predicted by a Gaussian process regression approach. The results revealed that the best parameters which cleanly removed the rust were 60W of laser power, 900mm/s traverse speed, and a spot size of 722μm. The enhancement of surface microhardness of laser cleaned specimen was 37% compared to the rusted specimen surfaces. The roughness of the laser cleaned surface was, 1.29μm while the rusted surface comprised of 55.45μm (Ra). Microstructural analysis showed a presence of randomly distributed graphite flakes surrounded by a pearlitic matrix containing ferrite and cementite after laser cleaning. This was similar to that of the un-rusted surface. The hardness, roughness and microstructural content were in close relation with the respective properties of the un-rusted automotive brake disc. This showed that the mechanical and physical properties of the brake disc were not altered negatively during the

* Corresponding author's e-mail: ac5190@coventry.ac.uk

laser cleaning process. Implementation of the laser-cleaning technique in automotive and manufacturing industries should be embraced as it provides a faster, safer and cheaper way of enhancing the surface integrity of components and also paves way for other surface enhancement methodologies to be applied such as blast cleaning or laser shock cleaning for inducing extra strength, by beneficial residual stresses.

Keywords: Cast iron, laser cleaning, laser polishing, ablation, corrosion, surface integrity, automotive, brake disc

1 INTRODUCTION

1.1 Overview

Rusting is an unavoidable natural phenomenon that has been a global menace for ages. This has caused so much damage overtime ranging from crude farm tools to valuable historical artefacts, modern-day industrial, engineering and domestic parts made from metals and alloys. The annual cost of corrosion worldwide is $2.2 trillion which is over 3% of the world GDP [1]. This brings the need to counter/remove rust. Over the years, rust removal has evolved from a more primitive technique that includes scrubbing, the use of white vinegar, salt, lime, baking soda to the use of chemicals and other modern rust removal techniques [2]. These techniques are less effective and consumes both time and energy. There is therefore an increasing need to use effective and quicker ways of removing rust which has led to the use of industrial lasers.

Metals and alloys are used in our day-to-day activities be it domestic, automobile or industrial. These metals and alloys are constantly exposed to the surrounding which acts chemically on it causing degradation of its part leading to corrosion [3]. Corrosion is a chemical or electrochemical reaction that causes the disintegration of an engineering material [4]. Rusting is specific to iron and its alloys [5]. It occurs when iron reacts with moist air or water to form iron oxide [6]. Therefore, rusting leads to a decrease in the performance, life span and failure of engineering materials [7]. Since rust affects irons and its alloys in which cast iron falls into that subset of metals, a brake disc made of cast iron was used as a case study for this research with the aim of the obtaining the optimal laser parameters that are most suitable for the removal of rust from metals and alloys.

1.2 Research background

Laser cleaning involves the removal of rust/corrosion from the surface of metals [8]. It involves the removal of debris, contaminant and impurities (silicon or rubber) by laser irradiation [9]. Varieties of industrial laser cleaning applications are done using a pulsed fibre laser with high repetition rate, short pulse and high peak power [10]. During the process of laser cleaning, it is necessary that the physical and mechanical properties of the base metal are not modified [11].

Similar research on laser cleaning of corroded layers due to environmental pollution on metallic objects showed that the rate of laser ablation increased with increasing laser fluence [12]. They suggested the fluence should be within the ablation domain, that is, greater than the vaporization threshold but less than the saturated domain [12]. The base metal is affected once it reaches the saturated domain [13]. Zhenyong *et al.* [14] gave a similar viewpoint to Siatou *et al.* [12], but argues that the cleaning efficiency of a pulsed Nd: YAG laser is better than that of the CO_2 laser. They further explained that the high laser absorbency of rust particles plays a vital role in the cleaning mechanism [15]. Irrespective of the preferred use of pulsed lasers over continuous wave CO_2 lasers for cleaning, a successful rust removal process can still be carried out [16]. Also, proper laser cleaning does not damage the metal substrate nor negatively alter its mechanical properties and microstructure [16]. Kane [17] suggested that most cleaning processes are unique and the best parameter for cleaning is to find the correct balance between the power, wavelength, spot size and traverse speed. The effect of laser cleaning on a metallic part's hardness, microstructure and surface roughness was previously reported [18].

Creek [19] suggested that rust reduces the hardness and strength of metals. As the amount of rust reduces, hardness increases. A review of laser cleaning and its effect on the vertical variation over a measured distance (surface roughness) showed that when the average surface roughness increase (more than the wavelength of the laser), absorption also increased [20]. For a smooth surface, where average roughness is less than the laser's wavelength, the absorptivity would reduce [20]. Przestacki *et al.* [21] in the research of cleaning superficially corroded metals by CO_2 lasers found the Ra value to be 1.75μm. Adebayo [22] found in a research on the relationship between graphite flake sizes and the mechanical properties of grey cast iron that a large, closely-packed flake reduces the strength as well as the hardness. However, Holtzer et al. [23] reported that the presence of a larger flake size increases the ease of machining, good dampening capacity and dimensional stability.

1.3 Research rationale

The global annual cost of corrosion damage is 2.5 trillion USD [24] . This value was approximately 3.4% of the world's GDP. Around 15 to 35% (375 to 875 billion USD) of that cost could be saved globally if corrosion prevention was implemented [25]. In 2002, the United States Federal Highway Administrator (FHWA) released a two-year research on the direct cost of metallic corrosion in nearly every U.S industrial sector [26]. These affected sectors include: manufacturing; production; infrastructures; transportation; aerospace; automobile and many more [26]. Koch *et al.* [26] *via* a study on corrosion cost and preventive strategies, that the annual direct cost of corrosion was estimated at a staggering 276 billion USD which is 3.1% of the nation's gross domestic product. The production and manufacturing sector accounted for 17.6 billion USD which is quite large. The transportation sector accounts for 21.5% (29.7 billlion USD) of the total cost [26] . From these case studies, there are key reasons that justifies the need for this research. In particular, laser rust removal helps to decrease the cost of replacing and maintaining metallic engineering parts [27, 28]. The life-span of metallic engineering components can be greatly increased using laser rust removal technique. It also increases profitability and productivity in manufacturing industries by saving production and maintenance time and prevents sudden failure of parts. Controlling corrosion and rusting also ensures the mechanical and physical properties such as hardness, surface roughness, the microstructure is retained even over its life-span post laser cleaning. Furthermore, since rusting occurs naturally, it helps to reduce and control its effect to the barest minimum. Laser-based industrial processes exist for removal of rust, however, very little published work addresses the fundamental effects of laser material interaction post laser cleaning, particularly, for automotive brake disc which is a novel application. This work not only aims to address the parameters appropriate to remove rust/corrosion from an automotive grey cast iron component, but also aims to improve the surface integrity of the component for longer functional life, and reduced maintenance costs.

1.4 Mechanism of rust removal

The process of removing material from a metallic surface through laser irradiation can be achieved through various mechanisms [29]. These mechanisms can be grouped into three major groups that are evaporation processes (ablation and selective vaporization), impact processes (dry and steam cleaning, spallation, photon pressure, and evaporative pressure) and vibration processes (angular laser cleaning and transient thermal heating) can also act as a remedy for cleaning surfaces [30]. The mechanism of laser rust removal using CO_2 laser was based on stimulated emission phenomenon, heating, absorption, melting, and vaporisation. The rust deposition was a thin loose transition layer which was removed with the laser irradiation. This layer is mainly made of Fe_2O_3 and Fe_3O_4 particles [16], as the rusted surface is exposed to high laser power, a laser-absorptive field is naturally formed. This was achieved by the breaking down and ionization of the plasma above the surface. At the same time, the output temperature is above the melting point of the rust particles [18]. The laser energy absorbed is transformed into air or plasma intrinsic energy [16] as shown in Figure 1. In relation to the temperature, the surface absorbs laser power leading to enthalpy (equal to the internal energy of the system plus the product of pressure and volume). The corroded surface is removed since the surface temperature is greater than the vaporisation temperature of the material [31]. Other laser cleaning procedures, include; shot blasting, blast cleaning and shock laser cleaning [32 - 34]. These processes

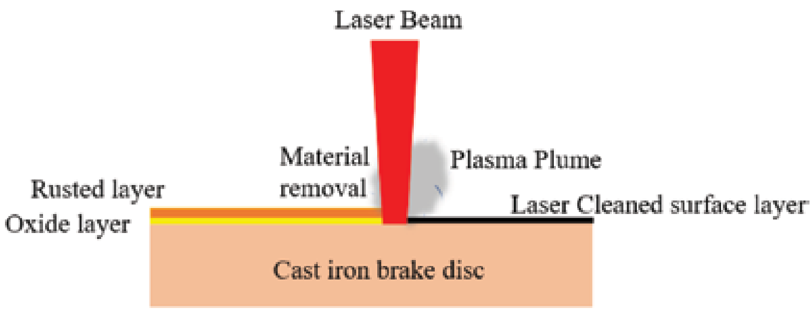

FIGURE 1
A schematic representation of laser rust removal process.

involve different mechanism for cleaning. A schematic representation of rust removal using a laser is shown in Figure 1.

2 EXPERIMENTAL AND ANALYTICAL TECHNIQUES

2.1 Background of test material

The material used for the experiment was both rusted and un-rusted grey cast iron automotive brake disc of a Vauxhall Astra diesel car. The samples were cut from the brake disc into small blocks for ease of laser surface treatment (see Figure 2(b)). The grey cast iron brake disc composes of 3.25 to 3.5 wt.% carbon, 0.050 to 0.45 wt.% chromium, 0.15 to 0.40 wt.% copper, 91.9 to 94.2 wt.%, iron, 0.50 to 0.90 wt.% manganese, 0.05 to 0.10 wt.% molybdenum, 0.050 to 0.20 wt.% nickel, 0.12 wt.% phosphorus, 1.8 to 2.3 wt.% silicon and 0.15 wt.% Sulphur [35]. The availability of grey cast iron in abundance makes it the second cheapest of all engineering metals [36]. Due to the operating conditions of the brake disc, it is required to have a good compressive strength, high friction coefficient, considerably lightweight, good thermal capacity and economically viable [37]. The ease of manufacture, cost, anti-wear resistance properties and thermal stability makes grey cast iron suitable for the brake disc [38]. The microstructural content contains flaked graphite in a matrix of pearlite and some traces of ferrite [23]. The manufacturing process of the brake disc includes casting, cutting, and forming [39]. It undergoes some heat treatment to change its microstructure, thereby, boosting its mechanical properties [38, 39].

2.2 Preparation of sample prior to laser cleaning

Pre-laser treatment involves the preparation of samples prior to laser beam exposure. The brake disc was in its as-received state (un-rusted) at the onset of the experiment. The basic steps in the pre-laser treatment involved induced rusting and cutting. These steps were necessary only for the sake of

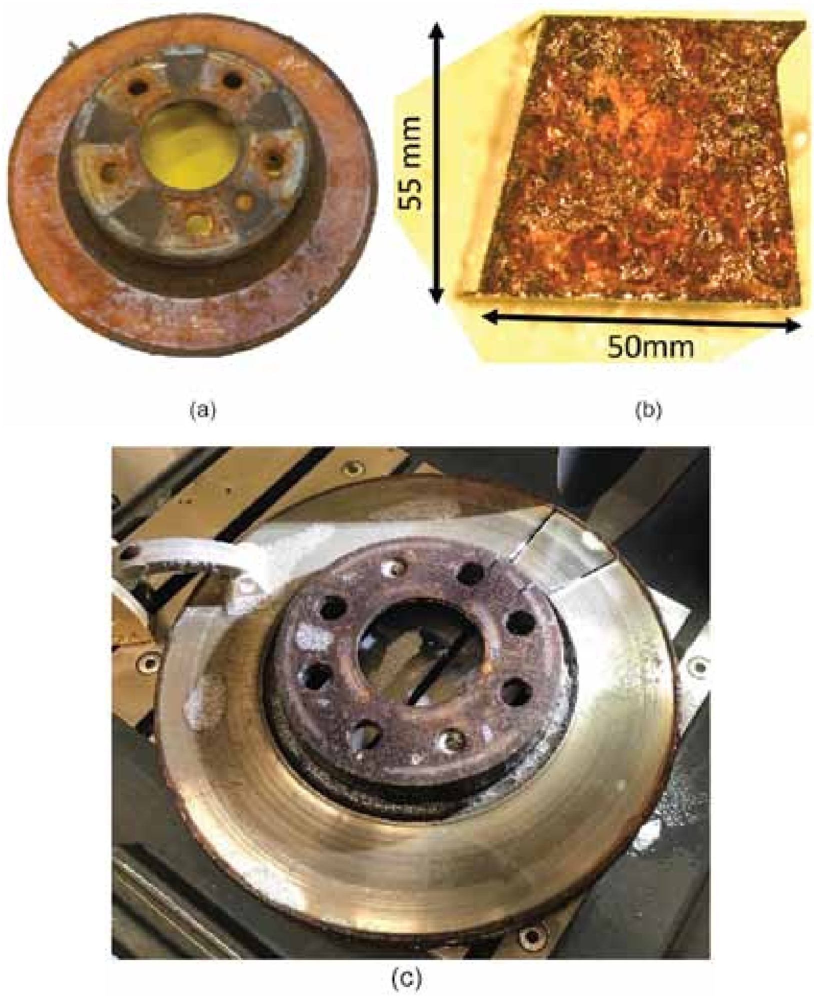

FIGURE 2
Illustrates optical images of the rusted brake disc in (a); a cut bake disc into smaller parts in (b) and (c) the un-rusted automotive brake disc.

this experiment. The brake disc was exposed to the atmosphere to enable moisture (water and air) to act on it for several weeks. By the third week significantly, uniform rust was formed throughout the entire surface of the brake disc as seen in Figure 2. The uniformly rusted brake disc was then cut into 20 parts (samples) of roughly equal size to ensure that samples were sufficient for the experiment. Figure 2(a) shows the rusted brake disc and the cut sample into smaller parts prior to laser cleaning in Figure 2(b) and the un-rusted complete brake disc in Figure 2(c).

TABLE 1
Laser processing parameters employed for laser rust removal.

Power (W)	Traverse speed (mm/sec)	Beam diameter (mm)	Radiance Density ($W/mm^2/Sr^{-1}/um^{-1}$)
10 to 85	30 to 3000	0.71 to 1.69	2.74 to 132.35

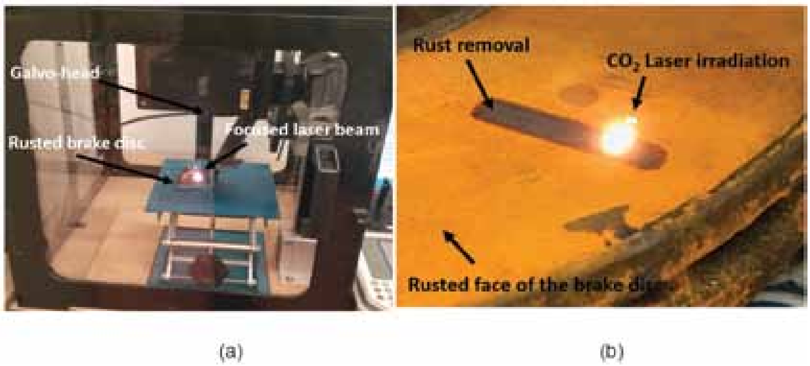

FIGURE 3
Optical images showing experimental set-up of the CO_2 laser rust removal process in (a) and method of rust removal in (b).

2.3 Laser cleaning process

Laser cleaning experiments were conducted using a continuous wave (CW) Rofin multiscan CO_2 laser (Hamburg, Germany). The laser has a wavelength of 10.6μm and a maximum power output of 85W. Experimental parameters applied and varied are namely: laser power, traverse speed, and spot size (see Table 1). A systematic approach was adopted for the experiments where one parameter was changed in an orderly pattern while other parameters were kept constant. The experiment involved 20 different samples with a total of 27 trials each processed with a unique set of processing parameter. First, the power was varied between 10W to 85W (maximum power), while other parameters were kept constant. The Radiance density (brightness) was determined using our previous technique [40 – 42], and ranged from 2.74 to 132.35 $W/mm^2/Sr^{-1}/\mu m^{-1}$. Traverse speed was varied between 30 to 3000mm/s with other parameters kept constant. The focal distance was also varied to obtain the correct laser beam diameter. Each of the cut samples were mounted on the processing table and exposed to the CO_2 laser beam to remove the top rust surface (see Figure 3(a)). Figure 3 also shows the experimental set up during the laser cleaning process and the method of rust removal.

2.4 Material removal measurement

The micrometre screw gauge was used to measure the thickness of the samples before and after laser rust removal. The unrusted surface thickness of the sample was also measured, and the difference in thickness was noted. The process was used to determine the ablation depth as well as measure the amount of material removal post laser cleaning. Measurements were taken five times on every sample to ensure a level of accuracy, and the average was then calculated.

2.5 Microhardness testing, topography, sample preparation and etching procedures

The Mitutoyo MvK-H1 hardness tester (Kawasaki, Japan) was used to measure the Vickers microhardness. A maximum load of 1000N was applied on the samples with a 5 secs dwell time. A Bruker contour GT profilometer with the vison64 software was used to measure the surface profile of the samples with the aim of quantifying the roughness. Polished cast iron specimen usually shows little or no matrix microstructure. Etching was conducted on the unrusted, totally rusted and the best laser-cleaned samples. The etchant used for the grey cast iron samples was Nital. Prior to etching, the samples were cut down from the whole automotive brake disc to smaller pieces. Samples were cross-sectioned for microstructural analysis. Selected samples were then mounted using a standard Vari-set 20 cold mounting powder and the quick-set cold mounting liquid. The mixing ratio was 2-parts powder to 1-part liquid by volume. The samples were kept at the center of the mount with the surface to be polished facing downward. The polishing process was conducted in 6 phases. A 9µm DiaDuo-2 water-based diamond suspension containing monocrystalline diamonds. A MD-Dur cloth was used, and the process took place at a speed of 150rpm for 10mins. A 6µm DiaDuo-2 diamond suspension with a MD-Dur cloth at a speed of 150rpm for 7mins. A 3µm DiaDuo-2 paste diamond suspension polish liquid was used with a MD-Dac cloth at 150rpm for another 7mins. A 1µm DiaDuo-2 paste diamond suspension polish liquid was used with a MD-Dac cloth at 150rpm for 3mins. Final polishing was then carried out using the colloidal silica suspension (0P-S) as the cooling lubricant for 3mins at 150rpm. To obtain a top-notch polished surface, the sample was then transferred to the Buehler Vibromet 2 vibratory polisher for 2 hours.

2.6. Optimisation of properties using gaussian process regression

A Gaussian process regression (GPR) approach [43] was used to predict the effects of laser cleaning with respect to the process parameters based on the experimental data. GPR is a reliable and a well-known method in machine learning that can be deployed using various types of data. It is a non-parametric approach and has been used widely to solve varieties of problems such as material properties, thus, can be deployed to understand the effects herein, in relation to laser processing related issues.

3 RESULTS AND DISCUSSION

3.1 Selection of laser cleaning parameters

Figure 4 represents a rusted surface which was removed by varying the laser parameters. The constituent of the rusted surface includes heavily corroded regions, corrosion cracking, and some areas that are partially rusted. The alteration of laser power from 10 to 85W (max power) produced various level of rust removal. At 10W, it was observed that a very low level of rust was removed with no visible cleaning effect. As the laser power was ramped up to 20W, the effect of rust removal became visible, but surface still contained significant rust. Upon applying 30W to 40W of laser power, there was a moderate level of rust removal. As the laser power was increased to 50W, there was a considerable amount of rust removed. At 60W, the rust removal was increased, but still contained areas where rust was visible. Although, it offered the best effect as ramping up the laser power to 70W significantly removed the rust but also affected the base metal. Thereafter, the rust was removed but the base metal was considerably altered due the increased laser power applied, and the substrate becomes visible with melt zones as evident in Figure 5(a), (b) and (c).

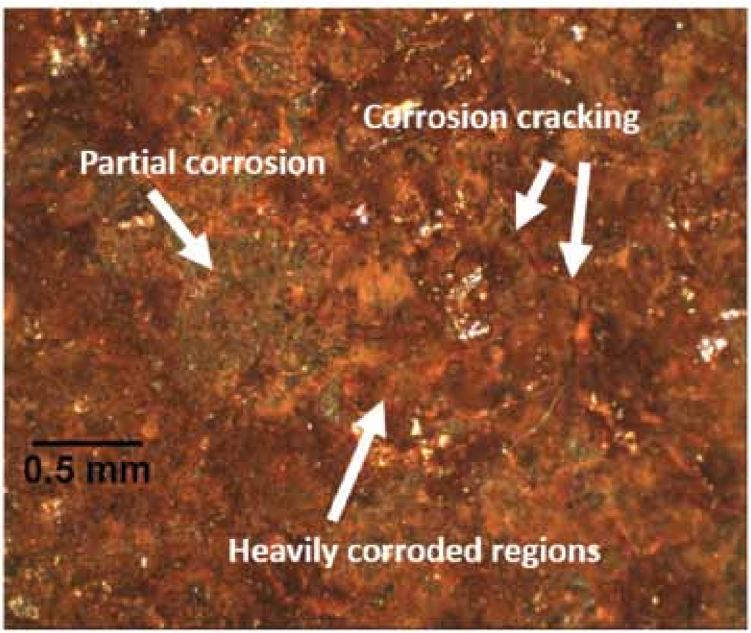

FIGURE 4
Optical image of the rusted (untreated) surface of grey cast iron brake disc.

As mentioned, increasing the laser power to 60W resulted to the best laser cleaned surface and will be further applied (Figure 5(e) and (f)) whilst varying the traverse speed. The best laser cleaned sample after varying all the parameters was 60W, 900mm/s traverse speed and 0.72mm spot size as all the rust were removed and the metal substrate was not melted (see Figure 5 (e) and (f)). Figure 4 demonstrates a direct comparison between the rusted (untreated) sample and the laser cleaned surfaces in Figure 5 (a) to (f).

Laser power (60W) and a spot size of 0.72mm was kept constant while the traverse speed was varied. Variation between 30mm/sec to 100 mm/sec produced total removal of rust, but the base metal was badly affected due to very low traverse speed which was due to the high laser power acting on the grey cast iron brake disc for a prolonged period which caused considerable melting. This would not be desirable as it is then likely that some of the surface properties would have changed. For the application of a brake disc, modification in the material's surface integrity was not an objective since it will affect the functional capabilities of the brake disc. At 200mm/sec to 300mm/sec traverse speed, there was complete rust removal while the melting of the base metal reduced. At 500mm/sec to 700mm/sec traverse speed, there was mini-

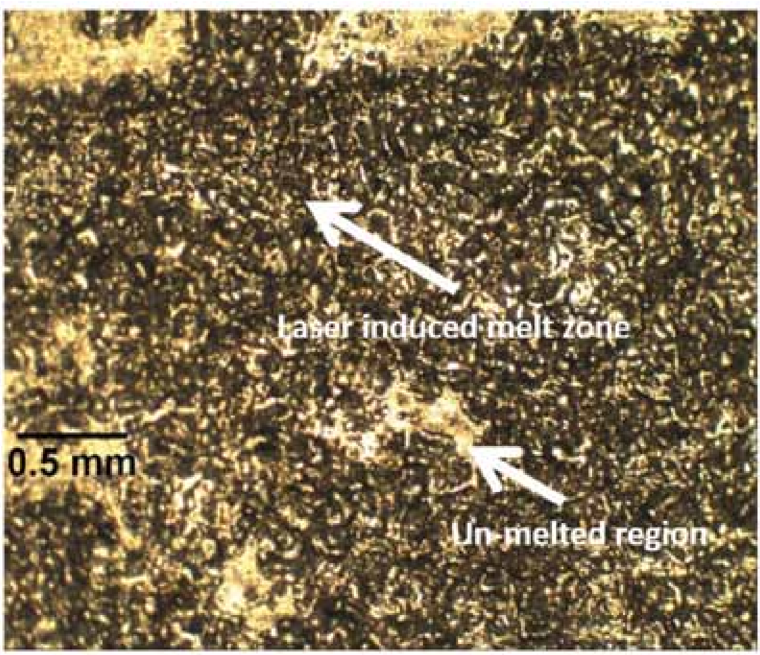

(a)

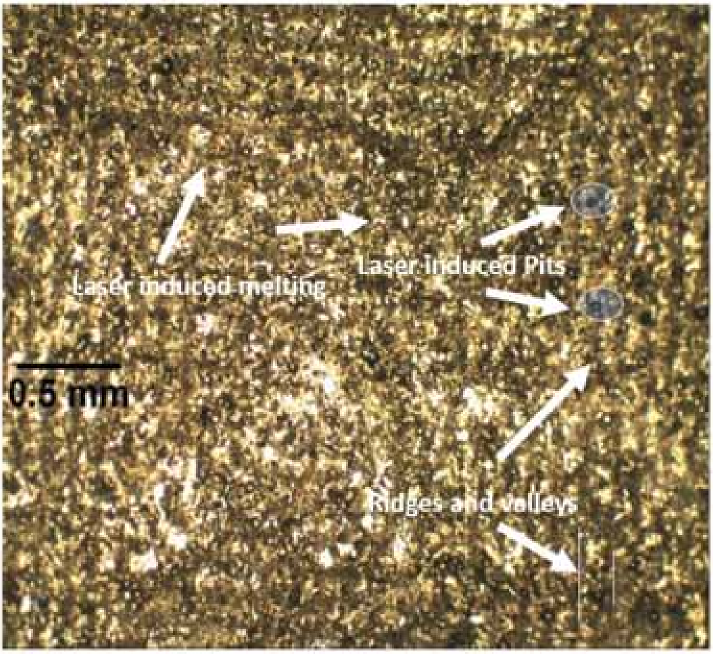
Laser induced melting
Laser induced Pits
0.5 mm
Ridges and valleys

(b)

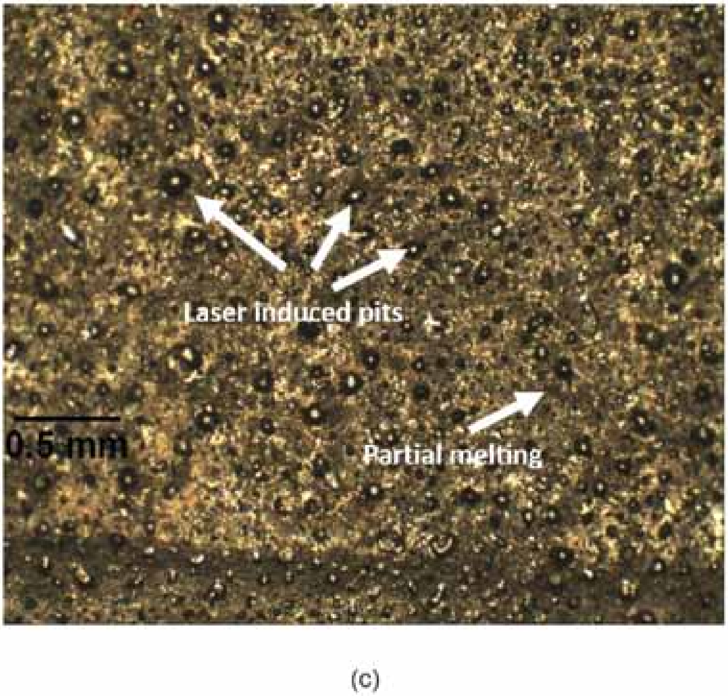
Laser Induced pits
0.5 mm
Partial melting

(c)

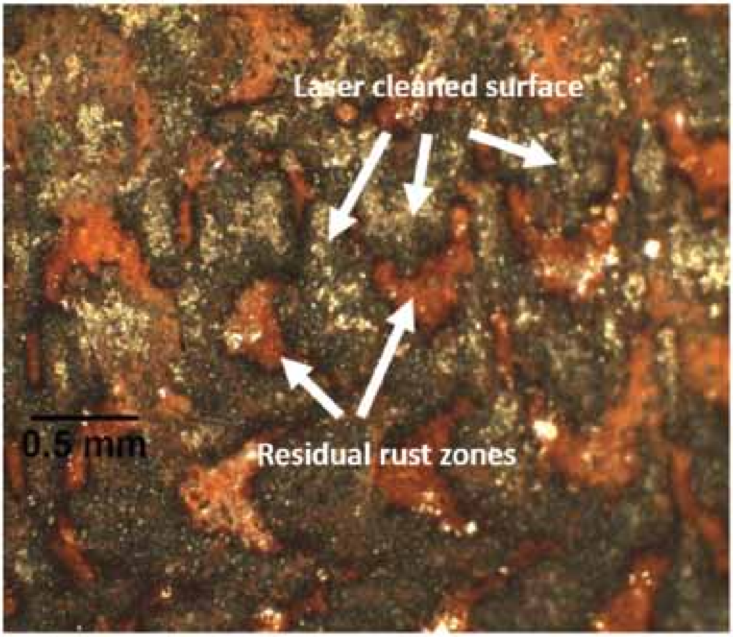
Laser cleaned surface
0.5 mm
Residual rust zones

(d)

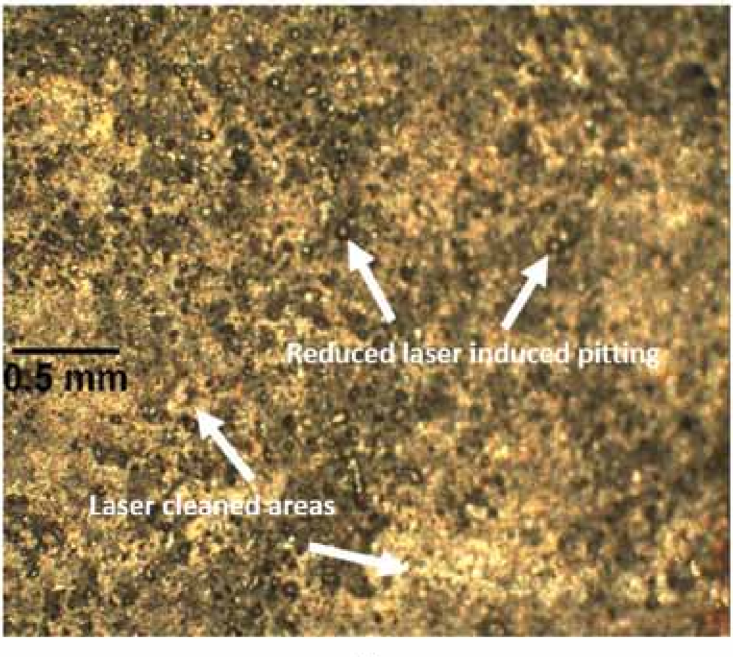
0.5 mm
Reduced laser induced pitting
Laser cleaned areas

(e)

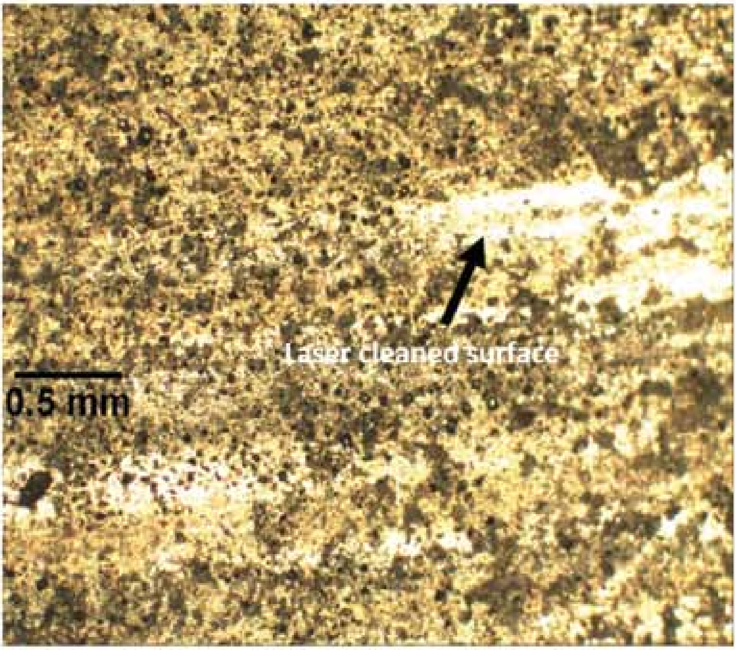

(f)

FIGURE 5
Optical images of laser cleaned surfaces in (a) at 30mm/sec; at 300mm/sec in (b); at 600mm/sec in (c); at 2000mm/sec in (d) whilst using a spot diameter of 0.72mm and laser power of 60W. (E) and (f) showing the most appropriate laser cleaned surfaces with a spot diameter of 0.72mm and laser power of 60W at 9000mm/sec.

mal melting of the base metal associated with good rust removal. As the speed increases, melting of the base metal decreases. At 900mm/sec, there was excellent removal of rust, and base metal was not affected which is rather desirable. At 1000 mm/sec, a good level of rust removal with little rust particles still seen on the surface. Beyond this speed (1500, 2000, 3000 mm/sec) rust was not removed to any considerable effect as the traverse speed was too fast to create any heating, local melting and material removal.

The spot size was varied from the largest diameter (1.69mm) obtainable based on the focal height of the laser's galvo head to the smallest diameter (0.71mm). It was concluded that to obtain the best effects and fully remove the rust layer off the grey cast iron brake disc; a minimal spot diameter was rather effective and desirable (0.71mm). Larger spot diameter at maximum laser power left many rusted regions. Thus, the best surface condition was obtained using a fairly small spot diameter focused into the material and was 0.72mm.

3.2 Measurement of rust removal

Mathematically, the depth of ablation ($Z_{ablation}$) was determined by the difference between average rusted sample thickness, and the average laser cleaned sample thickness as given by Equation (1):

$$Z_{ablation}\,(\text{mm}) = \text{average thickness of rusted sample} - \text{the average thickness of laser cleaned sample} \qquad (1)$$

Using the un-rusted surface as a reference, the deviation can serve as a characteristic to denote how much rust was removed from each sample. Deviation from the un-rusted sample can be represented as:

$$\text{Deviation (mm)} = \text{average thickness of laser cleaned surface} - \text{the average thickness of unrusted surface} \qquad 2)$$

The rusted brake disc has a slightly varying thickness of corrosion as it was exposed to the atmosphere. However, several measurements were taken at various points on each sample and the average was calculated. Hence, the mean represents the most accurate thickness value. Table 2 shows the average thickness of the surfaces with three different conditions. It was observed that the average thickness of the rusted layer was 0.33mm compared to the un-rusted surface. The thickness of the laser cleaned surfaces is shown in Table 2 as well as the depth of the rusted layer removed in Table 4. During the experiment, the cast iron brake discs were subject to high local temperatures generated from the laser beam operation at high power and or low traverse speed. Hence, it becomes unnecessary to measure the amount of rust removed after the top surface was melted and solidified, leading to the formation of melt zone, and pits, and dimples, as evident in some of the optical images in Figure 5(b) and (c).

The GPR curve determined using the experimental data (laser power *versus* Z-ablation) combined with the optimized fit is shown in Figure 6. It is clear that an increase in laser power had increased the Z-ablation which peaked at 60W with 0.30mm in thickness of rust removed. The value of Z-ablation begins to decrease beyond this point and can be postulated (from Figure 6) to saturate where the ablation depth becomes considerably constant as the laser power increases to 200W. The dip in the curve is difficult to

TABLE 2
Thickness of both the un-rusted and rusted surface of grey cart iron brake disc.

Sample Type	Reading 1 (mm)	Reading 2 (mm)	Reading 3 (mm)	Average(mm)
Un-rusted	8.18	8.22	8.20	8.20
Rusted	8.52	8.57	8.49	8.53

TABLE 3
Thickness of rust removed and ablation depth of laser cleaned grey cast iron brake disc.

Laser Cleaning Parameters (Power, Speed, Spot Size)	**Average thickness (mm)**	**$Z_{ablation}$ (mm)**	**Deviation (mm)**
10W, 1000 mm/s, 0.72 mm	8.49	0.04	0.29
20W, 1000mm/s, 0.72mm	8.46	0.07	0.26
30W, 1000mm/s, 0.72mm	8.37	0.16	0.17
40W, 1000mm/s, 0.72mm	8.31	0.22	0.11
50W, 1000mm/s, 0.72mm	8.27	0.26	0.07
60W, 1000mm/s, 0.72mm	8.23	0.30	0.03
60W, 900mm/s, 0.72mm	8.25	0.28	0.05
60W, 1000mm/s, 0.72mm	8.31	0.22	0.11
60W, 1500mm/s, 0.72mm	8.39	0.14	0.19
60W, 2000mm/s, 0.72mm	8.45	0.08	0.25
60W, 3000mm/s, 0.72mm	8.49	0.04	0.29
60W, 900mm/sec, 0.72mm	8.21	0.32	0.01
20W, 1000mm/s, 0.72mm	8.24	0.29	0.04

TABLE 4
The microhardness of various laser cleaned, rusted and un-rusted surfaces.

	Hardness (HV)					
Sample Condition	Trial 1	Trial 2	Trial 3	Trial 4	Trial 5	Average
Un-rusted	224	224	224	223	224	224
Rusted	91	94	90	97.0	95	93
Laser cleaned: 60W, 900mm/sec, 0.72mm	234	238	233	235	236	235
Laser cleaned: 60W, 1500mm/s, 0.72mm	176	175	180	175	182	178
Laser cleaned: 60W, 30mm/s, 0.72mm	307	310	302	305	305	306

explain at this stage, but it can be given to the lack of experimental data which reduces the reliability of the GPR method. Reliability would improve with further experimentation which would verify and support the predicted GPR curve.

3.3 Microhardness analysis

Table 4 presents the variation in hardness measured for the cast iron brake disc at various surface conditions applied. The average hardness of the un-rusted surface was measured to be 224 HV. This was verified by a previous work on

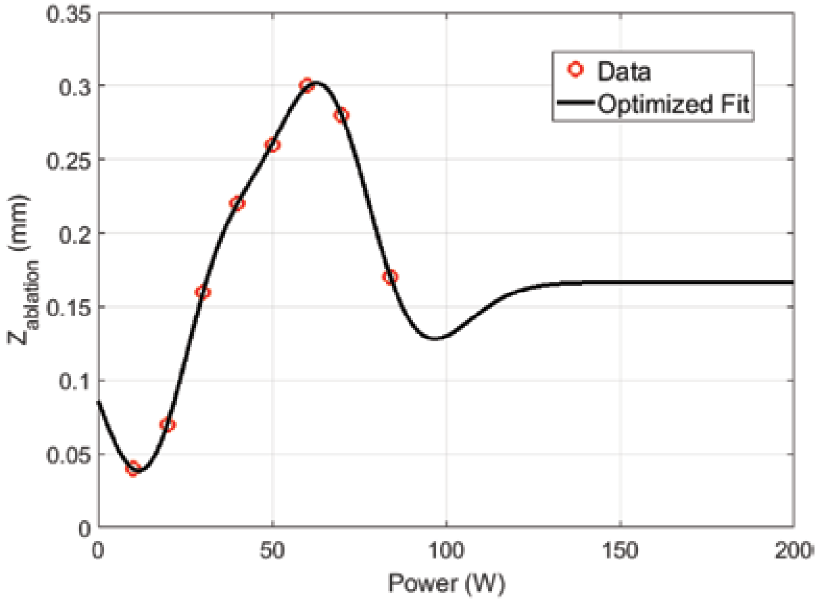

FIGURE 6
Experimental data with optimized fit for laser power *versus* Z-ablation obtained with the Gaussian process regression method.

TABLE 5
Vickers microhardness values with respect to rust thickness.

Surface Condition	Microhardness (Hv)	Rusted Layer Thickness (μm)
Rusted surface	93	330
Partially rusted surface	178	190
Un-rusted surface	224	10
Best laser cleaned surface	235	0

the manufacturing of grey cast iron automotive brake disc that reported a hardness value of 225 HV [44]. On the other hand, the hardness of the rusted surface was the lowest at an average of 93HV. This was natural since the rust particles formed on the brake disc were loosely packed and the bond strength of these particles were not as strong as that of the un-rusted surfaces to render the hardness to be high, comparatively. Table 5 presents the hardness values with respect to the rust layer thickness. It was evident that the thicker the rusted layer, the lower the hardness. This was due to the penetration depth of the laser light, which diminishes as the depth of rust increases. When these surfaces were compared to those cleaned with a laser; there was a trend of increased hardness with the lowest laser cleaning traverse speed. The lowest traverse speed comprised of the highest hardness which was an increase by 37% in comparison to the un-rusted surface and over 3 folds increase, compared to the fully rusted surface. Creek [19], suggested that rust reduces the hardness and strength of metals. That is, as the amount of rust reduces, hardness increases. Furthermore, as the traverse speed increased the hardness decreased. At 900mm/sec, the hardness was measured at an average of 235HV which was about 4.5% in comparison to the un-rusted surface. The traverse speed was increased to 1500mm/sec and the hardness was measured to be 178 HV. This was the lowest obtained from the laser cleaned surfaces. This was attributed to the fact that higher traverse speeds does not result in enough rust being removed from the respective surface. This lead to the hardness still not measuring close to the un-rusted surfaces. Tabulating these parameters into the GRP curve also yielded similar findings, whereby, the hardness reduced as the traverse speed increased (see Figure 7). As the laser beam was active for a longer period on the rusted surfaces. Particularly at low traverse speed (30mm/sec), there was significant heat being generated at the laser-material interaction. Thus, the possibility of removing the rust was not only high as evident from Figures 5, but also producing partial melt-zones which solidified at a slower rate to have generated a ductile surface. Also, the surface partial-solidification induced ductility would

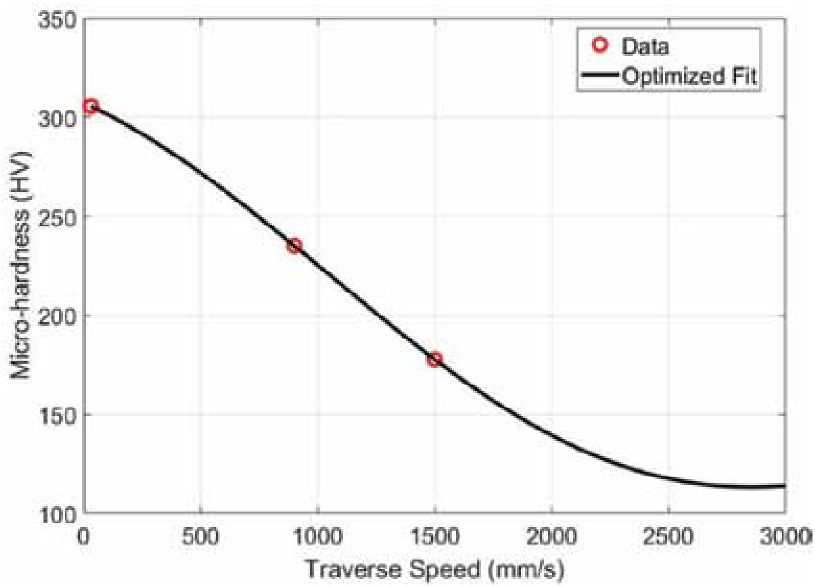

FIGURE 7
Gaussian process regression optimized curve and experimental data of microhardness *versus* traverse speed.

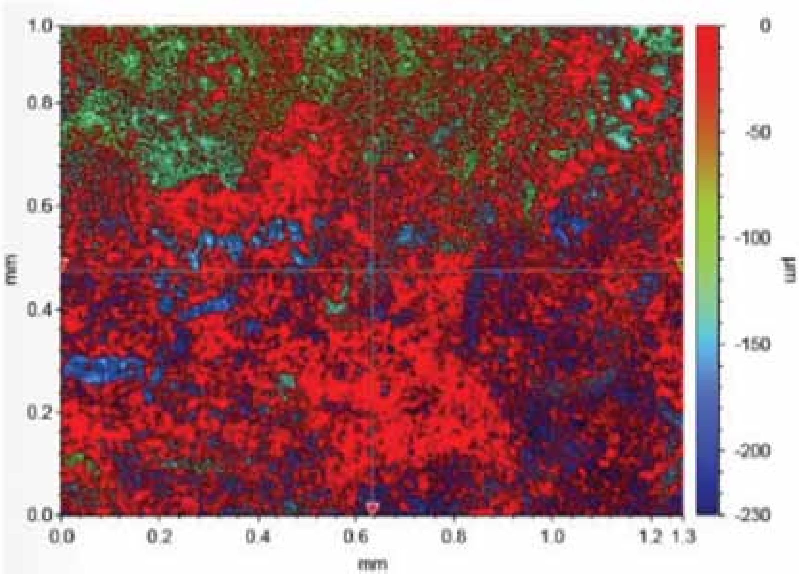

FIGURE 8
Topography of rusted grey cast iron brake disc surface.

be able to sustain for plastic deformation during cyclic fatigue failure of the specimen.

3.4 Surface roughness analysis

The average roughness (Ra) is a 2-D roughness parameter showing the arithmetic average of the absolute values of the profile heights with respect to the mean over a given length. In this case, it was significantly high for the rusted cast iron brake disc with a measured value of 55.41µm. When this was compared to the un-rusted brake disc, the measured roughness was 3.08µm and was considerably lower. This was due to the operating condition and harsh environment the brake disc operates, which lead to the formation of little rust at the onset. Further exposure lead to the formation of heavy rust at a later stage. However, after laser cleaning, the surface became much smoother. The roughness was measured to be 1.29 µm and was less than 50% compared to the un-rusted brake disc. As expected, the Rt value for the three surfaces shown in Table 6 had a similar trend with the rusted surface having a value of 230.39µm. The best laser-cleaned and un-rusted surface had an Rt value of 26.27µm and 24.89µm respectively. It was observed that the best laser-cleaned surfaces had a smaller Ra value when compared to the un-rusted sample, which however comprised of a higher Rt value. This indicates the onset of the Gaussian laser beam ablating the surface of the cast iron brake disc. This in turn, leads to an increase in the distance between the lowest and highest points over the surface area of the laser-cleaned samples than that of the un-rusted

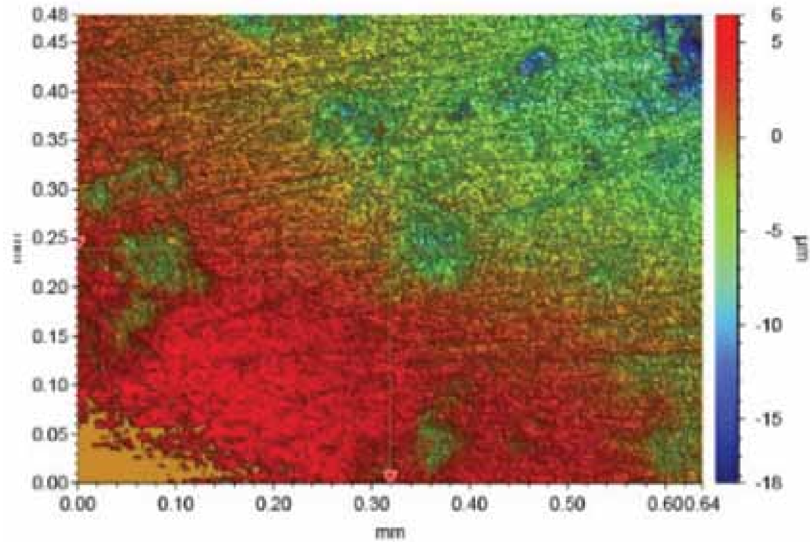

FIGURE 9
Topography of un-rusted grey cast iron brake disc surface.

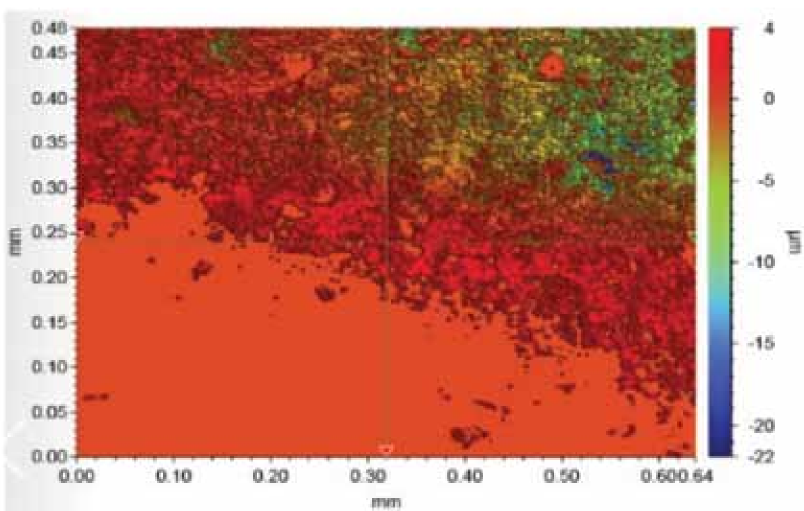

FIGURE 10
Topography of laser cleaned grey cast iron brake disc at 60W laser power, 900mm/sec and 0.72mm spot size.

surface. The 2-D topographical images of the rusted, un-rusted and totally cleaned samples are illustrated in Figure 8 to Figure 10 respectively. From Figure 8 to

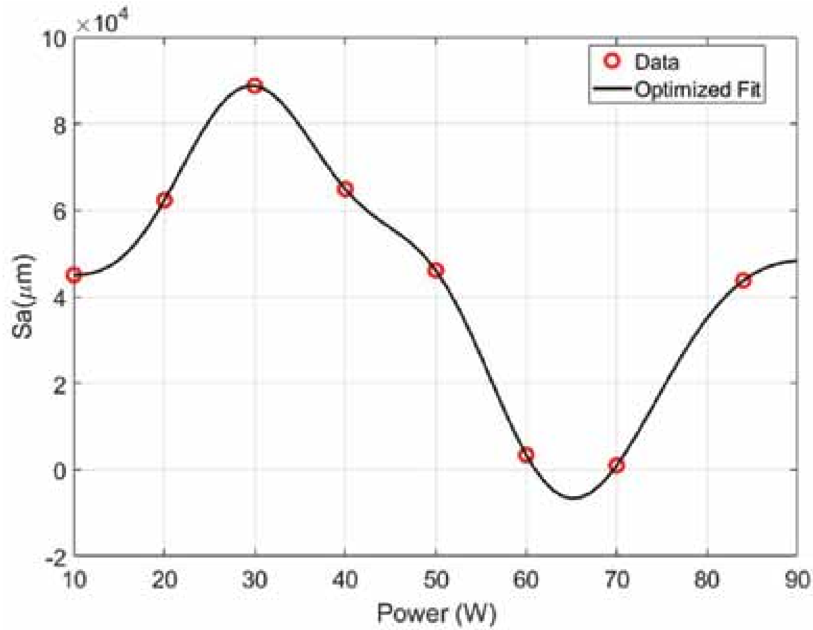

FIGURE 11
Illustrating the Sa values with respect to increase in power (60W laser power, 900mm/sec traverse speed and a spot size of 0.72 mm).

Figure 10, it is was seen that the rusted sample 2-D topography has less smooth surface when compared to the other two samples. The existence of pits, ridges and valleys might have influenced such topography.

Upon observing the Sa values, it was evident that as the laser power increased, the Sa value increased simultaneously until it peak at 30W, then subsequently decreased as the laser power further increased (see Figure 11). This indicated that the surface was smoothening as the roughness was reduced with the rusted layer being removed. At 60W the roughness was at the lowest with a possibility of complete removal of the rust. The roughness then began to increase as the laser power went up. This indicated that there was a possibility of surface melting and reforming to form a new rougher topography. This was also evident from the optical images showing melt zone beyond the laser power of 60W. As the surface considerably melted, it created dimpling and pitting effects, evident in Figure 12. This created an increase in surface roughness as evident from Figure 12 where the Sa values noticeably increased.

3.5 Microstructural analysis

The microscopic images of the un-rusted, rusted and best laser-cleaned surfaces are shown in Figure 14 to Figure 16. The microstructural images of the

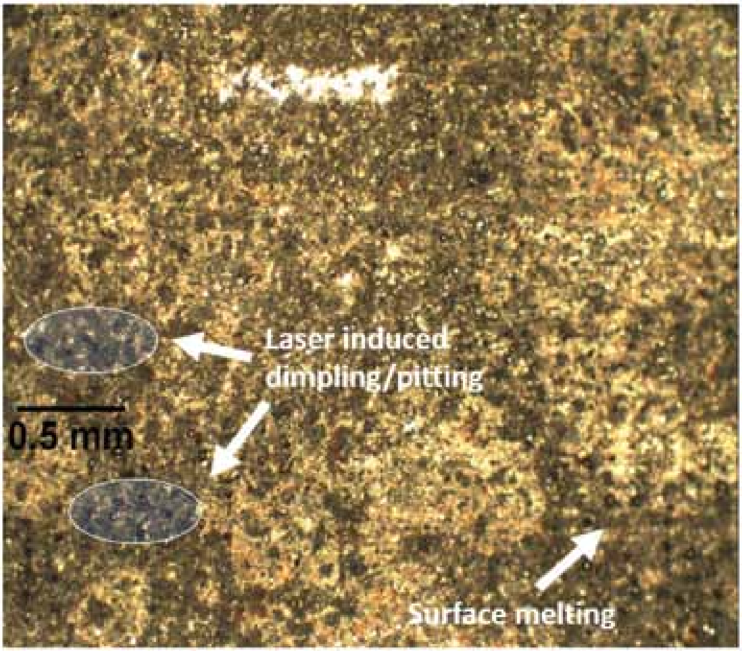

FIGURE 12
Showing the roughening of the surface at 70W laser power, 900mm/sec and 0.72 mm spot size as melt zones take place in various area.

three surfaces all show the presence of a black flake-like structure (graphite flakes). Grey cast iron is characterised for having a large portion of its carbon in the form of graphite flakes. The fast interstitial diffusion of small carbon atoms makes the formation of graphite flakes possible. As diffusion progresses, more graphite is formed. The plane of such graphite is held by a covalent bond and has a hexagonal structure. The presence of silicon as one of the alloying elements of grey cast iron promotes the formation of ferrite and graphite. It acts as a strong graphitizer during eutectic solidification of grey cast iron. Eutectic cells are formed by the nucleation of graphite. The mixture of graphite and austenite makes up the eutectic cells. The eutectic cells can be viewed on the micrograph chemical etching. During the eutectoid transformation, the austenite transforms into ferrite and cementite or graphite. The system stability is dependent on the transformation that occurs. Graphite or cementite either occupies the carbon-rich zone based on the system stability, that is, if the system is metastable, it prefers cementite. If the system is stable, it prefers graphite. The graphite flake is seen to be much softer than the surrounding matrix which is viewed as a void. The formation of the pearlitic matrix with graphite particles occurs in the surrounding matrix of the flake to prevent the structure from being too weak. This formation

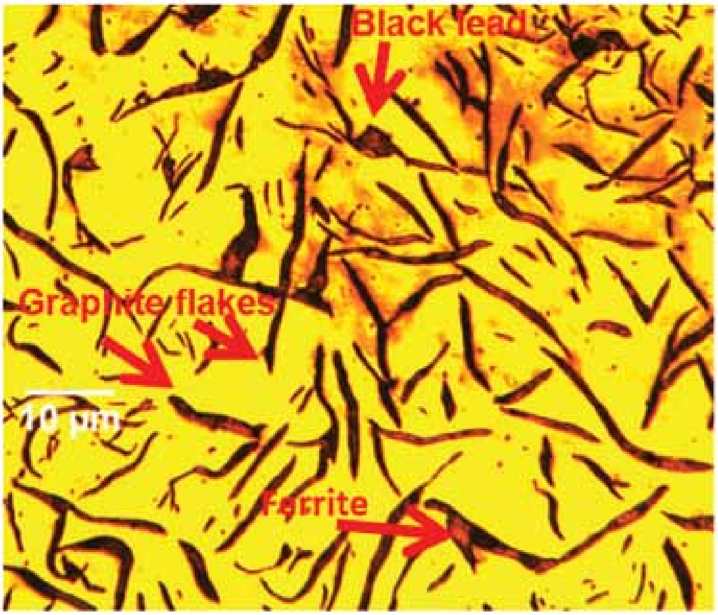

FIGURE 13
Microstructure of the un-rusted surface of the grey cast iron.

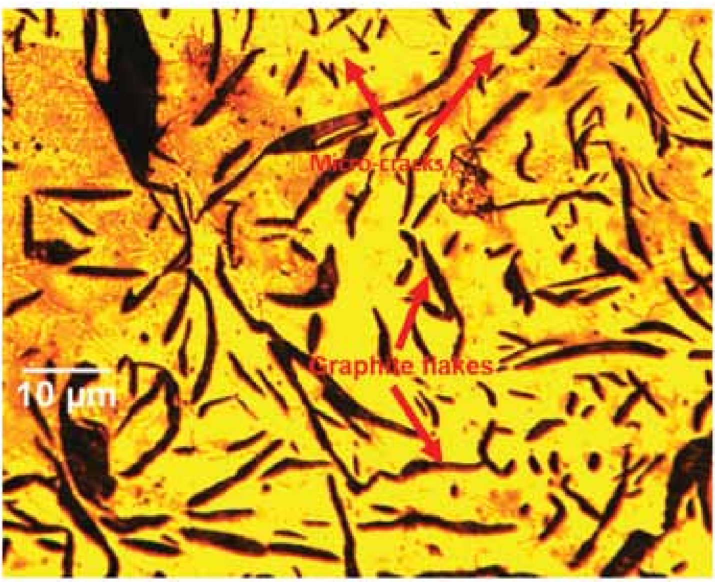

FIGURE 14
Microstructure of rusted surface.

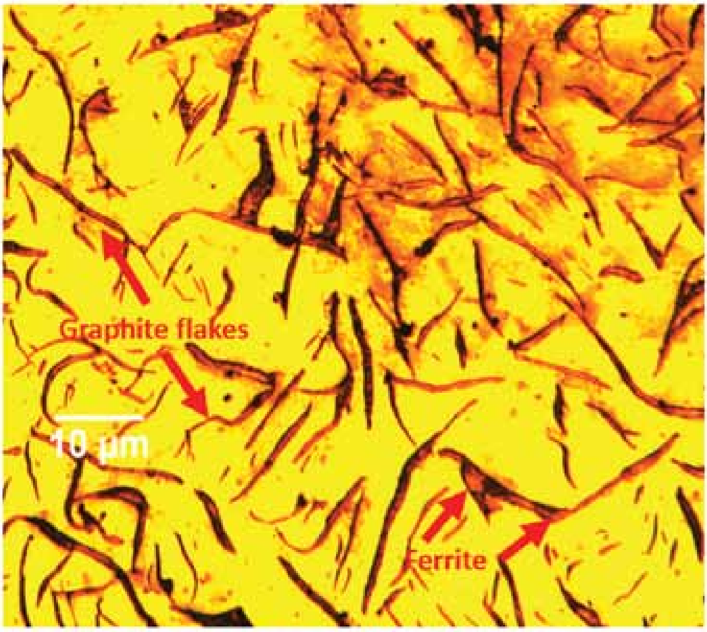

FIGURE 15
Microstructure of a laser-cleaned surface (60W of laser power, 900mm/s traverse speed, spot size of 0.72mm).

gives it good compressive strength, good thermal conductivity and vibration damping. It was observed from the microstructure that the graphite flakes vary in shape and size. The rusted sample shows larger flakes when compared to the un-rusted and laser-cleaned surfaces. It also exhibits relatively longer graphite flakes on the average. Deep black pits are also seen on the microstructure of the rusted sample which signifies the presence of impurities and non-metallic inclusions. The presence of inclusions and impurities along with the slightly longer and larger graphite flake is responsible for the low hardness value and high Ra value of the rusted sample.

The laser-cleaned sample has a relatively larger spacing between the flakes when compared to the un-rusted and rusted surfaces. An increase in space between flakes results in an increase in the strength and a corresponding increase in hardness. A relatively shorter flake length and smaller flake size yields a higher hardness value when compared to the un-rusted and the rusted surfaces. This is because graphite particles are generally softer. The hardness is evident as seen on the microstructure of the laser cleaned surface in Figure 15. There is a relative decrease in the number of graphite flakes when compared to the microstructure of the rusted grey cast iron sample. Furthermore, a denser cluster of graphite flakes with relatively bigger flake size and longer flake length created lesser space for a hard pearlitic matrix. The grey region in Figure 13 to Figure 15 represents a pearlitic matrix. The pearlitic matrix contained two phases which are ferrite and cementite. While cementite is a hard and brittle intermetallic compound, ferrite has low strength and high ductility. Besides the cementite found in the pearlite matrix, the micrograph also showed no evidence of cementite. The dual phase involving ferrite and cementite which creates the pearlitic matrix originates from the austenite phase. At higher temperature, only austenite is present with 0.76%C been dissolved in the face-centered cubic (FCC) crystal's solid solution. The cooling down of iron to 727°C results in several simultaneous changes. It is highly likely that the laser cleaning process induced temperatures above that level. First, the iron changes from FCC austenite to body-centred cubic ferrite, but the ferrite can only accommodate 0.022% carbon in solid solution. The excess carbon left was then rejected forming the carbon-rich intermetallic phase which is cementite.

4 CONCLUSIONS

The enhancement of the surface integrity of a rusted, grey cast iron automotive brake disc was achieved *via* a laser cleaning process. Laser cleaning and rust removal are fast and effective in enhancing the surface integrity of such materials. The results showed that the presence of rust on cast iron reduces its mechanical and physical properties. The ripple effect of such reduction leads to failure of the brake disc when fused into the braking system of an automotive vehicle. The best set of laser parameter for removing rust from the grey cast iron brake disc using a CO_2 laser system was 60W of laser power, 900mm/s traverse speed and a spot size of 0.72mm. The presence of rust on the surface of the brake disc greatly reduces its microhardness. The laser cleaning process positively altered the microhardness value, verified by an increase of 5.04% when comparing the un-rusted sample (223 HV) to the best-cleaned sample (235 HV). The best-cleaned sample has an Ra value of 1.29μm which is relatively good when compared to that of the un-rusted samples. The microstructure of the samples showed that the presence of randomly distributed graphite flakes surrounded by a pearlitic matrix contained ferrite and cementite. The GPR technique can demonstrate an in-depth prediction of parameters beyond the experimental data. However, further experimental work verifying the prediction will improve its reliability for laser processing problems such as the one herein. The applied parameters showed that laser cleaning could be successfully applied to not only clean rusted surfaces of metallic materials such as the one herein, but could also have a positive effect on some of the material properties, thus, increasing the life span of the brake disc. Laser cleaning of the brake disc will drastically reduce cost (maintenance and replacement cost). It also prevents sudden failure since the parts have been enhanced to become more durable and reliable, even when operating under harsh conditions. It is also much greener and has the potential to replace chemicals, abrasive materials or shot blasting and harmful cleaning solvent that poses hazards to the end-user.

REFERENCES

[1] Al-Numan, B. and Cicek V. *Corrosion Chemistry*. Salem, MA, USA: Scrivenger publisher LLC. 2011.

[2] Adebayo, A. V . Relationship between Graphite Flake Sizes and the Mechanical Properties of Grey Iron. *International Journal of Materials Science and Application.* **2** (2013), 94-98.

[3] ASTM (2017). *ASTM Class 35 Standard Gray Iron Test Bars, as Cast*. Retrieved 30th November 2017 from http://www.matweb.com/search/datasheet_print.aspx?matguid=fcc3101c8cda4cf1b2ce0b1dcde93dd4.

[4] Bélisle E., Huang Z., Gheribi A. Scalable Gaussian Process Regression for Prediction of Material Properties. In: Wang H., Sharaf M.A. (eds) Databases Theory and Applications. ADC 2014. Lecture Notes in Computer Science **8506**. (2014) Springer, Cham, https://doi.org/10.1007/978-3-319-08608-8_4.

[5] Butcher, E. A green way to clean – Laser cleaning. *Laser Technik Journal*. Surface Processing, 9 (2012). 36 - 38.

[6] Byskov-Nielsen, J., Savolainen, J-M. S., Christensen, M., and Balling, P. Ultra-short pulse laser ablation of metals: threshold fluence, incubation coefficient and ablation rates. *Applied physics A: Materials Science and Processing* **101** (2010), 97-101.

[7] Chare I.A., Jeffery R. and Melchers R.E. Rust removal from steel coupons after short-term marine immersion. *Corrosion: the journal of science and engineering* **71** (2015), 811-818.

[8] Ch D., Kiran U.C., and Kumar, V.Y. Design, Analysiss and Manufacturing of Disc Brake Rotor. *International Journal of Engineering Research and Development* **13** (2017), 15-23.

[9] Creek, V. *Corrosion Engineering*. Cambridge: Woodhead Publishing. 2014.

[10] Dhiyaneswaran, S., and Amirthagadeswaran, K.S. Comparative study of Disc Brake materials through Computer Aided Engineering. *International Journal of Modern Engineering Research.* (2015) 173-179.

[11] Fogarassy E. Geohegen D. and Stuke M. *Laser Ablation*. Newnes Australia: Elsevier Science. 2012.

[12] Granta Design Ltd. CES 2017 Selector, EduPack. Cambridge, UK. www.granta.co.uk.

[13] Hays G.F. (2012). *Now Is the Time*. World Corrosion Organisation. 1-2, Retrieved on 25th December 2015, from http://events.nace.org/euro/corrodia/Fall_2010/wco.asp

[14] Holtzer M., Gorny M. and Danta R. *Microstructure and Properties of Ductile Iron and Compacted Graphite Iron Casting - The Effects of Mold Sand/ Metal Interface Phenomena*. Poland: Springer International Publishing. 2015.

[15] Kannatey-Asibu E. *Principles of Laser Material Processing,* 1 edition. New Jersey, USA: Wiley. 2009.

[16] Kane, D.M. *Laser Cleaning*. ed. by Kane, D.M. World Scientific publishing company. 2007.

[17] Koh, Y.S. *Laser Cleaning as a Conservation Technique for Corroded Metal Artifacts*. 2006.

[18] Koch H.G., Brongers, M.P.H., Thompson, N.G., Virmani, Y.P., and Payer, J.H. *Corrosion Cost and Preventive Strategies in the United States*. Federal Highway Administration, USA. 2002.

[19] Lawrence, J. *Advances in Laser Material Processing: Technology, Research and Application.* Cambridge: Woodhead Publishing. 2017.

[20] Maleque, M.A., Dyuti, S., and Rahman, M.M. *Material Selection Method in Design of the Automotive Brake Disc.* 2010.

[21] Maluf, O., Angeloni, M., Milan, M.T., and Filho, B. *Development of materials for automotive disc brakes.* 2004.

[22] Masoud I.M., Al-Jarrah J.A., and Abu M.T. Manufacturing of Grey Cast Iron Automotive Disc Brake. *Indian Journal of Applied Research* **4** (2014), 131.

[23] Pierre R. and Roberge R. *Corrosion Inspection and Monitoring*. London: Wiley. 2007.

[24] Przestacki D., Wietze Otter, H., and Depre, P. *The Cleaning of Superficially Corrosion Metals by CO^2 Laser*. 2006.

[25] Ren Z., Wu C., Chen H., Lu Y., Qiao H., and Hu, T. Mechanism of Laser Derusting and Surface Properties of Low Carbon Steel. *Opto-Electronic Engineering* **44** (2017), 1210-1216.

[26] Renner F.U., Stierle, A., Dosch, H., Kolb, D.M., Lee T-L. and Zegenhagen, J. *Initial corrosion observed on the atomic scale* **439** (2006), 707-710.

[27] Sanjeevan P. and Klemm A.J. (2004) *A Review of Laser Technique Application in Cleaning Process of Porous Construction Materials*. Laser technique in the cleaning of porous construction materials Retrieved 3rd January 2017 from https://www.irbnet.de/daten/iconda/CIB10654.pdf

[28] Shukla P.P., and Lawrence J. Role of laser beam radiance in different ceramic processing: A two wavelength comparison. *Optics and Laser Technology* **54** (2013), 380-388.

[29] Shukla P., Lawrence J., and Zhang Yu. Understanding Laser-beam brightness: A Review on a New Prospective in Materials Processing, *Optics and Lasers in Engineering*, **75,** (2015) 40-51.

[30] Shukla P.P., and Lawrence J., Identification of Optical Parameters for Determination of Radiance, Journal of Optics, Optical Society of India, **44** (2015) 12-19.

[31] Siatou, A., Charalambous, D., Argyropoulos, V., and Pouli, P. *A Comprehensive Study for the Laser Cleaning of Corrosion Layers due to Environmental Pollution for Metal Objects of Cultural Value : Preliminary Studies on Artificial Corroded Coupons.* Hindawi Publishing corporation. 2006.

[32] Steen W.M. and Mazumder J. *Laser Material Processing*. 4th edition London: Springer London. 2010.

[33] Siano S. *Principles of Laser Cleaning in Conservation*. in Schreiner, M. Strlic M. and, Salimbeni, R. (eds.): Handbook on the Use of Lasers in Conservation and Conservation Science. 2008.

[34] SPI Lasers. (2015). *Laser Cleaning*. Retrieved 25th December 2017, from http://www.spilasers.com/laser-processing-applications/laser-cleaning/.

[35] Tong, Y., Li, F., Huang, J., Wu, X., and Ren, X. Simulation and Research on the Laser Removal Mechanism. *International Journal of Non-Linear Science* **23** (2017), 137-141.

[36] Varney J., Koch, G., Thompson, N., Moghissi, O., Gould, M., and Payer, J. *International Measures of Prevention, Application, and Economics of Corrosion Technologies Study*. NACE International- (IMPACT). 2016.

[37] Wang, Z., Huang, W., and Zeng, X. Parameters and Surface Performance of Laser Removal of Rust Layer on A3 Steel. *Surface and Coatings Technology* **166** (2003), 10-16.

[38] Waldman J. *Rust: The Longest War*. New York, USA: Simon & Schuster; Reprint edition. 2015.

[39] Wang F.F.Y. *Laser Material Processing: Material Processing Theory and Practices*. ed. by Boss, M. North-Holland Publishing Company. 2012.

[40] Watkins, K.G., Curran, C., and Lee, J.-M. Two New Mechanisms for Laser Cleaning Using Nd:YAG Sources. *Journal of Cultural Heritage*. (2003), 56s - 64s.

[41] Yathish, K.O., Arun, L.R., Kuldeep, B., and Muthanna, K.P. analysis and material optimization of Disc Brake Using MMC. *International Journal of Innovative Research in Science, Engineering and Technology* **2** (2013), 4101-4108.

[42] Yilbas B.S. and Shuja Shahzada Z. *Laser Surface Processing and Model Studies.* Germany: Springer-Verlag Berlin Heidelberg. 2013.

[43] Young D. *High Temperature Oxidation and Corrosion of Metals*. 2nd edition: Amsterdam, Netherlands: Elsevier Science. 2016.

[44] Sun Z., Sun Z., Xu J., Zhou, W., and Zhou, W., Parameters and mechanism of laser cleaning rust deposit on the steel surface. *Proc. SPIE 4915, Lasers in Material Processing and Manufacturing*. 12 September 2002, Shanghai, China, doi: 10.1117/12.482918; https://doi.org/10.1117/12.482918.